Université catholique de Louvain
Faculté des Sciences
Département de Physique

Charm studies in emulsion

Sergey Kalinin
Promoteur: Professeur T. Delbar

Dissertation présentée en vue de l'obtention
du grade de Docteur en Sciences

March 2006

Contents

List of Figures

List of Tables

Introduction

> There are just three possibilities:
> 1. Charm is not found, and I eat my hat.
> 2. Charm is found by hadron spectroscopy, and we celebrate.
> 3. Charm is found by outlanders, and you eat your hats.
>
> Shelly Glashow

For thousands of years human beings were observing different phenomena and then they were trying to find explanations to the observations. However, the c-quark has been discovered in the opposite way. First, it has been predicted by the theory, and second, its existence has been demonstrated by the experiment. This is exactly the reason why c-quark is called *charm*. The quark has been discovered in 1974 [1, 2]. Since then, a lot of experiments have been performed to study its properties but even today there are dark areas in the knowledge about this particle.

The analysis presented in this thesis concerns the production mechanism and the decay properties of charmed hadrons. The analysis is based on the events observed in neutrino and anti-neutrino deep inelastic scattering on emulsion target. The events originate primarily from charged current production of charm quarks,

$$\nu + \mathrm{N} \rightarrow \mu^- + c + X \tag{1}$$

$$\overline{\nu} + \mathrm{N} \rightarrow \mu^+ + \overline{c} + X \tag{2}$$

and were collected by the CHORUS collaboration during the years 1995-1998 at CERN.

In the last decade of XXth century several observations pointed to the possibility that neutrinos may have masses. The difference between their masses and non-zero mixing angles lead to so-called neutrino oscillations

when a particle of one type transfroms into another type of particle without external interactions. Originally, the CHORUS experiment was designed to discover $\nu_\mu \rightarrow \nu_\tau$ oscillations by the appearance of ν_τ in a ν_μ beam. The selection of events with τ produced in neutrino interactions is based on flightpath. Since charmed hadrons have similar flightpaths as τ, they are background events for the oscillations. The data sample collected for the discovery of oscillations would contain a lot of charmed hadrons which gives a unique opportunity to explore heavy quark production mechanisms. The subject of this thesis is limited to charm production in neutrino-induced charged-current interactions.

Neutrino-nucleon deep-inelastic scattering is a very effective way to study the dynamics of c-quark production, to explore the inner structure of the nucleon and to measure several parameters in the Standard Model of elementary particles interactions. For example, the charm production in neutrino interactions allows to measure the difference between nucleon strange sea content, $|V_{\mathrm{cd}}|$ and $|V_{\mathrm{cs}}|$, the Cabibbo-Kobayashi-Maskawa (CKM) matrix elements. Looking at the decay products of charmed hadrons permits to directly measure the average muonic branching ratio.

The Standard Model

The Standard Model of particle physics is a model which describes the strong, weak, and electromagnetic fundamental forces, as well as the fundamental particles that make up all matter. Developed in sixties and early seventies, it is a quantum field theory, and consistent with both quantum mechanics and special relativity. To date, almost all experimental tests of the three forces described by the Standard Model have agreed with its predictions. However, the Standard Model is not a complete theory of fundamental interactions, primarily because it does not describe gravity and masses. The model has been proposed by S. L. Glashow, S. Weinberg and A. Salam [3, 4, 5] and is being extended since then.

The Standard Model contains both fermionic and bosonic fundamental particles. Fermions are particles which possess half-integer spin and obey the Pauli exclusion principle, which states that no fermions of the same type (electrons, quarks, etc) can share the same quantum state. Bosons possess integer spin and do not obey the Pauli exclusion principle. The two sorts of particles play different role in nature: fermions are particles of matter and bosons are particles that transmit forces.

In the Standard Model, the theory of the electroweak interaction (which

describes the weak and electromagnetic interactions) is combined with the theory of quantum chromodynamics. All these theories are gauge theories, meaning that they model the forces between fermions by coupling them to bosons which mediate (or "carry") the forces. The Lagrangian of each set of mediating bosons is invariant under a transformation called a gauge transformation, so these mediating bosons are referred to as gauge bosons. The bosons in the Standard Model are:

- Photons, which mediate the electromagnetic interaction.
- $W^{\pm}$ and Z bosons, which mediate the weak force.
- Eight species of gluons, which mediate the strong nuclear force. Six of these gluons are labeled as pairs of "colors"(charges) and "anti-colors" (for example, a gluon can carry "red" and "anti-green".) The other two species are a more complex mix of colors and anti-colors.
- The Higgs boson, which induce spontaneous symmetry breaking of the gauge groups and give a mass to the particles.

The gauge transformations of the gauge bosons can be exactly described using a unitary group called a "gauge group". The gauge group of the strong interaction is SU(3), and the gauge group of the electroweak interaction is SU(2)×U(1). Therefore, the Standard Model is often referred to as SU(3)×SU(2)×U(1). The Higgs boson is the only boson in the theory which is not a gauge boson; it has a special status in the theory. Gravitons, the bosons believed to mediate the gravitational interaction, are not accounted for in the Standard Model.

There are twelve different types, or "flavors", of fermions in the Standard Model. Among the proton, neutron, and electron, those fermions which constitute the matter, the Standard Model considers only the electron as a fundamental particle. The proton and neutron are aggregates of smaller particles known as quarks, which are held together by the strong interaction. The fundamental fermions in the Standard Model are given in Table 1.

Table 1: Fermions of the Standard Model

Fermion	Symbol	Electric charge	Color multiplet	Mass
Generation 1				
Electron	e^-	-1	1	0.511 MeV
Electron neutrino	ν_e	0	1	<460 eV (68% C.L.)
Positron	e^+	+1	1	0.511 MeV
Electron anti-neutrino	$\overline{\nu}_e$	0	1	<3 eV
Up quark	u	+2/3	3	∼5 MeV
Down quark	d	-1/3	3	∼10 MeV
Anti-up anti-quark	$\overline{u}$	-2/3	$\overline{3}$	∼5 MeV
Anti-down anti-quark	$\overline{d}$	+1/3	$\overline{3}$	∼10 MeV
Generation 2				
Muon	μ^-	-1	1	105.6 MeV
Muon neutrino	ν_μ	0	1	<0.19 MeV (90% C.L.)
Anti-Muon	μ^+	+1	1	105.6 MeV
Muon anti-neutrino	$\overline{\nu}_\mu$	0	1	-
Charm quark	c	+2/3	3	1.25±0.1 GeV
Strange quark	s	-1/3	3	∼ 100 MeV
Anti-charm anti-quark	$\overline{c}$	-2/3	$\overline{3}$	∼1.5 GeV
Anti-strange anti-quark	$\overline{s}$	+1/3	$\overline{3}$	∼100 MeV
Generation 3				
Tau	τ	-1	1	1.78 GeV
Tau neutrino	ν_τ	0	1	<18.2 MeV (95% C.L.)
Anti-Tau	$\overline{\tau}$	+1	1	1.78 GeV
Tau anti-neutrino	$\overline{\nu}_\tau$	0	1	-
Top quark	t	+2/3	3	178 GeV
Bottom quark	b	-1/3	3	∼4.7 GeV
Anti-top anti-quark	$\overline{t}$	-2/3	$\overline{3}$	178 GeV
Anti-bottom anti-quark	$\overline{b}$	+1/3	$\overline{3}$	∼4.7 GeV

The fermions can be arranged in three "generations", the first one consisting of the electron, the electron neutrino, the up and down quarks. All ordinary matter is made from these first generation particles; the higher generation particles decay quickly into the first generation ones (except for the neutrinos that are thought to be stable) and can only be generated for a short time in high-energy experiments. The reason for arranging them in generations is that the four fermions in each generation behave almost exactly like their counterparts in the other generations; the only difference is their masses. For example, the electron and the muon both have half-integer spin and unit electric charge, but the muon is about 200 times more massive.

The electron and the electron-neutrino, and their counterparts in the other generations, are called "leptons". Unlike the other fermions, they do not possess a quality called "color", and therefore their interactions (weak and electromagnetic) fall off with distance. On the other hand, the strong force between quarks gets stronger with distance, so that quarks are always found in colorless combinations called hadrons. These are either fermionic baryons composed of three quarks (the proton and neutron being the most familiar example) or bosonic mesons composed of a quark-anti-quark pair (such as pions). The energy of such aggregates exceeds that of the quark components due to the presence of a gluon field. This field plays an extremely important role in the hadrons production and is associated with the mass threshold effects when a heavy quark is produced at the energies close to the bare quark mass. And, in general, the gluon field describes the transition between quarks as free particles into bound hadrons.

There is yet another distinctive particularity related to the quarks*. The quark mass eigenstates are not the same as the weak eigenstates. Phrased differently, the quarks participating in strong and weak interactions are not the same. This difference is accounted by introducing a mixing. By convention, the mixing is expressed in terms of a 3×3 unitary matrix V operating on the charge $-e/3$ quark masses eigenstates

$$\begin{pmatrix} d' \\ s' \\ b' \end{pmatrix} = \begin{pmatrix} V_{\rm ud} & V_{\rm us} & V_{\rm ub} \\ V_{\rm cd} & V_{\rm cs} & V_{\rm cb} \\ V_{\rm td} & V_{\rm ts} & V_{\rm tb} \end{pmatrix} \begin{pmatrix} d \\ s \\ b \end{pmatrix} , \tag{3}$$

where d', s' and b' are the weak interaction eigenstates. The first explicit parametrization of the matrix has been made by Kobayashi and Maskawa [6] in 1973. It is actually a generalization of the four-quark case, where

*And to the neutrinos in the case of mixings between neutrinos of different sorts.

the matrix is described by a single parameter, the Cabibbo angle [7]. Their parametrization involves four parameters, three angles θ_1, θ_2, θ_3 and a phase δ. The phase is needed to describe the breaking of the CP invariance in the weak interactions.

A frequently used approximation was proposed by Wolfenstein [8] which qualitatively shows the relations between the matrix elements

$$V = \begin{pmatrix} 1-\lambda^2/2 & \lambda & A\lambda^3(\rho - i\eta) \\ -\lambda & 1-\lambda^2/2 & A\lambda^2 \\ A\lambda^3(1-\rho-i\eta) & -A\lambda^2 & 1 \end{pmatrix} + \mathcal{O}(\lambda^4) \ , \qquad (4)$$

with A, ρ and η real numbers that were intended to be of order unity and $0 < \lambda < 1$. This approximate form is widely used, but care must be taken, since the CP-violating phase enters V_{cd} and V_{cs} through terms that are of higher order in λ.

The precise measurements of the CKM matrix elements are extremely important tasks because they are parameters of the Standard Model and they enter into the Lagrangian. Also, a deviation from the unitarity would indicate the existence of a fourth generation of the fermions. The unitarity constrain is usually presented as a triangle on a plane which combines different measurements. It is shown in Fig. 1.

Tests and predictions

The so-called GIM mechanism [10] predicted the charm quark before it was observed experimentally. Later when a bottom quark has been discovered, most physicists were sure of the existence of the top quark. The only question was its mass. The top quark has been observed in the 90s.

On top of that, the Standard Model predicted the existence of $W^{\pm}$ and Z bosons and the gluon before these particles had been observed. Their predicted properties were experimentally confirmed with good precision.

The Large Electron-Positron collider at CERN tested various predictions about the decay of Z bosons, and found them confirmed. To get an idea of the success of the Standard Model let compare measurements of several quatities that are dependent in the model. As it follows from the mass terms of electroweak Lagrangian, $\cos\theta_{\mathrm{W}} = \frac{m_{\mathrm{W}}}{m_{\mathrm{Z}}}$, where θ_{W} is so-called Weinberg angle. However, it is possible to measure some of these quatities separetely [11, 12]. The comparison is summarized in Table 2.

Figure 1: Representation in the complex plane of the triangle formed by the CKM matrix elements. The plot was made by combining different measurements [9]. The three angles are defined by $\alpha = \arg\left[-\frac{V_{\rm td}V_{\rm tb}^*}{V_{\rm ud}V_{\rm ub}^*}\right]$, $\beta = \arg\left[-\frac{V_{\rm cd}V_{\rm cb}^*}{V_{\rm td}V_{\rm tb}^*}\right]$, $\gamma = \arg\left[-\frac{V_{\rm ud}V_{\rm ub}^*}{V_{\rm cd}V_{\rm cb}^*}\right]$. The constants $\Delta m_{\rm d}$ and $\Delta m_{\rm s}$ are oscillation frequencies. They are defined as mass difference between the two mass eighenstates $B_{\rm H}$ and $B_{\rm L}$ for $B_{\rm d}$ and $B_{\rm s}$ respectively. $\overline{\eta} = \eta(1-\lambda^2/2)$ and $\overline{\rho} = \rho(1-\lambda^2/2)$. The area around the vertex of the angle α correspond to the unitarity of the triangle.

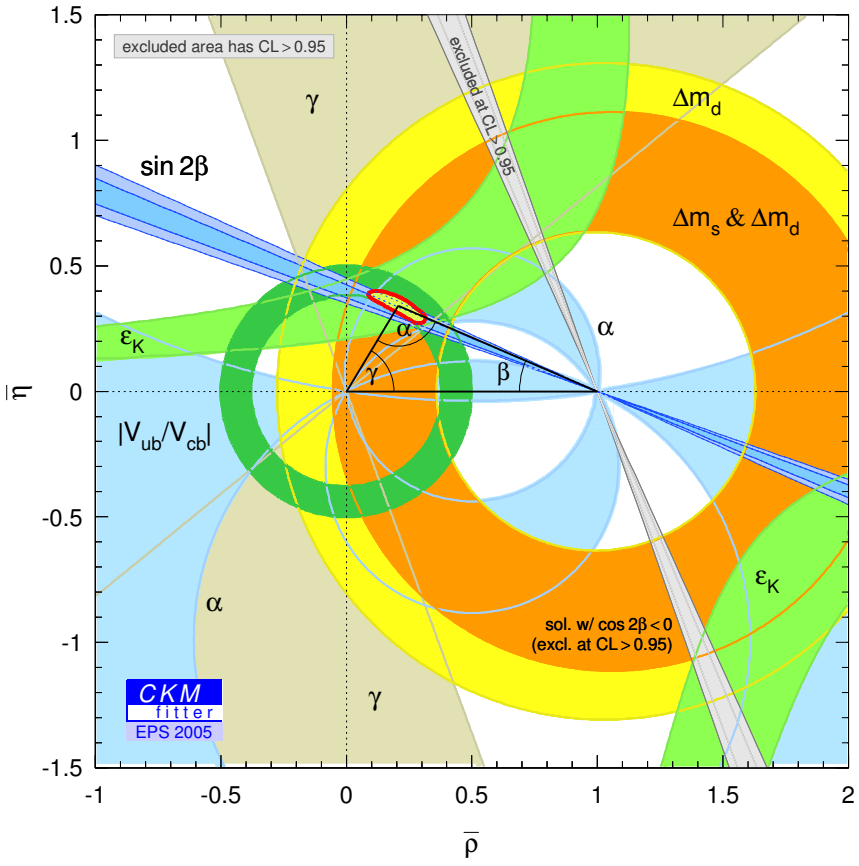

Challenges to the Standard Model

Although the Standard Model has had great success in explaining experimental results, it has never been accepted as a complete theory of funda-

Table 2: Experimental results on the masses of W and Z bosons and $\sin^2\theta_{\rm W}$. The ratio of $m_{\rm W}$ and $m_{\rm Z}$ gives $\sin^2\theta_{\rm W} = 0.222\pm0.001$ which should be compared to the value shown in the table. Recent results from NuTeV show [13] that the value of $\sin^2\theta_{\rm W}$ is higher that it is in the table. The difference may come from difference between the distributions of strange and anti-strange sea quarks in the model.

Quantity	Measured value
Mass of W boson	80.425±0.038 GeV
Mass of Z boson	91.188±0.002 GeV
$\sin^2\theta_{\rm W}^{\rm (on-shell)}$	0.225±0.002

mental physics. This is because it has two important defects:

- The model contains 19 free parameters (six quark masses, three charged leptons masses, three CKM mixing angles and a phase, W and Z boson masses, Higgs boson mass, electromagnetic, weak and strong coupling constants) which must be determined experimentally plus another 7 if neutrinos have masses (three masses, three mixing angles and a phase). These parameters cannot be independently calculated.

- The model does not describe the gravitational interaction.

Since the completion of the Standard Model, many efforts have been made to address these problems.

One attempt to address the first defect is known as grand unification. The so-called grand unified theories (GUTs) hypothesized that the SU(3), SU(2), and U(1) groups are actually subgroups of a single large symmetry group. At high energies (far beyond the reach of current experiments), the symmetry of the unifying group is preserved; at low energies, it reduces to SU(3)×SU(2)×U(1) by a process known as spontaneous symmetry breaking. The first theory of this kind was proposed in 1974 by Georgi and Glashow[14], using SU(5) as the unifying group. A distinguishing characteristic of these GUTs is that, unlike the Standard model, they predict the existence of proton decay. In 1999, the Super-Kamiokande neutrino observatory reported that it had not detected proton decay, establishing a lower limit on the proton half-life of 6.7×10^{32} years. This and other experiments have rejected numerous GUTs, including SU(5). Another extension of the Standard Model can be found in the theory of supersymmetry, which

proposes a massive supersymmetric "partner" for every particle. But no evidence of superpartners have been found so far.

In addition, there are cosmological reasons why the standard model is believed to be incomplete. Within it, matter and anti-matter are symmetric. While the preponderance of matter in the universe can be explained by saying that the universe just started out this way, this explanation strikes most physicists as inelegant. Furthermore, the Standard Model provides no mechanism to generate the flatness of the universe and its extraordinary homogeneity, consequences of omission of gravity in the Standard Model.

The Higgs boson, which is predicted by the Standard Model, has not been observed yet (though some phenomena were observed in the last days of the LEP collider that could be related to the Higgs; one of the reasons to build the LHC is that the increase in energy is expected to make the Higgs observable).

The first experimental deviation from the Standard Model came in 1998, when Super-Kamiokande published results indicating neutrino oscillation. This implies the existence of neutrino masses in the case of none-zero mixing anlges. The Standard Model do not accommodate massive neutrinos, because it assumes the existence of only "left-handed" neutrinos, which have spin aligned counter-clockwise to their axis of motion. If neutrinos have non-zero mass, they necessarily travel slower than the speed of light. Therefore, it would be possible to "overtake" a neutrino, choosing a reference frame in which its direction of motion is reversed without affecting its spin (making it right-handed). Since then, physicists have revised the Standard Model to allow neutrinos to have mass, which make up additional free parameters beyond the initial 19.

Synopsis of the thesis

The subject of this work is a determination of the muonic branching ratio of charmed hadrons produced in neutrino charged current interactions. The measurement is based on about 100,000 neutrino interactions found in the emulsion. About 2,000 events from the charged current sample have been manually confirmed as charm decay candidates. This statistics is about fifteen times bigger than one of E531 [15, 16] and about two times larger compared to the previous measurement of the muonic branching ratio by CHORUS collaboration [17]. On top of that, the method to extract the ratio is based only on the secondary tracks and the muon identification procedure is totally different from the previous measurement by CHORUS which significantly improves the systematic error.

Another subject covered in this thesis is related to extraction of V_{cd} CKM matrix element and to study of Bjorken x distributions. It is worth to mention that the analyses related to charm production are not finished. Here only the analyses framework is discussed and preliminary results of the methods are shown.

The chapters of the thesis are organized as follows:
Chapter 1 provides the theoretical framework of the analysis.
Chapter 2 describes the experimental setup including the beam and the electronic detectors.
Chapter 3 contains the detailed description of the Netscan technique to scan the emulsion and to reconstruct the events.
Chapter 4 is devoted to the measurement of muonic branching ratio of charmed hadrons.
Chapter 5 is related to the preliminary results on charm production, the measurement of x-distribution and $|V_{cd}|$.

Chapter 1

Neutrino-nucleon scattering

The chapter covers the theoretical framework of the charged current neutrino scattering on a nucleon and charm production.

1.1 Deeply inelastic scattering kinematics

A deeply inelastic scattering (DIS) process is generally of the form

$$l(k) + h(p) \rightarrow l'(k') + X, \tag{1.1}$$

where $l(k)$ represents an incident lepton of four-momentum k^μ, l' is an outgoing lepton of momentum k'^μ,$h(p)$ a hadron of momentum p^μ and X an arbitrary hadronic state. In our case, l is a neutrino, l' is a muon, $h(p)$ is either a proton or a neutron. The process illustrated in Fig. 1.1, is initiated by the exchange of vector boson W. The discussion of DIS, more than that of any other cross-section, is couched in a rather specialized kinematic notation, which we shall briefly review. The usage of the kinematic notation goes beyond the models describing leptoproduction: the parton model and even perturbative Quantum Chromodynamics (pQCD). For example, description of interactions between hadrons and nuclei is based on similar notation.

In charged current neutrino interactions, the momentum transfer between lepton and hadron, q, is space-like,

$$\begin{aligned} q^\mu &= k^\mu - k'^\mu, \\ -q^2 &= Q^2. \end{aligned} \tag{1.2}$$

In addition, as the term implies, in DIS the hadronic final state X has an invariant mass much larger than that of the nucleon. This is normally

Figure 1.1: Deeply inelastic scattering.

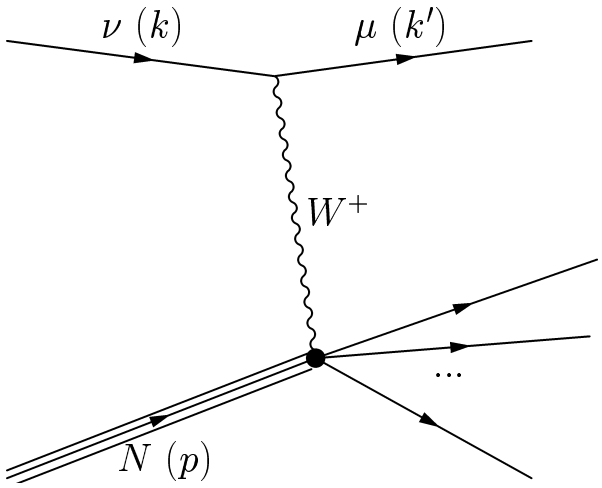

parametrized in terms of the Bjorken scaling variable x,

$$x = \frac{-q^2}{2p \cdot q} = \frac{Q^2}{2M\nu}, \tag{1.3}$$

where M is the mass of the nucleon, ν is the energy transfered from the lepton to the nucleon in the nucleon(target) rest frame,

$$\nu = E_k - E_{k'} = p \cdot q/M. \tag{1.4}$$

ν is naturally related to the dimensionless variable y,

$$y = \frac{p \cdot q}{p \cdot k} = \frac{E_k - E_{k'}}{E_k} = \frac{\nu}{E_k}, \tag{1.5}$$

which measures the ratio of the energy transfered to the hadronic system to the total leptonic energy available in the target rest frame. This variable also has a very simple interpretation in the parton model. If we denote $\hat{\theta}$ as a lepton scattering angle in the lepton-quark center of mass frame then

$$\begin{aligned} y = \frac{\nu}{E_k} &= \frac{2M\nu}{s_{\mathrm{m}}} = \frac{Q^2}{x s_{\mathrm{m}}} = -\frac{(k-k')^2}{x s_{\mathrm{m}}} = \\ &= \frac{s_{\mathrm{m}}(1-\cos\hat{\theta})}{2 s_{\mathrm{m}}} = \frac{1-\cos\hat{\theta}}{2} = \sin^2\frac{\hat{\theta}}{2}, \end{aligned} \tag{1.6}$$

where $s_{\rm m} = (k_\mu + p_\mu)^2$ is the usual Mandelstam varibale.

For a nucleus with mass number A, it is usually convenient to rescale x by A, so that the denominator in Eq. 1.3 is still the mass of the nucleon. For fixed x, the mass of the hadronic final state is given by

$$W^2 = M^2 + \frac{Q^2}{x}(1-x). \tag{1.7}$$

Thus, for x fixed and Q^2 large, the mass of the hadronic final state is also large.

The incoming lepton may be an electron, a muon, or a (anti)neutrino, and the exchanged vector boson a photon, $W^\pm$, or Z. At lowest order in electroweak interactions, the cross-section of neutrino scattering on a nucleon may be split into leptonic and hadronic parts,

$$d\sigma = \frac{d^3k}{2s|k'|}\frac{c_{\rm V}^4}{4\pi^2(q^2-m_{\rm V}^2)} L_{lV}^{\mu\nu}(k,q) W_{\mu\nu}^{Vh}(p,q) \ , \tag{1.8}$$

where V labels the exchanged vector boson, of mass m_V, and where $c_{\rm V}$ can be:

$$c_{W^\pm} = \frac{g}{2\sqrt{2}} \ , c_\gamma = e \tag{1.9}$$

Note that each weak-interaction coupling involves $g = e/\sin\theta_W$. In this equation, we neglect the gauge- and mass-dependent term $q_\alpha q_\beta/m_{\rm W}$ in the vector-boson propagator $(g_{\alpha\beta} - q_\alpha q_\beta/m_V^2)/(q^2 - m_V^2)$. Corrections to this approximation are proportional to the ratio m_l/m_V for $V = W^\pm$ and are neglected in further calculations.

The leptonic tensors can be evaluated explicitly from

$$L_{lV}^{\mu\nu}(k,q) = \overline{\sum_{\rm spin}} \bar{u}(k)\Gamma^\mu u(k') \cdot \bar{u}(k')\Gamma^{\nu\dagger} u(k) = {\rm Tr}[k\Gamma^\mu k'\Gamma^{\nu\dagger}] \ , \tag{1.10}$$

where the last equation is true for a completely polarized neutrino beam and the coupling in the most general form reads

$$\Gamma^\mu = \gamma^\mu[g_{{\rm R}l}(1+\gamma_5) + g_{{\rm L}l}(1-\gamma_5)] \ . \tag{1.11}$$

Substituting Eq. 1.11 to Eq. 1.10 gives

$$\begin{aligned} L^{\mu\nu}(k,q) &= \overline{u}(k)\gamma_\mu(1-\gamma_5)u(k') \cdot \overline{u}(k')\gamma_\nu(1-\gamma_5)u(k) \\ &= 8\big[k_\mu k'_\nu + k_\nu k'_\mu - g_{\mu\nu} k\cdot k' \mp i\epsilon_{\mu\nu\alpha\beta}k^\alpha k'^\beta\big] \end{aligned} \tag{1.12}$$

where the last term's sign plus(minus) refers to incident neutrinos(anti-neutrinos) respectevely.

The hadronic tensor, on the other hand, is defined to all orders in the strong interaction in terms of the matrix elements

$$W_{\mu\nu}^{(Vh)}(p,q) = \frac{1}{8\pi}\sum_{\sigma}\sum_{X} < h(p,\sigma)|j_{\mu}^{V\dagger}(0)|X > \\ \times < X|j_{\nu}^{V}(0)|h(p,\sigma) > (2\pi)^4\delta^4(p+q-p_X) \ . \tag{1.13}$$

Here, $j_{\mu}^{V}(x)$ is the appropriate electroweak current operator, labeled by the corresponding vector boson and divided by the appropriate c_V (see Eq. 1.9). When appropriate, we average over the nucleon spin σ, which simplifies our analysis. We have performed this average in Eq. 1.13, and the normalization factor includes a factor $1/2$ for this average.

The hadronic tensor is a second rank tensor which parametrizes the structure of the boson-nucleon vertex. There are only two independent vectors upon which $W_{\mu\nu}$ can depend – p and q. The most general rank-2 tensor can be constructed by expanding it in terms of scalar *structure functions* $W_i^{(Vh)}$

$$W_{\mu\nu}^{(Vh)} = -g_{\mu\nu}W_1^{(Vh)}(x,Q^2) + \frac{p_\mu p_\nu}{M^2}W_2^{(Vh)}(x,Q^2) - \\ -i\frac{\epsilon^{Pq\mu\nu}}{2M^2}W_3^{(Vh)}(x,Q^2) + \frac{q_\mu q_\nu}{M^2}W_4^{(Vh)}(x,Q^2) + \\ +\frac{p_\mu q_\nu + q_\mu p_\nu}{2M^2}W_5^{(Vh)}(x,Q^2) + \frac{p_\mu q_\nu - q_\mu p_\nu}{2M^2}W_6^{(Vh)}(x,Q^2) \ , \tag{1.14}$$

where $\epsilon^{Pq\mu\nu} = \epsilon^{\alpha\beta\mu\nu}p_\alpha q_\beta$. The structure functions $W_i^{(Vh)}$ are Lorentz scalars that depend on q^2 and $p\cdot q$, and, in general, they depend on the target and on the incident lepton. Note that there is a variety of conventions in the literature about the definition of W_i and of the variable ν. Our conventions for the W_i's are consistent with those in Ref. [18].

It is worth noting that the hadron structure functions W_4, W_5, W_6 do not enter to the cross section because they are multiplied by factors proportional to the lepton mass from the lepton vertex and give minor contribution to the cross section.

The structure functions are generally parametrized in terms of x and Q^2. At this stage, there is no relation between the $W_i^{(Vh)}$ for different bosons V.

The functions W_i of Eq. 1.14 are usually replaced, for the purposes of exhibiting data, by alternate, but equivalent, structure functions F_i, which

will turn out to be particularly simple in the parton model,

$$\begin{aligned} F_1(x,Q^2) &= W_1(x,Q^2), \\ F_2(x,Q^2) &= \frac{\nu}{M} W_2(x,Q^2), \\ F_3(x,Q^2) &= \frac{\nu}{M} W_3(x,Q^2). \end{aligned} \tag{1.15}$$

Yet another equivalent basis for the structure functions is inspired by assigning polarizations to the vector boson V, in the target rest frame:

$$\begin{aligned} \epsilon_R(q) &= \frac{1}{\sqrt{2}}(0;1;-i;0), \\ \epsilon_L(q) &= \frac{1}{\sqrt{2}}(0;1;i;0), \\ \epsilon_{\text{long}}(q) &= \frac{1}{\sqrt{Q^2}}(\sqrt{Q^2+\nu^2};0;0;\nu). \end{aligned} \tag{1.16}$$

This corresponds to helicities of +1, -1 and to longitudinal (sometimes called "scalar") polarization for the exchanged particle, respectively. Up to corrections of order M^2/Q^2, $W_{\mu\nu}^{(Vh)}$ has the expansion

$$W_{\mu\nu}^{(Vh)} = \sum_{\lambda} \epsilon_\lambda^*(q)_\mu \epsilon_\lambda(q)_\nu F_\lambda^{(Vh)}(x,q^2), \tag{1.17}$$

where $\lambda = \text{L},\ \text{R},\ \text{long}$ labels the helicity. In this approximation, the "helicity" structure functions are related to the structure functions of Eq.1.15 by the simple relations

$$F_{\text{L,R}} = F_1 \pm F_3, F_{\text{long}} = \frac{F_2}{2x} - F_1. \tag{1.18}$$

The notation in terms of helicities is useful in calculation of mass threshold effects discussed later in Section 1.3.

The structure functions can be found directly from the experiments in which only the outgoing lepton's momentum is measured. For instance, the differential cross-section in terms of the dimensionless variables x and y may be rewritten in terms of incoming and outgoing leptons energies and scattering angle in the target rest frame as

$$\begin{aligned} \frac{d^2\sigma^{(lh)}}{dxdy} = \frac{E_{k'}y}{M} N^{(lV)} \Big[& 2W_1^{(Vh)}(x,q^2)\sin^2(\theta/2) + W_2^{(Vh)}(x,q^2)\cos^2(\theta/2) \pm \\ & W_3^{(Vh)}(x,q^2)\frac{E_k + E_{k'}}{M}\sin^2(\theta/2) \Big] , \end{aligned} \tag{1.19}$$

where the $\pm$ corresponds to $V = W^{\pm}$, and where

$$N^{(\nu W^+)} = N^{(\bar{\nu} W^-)} = \pi\alpha^2 \frac{ME}{2\sin^4(\theta_W)(Q^2 + M_W^2)^2} \ . \tag{1.20}$$

Here, θ_W is the weak mixing angle, and $\pi\alpha^2/(2M_W^4 \sin^4\theta_W) = G_{\rm F}^2/\pi$, with $G_{\rm F}$ the Fermi constant.

Other useful expressions for the cross-section are given directly in terms of y,

$$\frac{d^2\sigma^{(lh)}}{dxdy} = N^{lV}\Big[\frac{y^2}{2} 2xF_1^{(Vh)} + \big(1 - y - \frac{Mxy}{2E}\big)F_2^{(Vh)} + \delta_V\big(y - \frac{y^2}{2}\big)xF_3^{(Vh)}\Big], \tag{1.21}$$

where δ_V is +1 for $V = W^+$ (neutrino beam), -1 for $V = W^-$ (anti-neutrino beam), while M is the target hadron mass as before.

The experimental results from different experiments are shown in Fig. 1.2.

Figure 1.2: $\sigma_{\rm T}/E_\nu$, for the muon neutrino and anti-neutrino charged-current total cross section as a function of neutrino energy. The error bars include both statistical and systetic errors. The straight lines are the averaged values over all energies as measured by the experiments in Ref [19, 20, 21, 22] = $0.677 \pm 0.014 (0.334 \pm 0.008) \times 10^{-38}$ cm^2/GeV. There is a change in energy scale at 30 GeV.

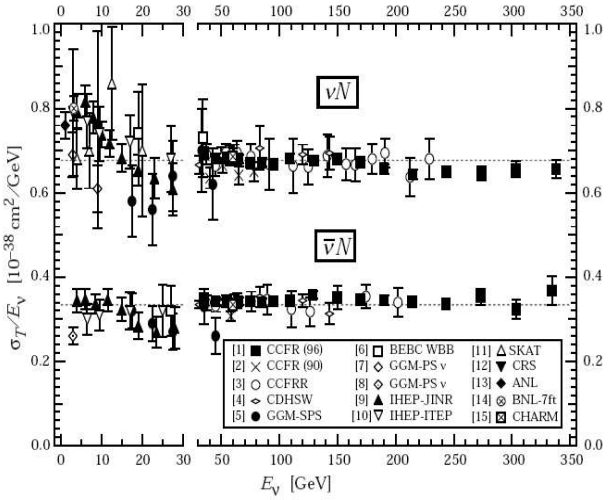

1.1.1 Cross sections and parton distributions

Now let us see what the parton model has to say about deep-inelastic scattering. In the parton model the scattering on the nucleon is due entirely to the scattering on its individual constituents. If these constituents are quarks and gluons, then only quarks will couple to electroweak currents in the Born approximation. The DIS cross section is then given by the probability $q^{\mathrm{T}}(\xi)$ of finding a quark of flavor q and fractional momentum ξ in hadron T, times the cross section for the *elastic* scattering of that parton.

A typical parton-model DIS cross section is therefore given by

$$\frac{d\sigma^{(lT)}}{dE_{k'}d\Omega_{k'}}(p,q) = \sum_q \int_0^1 d\xi \frac{d\sigma^{(lf)}_{Born}}{dE_{k'}d\Omega_{k'}}(\xi p, q) q^{\mathrm{T}}(\xi). \tag{1.22}$$

The distribution q^{T} is undetermined at this point. The perturbative equivalent of the parton-model picture of DIS is illustrated, in "cut diagram" notation, in Figure 1.3 (left).

We note the absence of diagrams such as Fig. 1.3 (right), in which the scattering of quark q with fraction ξ interferes with the scattering of a quark of fraction ξ', the momentum being made up by an extra gluon. This feature is referred to as the "incoherence" of the parton model.

From the Eqs. 1.8, 1.14 and 1.15 we derive relations for the structure

Figure 1.3: Parton-model picture of deep-inelastic scattering. Left: parton-model scattering. Right: the interference graph. The vertical line indicates the sum over all possible hadronic final states. V stands for a vector boson.

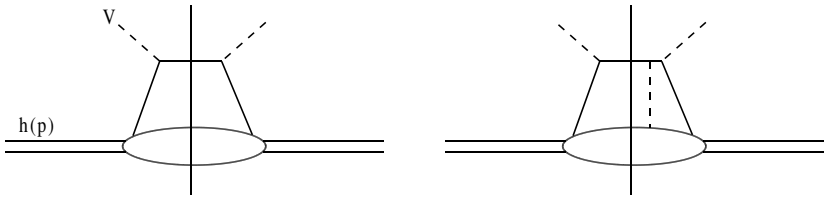

Figure 1.4: Born-level diagram.

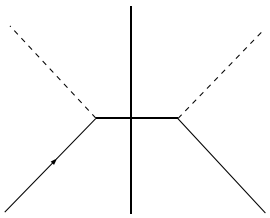

functions F_i in the parton model,

$$F_a^{(Vh)} = \sum_q \int_0^1 \frac{d\xi}{\xi} F_a^{(Vq)}(x/\xi) q^{\mathrm{T}}(\xi) (a = 1, 3), \tag{1.23}$$

$$F_2^{(Vh)} = \sum_q \int_0^1 d\xi F_2^{(Vq)}(x/\xi) q^{\mathrm{T}}(\xi). \tag{1.24}$$

Here the $F_i^{(Vq)}$ are the structure functions at the parton level; they can be calculated from the Born diagram of Fig 1.4. The factor $1/\xi$ in Eq. 1.23 arises from the normalization of the parton states and from the factors p in the definition of the structure functions from $W_{\mu\nu}$. The vector p^μ must be changed to ξp^μ for scattering on a parton.

It is worth stressing that the difference between electromagnetic and weak interactions at this stage is limited mainly to the coefficients. All the calculations above can be easily rewritten for the (γh) vertex. To show this fact, let us write the hadronic tensor for the scattering off a quark mediated by a photon and write down the explicit relations between the structure functions. For the electromagnetic scattering, we have

$$(W_{\mu\nu}^{(\gamma q)})_{Born} = \frac{1}{8\pi} \int \frac{d^3p'}{(2\pi)^3 2\omega_{p'}} Q_f^2 \mathrm{Tr}[\gamma_\mu(\hat{p} + \hat{q})\gamma_\nu \hat{p}] \times (2\pi)^4 \delta^{(4)}(p' - p - q), \tag{1.25}$$

where eQ_q is the electric charge of the quark of flavor q. A factor e has been absorbed into c_γ in Eq. 1.9. This gives

$$2F_1^{(\gamma q)}(x) = F_2^{(\gamma q)}(x) = Q_q^2 \delta(1 - x). \tag{1.26}$$

Substituting these functions into 1.23 and 1.24, we find the electromagnetic

structure functions in terms of quark distributions,

$$2xF_1^{(\gamma h)}(x) = F_2^{(\gamma h)}(x) = \sum_q Q_q^2 x q^{\mathrm{T}}(x). \tag{1.27}$$

Two important aspects of these expressions are (i) the structure functions depend on the Bjorken scaling variable x only, and not on the momentum transfer directly; (ii) the two functions satisfy the relation $2xF_1 = F_2$.

The first result is known as *scaling* [23]. Its observation [24, 25, 26] was the inspiration for the parton model. The second, known as the *Callan-Gross relation* [27] follows from the specific of the Born diagram, Fig. 1.4, and as such is evidence of the spin 1/2 nature of charged partons (the quarks).

Evidently, measuring F_1 or F_2 immediately gives an experimental determination of the combination of distributions, $\sum_q Q^2 q^{\mathrm{T}}(x)$ for T a proton or a neutron. Now isospin invariance implies the following relations between the quark distributions

$$\begin{aligned} u^p &= d^n, \\ d^p &= u^n, \end{aligned} \tag{1.28}$$

with u the up and d the down quark. In the approximation that the proton and the neutron contain u and d quarks only, a measurement of F_2 for p and n, combined with Eq. 1.28, determines the distributions u^{T} and d^{T}. These distributions can then be used to predict other DIS cross sections, such as neutrino scattering, to the same approximation.

Of course, in real life things are not so simple. Quantum mechanics tells us that virtual states will include quark-antiquark pairs of every flavor. These are called sea quarks in opposition to the valence quarks responsible of the identity of the different hadrons. The sum in Eq. 1.27 will therefore include strange, charm, and even the bottom and top quarks, with their anti-quarks. Although we may expect that the contribution of very heavy quark pairs in a nucleon is relatively small, we clearly need more information to determine the distributions of light quarks, for instance. For this purpose, we shall find neutrino and anti-neutrino scattering ideal.

Scaling of the structure functions at high Q^2 is explained by the parton model. The deep inelastic scattering environment is described in a highly relativistic frame – the so-called infinite momentum frame. In this frame, quarks interact among themselves on time scale much longer than that of the collision, so the scattering is incoherent. Inelastic neutrino-nucleon scattering reduces to elastic scattering on free, individual partons. The partons

are on-shell, they travel collinearly with the nucleon and carry a fraction ξ of its momentum.

Elastic scattering of point particles depends only on the center of mass energy and the net angular momentum of the system. Assuming that neutrinos have no mass, neutrinos are left-handed and anti-neutrinos are right-handed. A similar assumption is made for the quarks and anti-quarks. Considering spin 1/2 and spin 0 constituents of the nucleon, the possible helicity dependent cross sections for elastic neutrino-parton scattering are given by

$$\begin{aligned}
\frac{d\sigma^{\nu q}}{d\cos\hat{\theta}} = \frac{d\sigma^{\bar{\nu}\bar{q}}}{d\cos\hat{\theta}} &= \frac{G_{\mathrm{F}}^2 M E_\nu}{\pi(1+Q^2/M_W^2)^2} \text{ (total spin 0)} \quad , \\
\frac{d\sigma^{\nu\bar{q}}}{d\cos\hat{\theta}} = \frac{d\sigma^{\bar{\nu}q}}{d\cos\hat{\theta}} &= \frac{G_{\mathrm{F}}^2 M E_\nu}{\pi(1+Q^2/M_W^2)^2}\Big(\frac{1+\cos\hat{\theta}}{2}\Big)^2 \text{ (total spin 1)} \quad , \\
\frac{d\sigma^{\nu k}}{d\cos\hat{\theta}} = \frac{d\sigma^{\bar{\nu}k}}{d\cos\hat{\theta}} &= \frac{2G_{\mathrm{F}}^2 M E_\nu}{\pi(1+Q^2/M_W^2)^2}\Big(\cos\frac{\hat{\theta}}{2}\Big)^2 \text{ (total spin } \frac{1}{2}\text{)} \quad , \qquad (1.29)
\end{aligned}$$

where $\hat{\theta}$ is the muon's center of mass scattering angle and which is related to y by Eq. 1.6 and the sum is made on all quark flavour in the final state. The superscripts identify the spin 1/2 partons with the quarks and anti-quarks. In reality, partons have transverse component of the momentum. Technically, this is attributed to spin 0 constituent, which is identified by the superscript k. The V–A structure of the weak interaction causes spatial parity to be maximally violated, so for massless partons only left-handed particles and right-handed antiparticles participate. The possible configurations for high energy neutrino-quark scattering are shown in Figure 1.5.

The probability of scattering from a particular type of parton is introduced with a parton distribution function $p(x)$. The quantity $p(x)dx$ is interpreted as the probability of finding a parton of type p in a hadron carrying a fraction x to $x+dx$ of the hadron's momentum. Then using the parton momentum distribution function $xp(x)$, the differential cross section for scattering off one parton is

$$\frac{d^2\sigma}{dxdy} \sim \frac{G_{\mathrm{F}}^2 2ME_\nu}{\pi(1+Q^2/M_W^2)^2} xp(x) \qquad (1.30)$$

and gathering all contributions from the constituents of a target T, the cross

sections for neutrino and anti-neutrino scattering are

$$\frac{d^2\sigma^{\nu\mathrm{T}}}{dxdy} = \frac{G_\mathrm{F}^2 xs}{\pi(1+Q^2/M_\mathrm{W}^2)^2}\big[q^{\nu\mathrm{T}}(x) + (1-y)^2\bar{q}^{\nu\mathrm{T}}(x) + \\ +2(1-y)k^{\nu\mathrm{T}}(x)\big]\ , \tag{1.31}$$

$$\frac{d^2\sigma^{\bar{\nu}\mathrm{T}}}{dxdy} = \frac{G_\mathrm{F}^2 xs}{\pi(1+Q^2/M_\mathrm{W}^2)^2}\big[\bar{q}^{\bar{\nu}\mathrm{T}}(x) + (1-y)^2 q^{\bar{\nu}\mathrm{T}}(x) + \\ +2(1-y)k^{\bar{\nu}\mathrm{T}}(x)\big]\ . \tag{1.32}$$

The parton distributions are associated with the structure functions by comparing the y dependences of the above formulas with Eq. 1.21, yielding:

$$2xF_1^{\nu(\bar{\nu})\mathrm{T}} = 2\big[xq^{\nu(\bar{\nu})\mathrm{T}}(x) + x\bar{q}^{\nu(\bar{\nu})\mathrm{T}}\big], \tag{1.33}$$

$$F_2^{\nu(\bar{\nu})\mathrm{T}} = 2\big[xq^{\nu(\bar{\nu})\mathrm{T}}(x) + x\bar{q}^{\nu(\bar{\nu})\mathrm{T}}(x) + 2xk^{\nu(\bar{\nu})\mathrm{T}}(x)\big], \tag{1.34}$$

$$xF_3^{\nu(\bar{\nu})\mathrm{T}} = 2\big[xq^{\nu(\bar{\nu})\mathrm{T}}(x) - x\bar{q}^{\nu(\bar{\nu})\mathrm{T}}\big], \tag{1.35}$$

Figure 1.5: Possible helicity configurations in the scattering between neutrinos or antineutrinos and quarks or antiquarks. a) corresponds to the case where both spins are opposite yielding total spin 0, realized in neutrino-quark or antineutrino-antiquark scattering. b) corresponds to the case where both spins are parallel yielding total spin 1, realized in neutrino-antiquark or antineutrino-quark scattering.

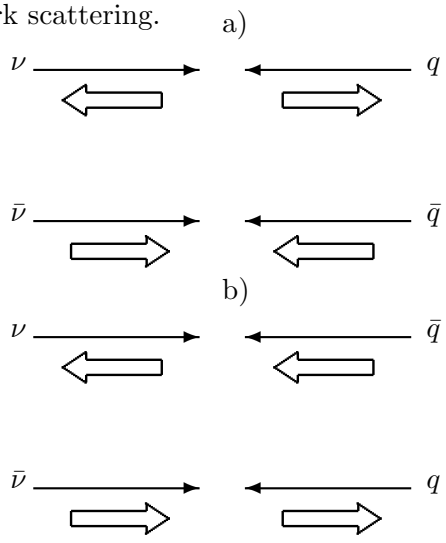

where the term proportional to Q^2/ν^2 has been dropped out. Thus, in the parton model, deep inelastic structure functions are simply related to the momentum fractions of the partons in the target.

Neutrino scattering has the ability to resolve the nucleon constituents. The charge conservation and the absence of quarks with electrical charge greater than that of electron limit neutrinos to scatter from d, s, $\bar{u}$ and $\bar{c}$. Finally, the quark densities that contribute to the structure functions are:

$$\begin{aligned} q^{\nu p}(x) &= q^{\nu n}(x) = d(x) + s(x), \\ \bar{q}^{\nu p}(x) &= \bar{q}^{\nu n}(x) = \bar{u}(x) + \bar{c}(x), \\ q^{\bar{\nu} p}(x) &= q^{\bar{\nu} n}(x) = u(x) + c(x), \\ \bar{q}^{\bar{\nu} p}(x) &= \bar{q}^{\bar{\nu} n}(x) = \bar{d}(x) + \bar{s}(x). \end{aligned} \tag{1.36}$$

(1.37)

Here, we have assumed the strong isospin symmetry Eq. 1.28 and that the sea quarks (s and c) have the same distributions in proton and neutron. Also an assumption is made that the sea anti-quarks are distributed exactly as the sea quarks and that the contribution from the heavy quarks b and t is neglected. Recent results show [28, 29] that the latter is not true in the low x region. This will be discussed later in the x-distributions chapter.

1.2 Quantum Chromodynamics

The parton model explains the scaling of the structure functions in terms of spin 1/2 point-like constituents, but by itself offers no explanation for the dynamics between the constituents. The need to refine the parton model was also apparent from detailed studies of structure functions, which found that scaling is only an approximate phenomenon, and that logarithmic scaling violations are present. Advances in understanding of non-Abelian gauge group theories led to Quantum Chromodynamics. QCD provides a consistent theory of quark dynamics, explains the scaling violations of the structure functions, and offers the detailed phenomenology formalism of deep inelastic scattering.

There are two important consequences of non-Abelian structure of QCD: confinement and asymptotic freedom. Quarks are confined in a hadron because the self-interactions of gluons tend to anti-screen a color charge, so that the strong force between two quarks increases as the distance between the quarks gets larger. This effect is known as quark confinement. However, at shorter distances (or equivalently, larger momentum transfers), the strong

coupling α_s decreases, so that as the momentum transfer $Q^2 \to \infty$, $\alpha_s \to 0$, and the quarks begin to act as free particles.

Similar to Quantum Electrodynamics, the inclusion of higher order or loop diagrams leads to terms that are ultraviolet divergent. These terms involve integrals of the form $1/(k^2 - m^2)^2$ and may be thought of as virtual states in which energy conservation is violated by an arbitrary large amount. As any other meaningful quantum field theory QCD is renormalizable. The renormalization involves introducing a free parameter μ_R^2, which is called renormalization scale. A calculation of observable quantities, like a cross section, must be independent of the scale. This requirement is expressed in the form of the renormalization group equation

$$\mu \frac{\mathcal{M}}{d\mu} = 0, \tag{1.38}$$

the renormalization group being the set of all rescalings μ^2. Then, to the next-to-leading order, the renormalization scale dependence of the coupling constant α_s is given by the beta functions

$$\mu \frac{d\alpha_s(\mu^2)}{d\mu} = -\frac{\beta_1}{2\pi}\alpha_s^2(\mu^2) - \frac{\beta_2}{8\pi^2}\alpha_s^3(\mu^2) + \mathcal{O}(\alpha_s^4(\mu^2)), \tag{1.39}$$

where the coefficients are given by

$$\begin{aligned} \beta_1 &= 11 - 2n_f/3, \\ \beta_2 &= 102 - 38n_f/3, \end{aligned} \tag{1.40}$$

and n_f is the number of quark flavors. The positive contributions come mainly from non-Abelian diagrams and the negative ones depending on n_f, which weaken asymptotic freedom, come from fermion loop diagrams. The solution to Eq.1.39 is usually given in terms of the dimensional parameter Λ:

$$\frac{\alpha_s(\mu^2)}{4\pi} = \frac{1}{\beta_1 \ln(\mu^2/\Lambda^2)} - \frac{\beta_2 \ln[\ln(\mu^2/\Lambda^2)]}{\beta_1^3 \ln^2(\mu^2/\Lambda^2)} + O\Big(\frac{1}{\ln^3(\mu^2/\Lambda^2)}\Big). \tag{1.41}$$

Therefore, measurement of Λ is equivalent to measuring $\alpha_s(\mu_0^2)$. Λ effectively sets the scale of the running coupling constant, and so it marks the boundary between quasi-free quarks and gluons and hadronic bound states.

There are several ways of making renormalization. The set of rules that specify the value of the renormalization scale for each divergent diagram describes the renormalization scheme that is used. One of the most popular

schemes is $\overline{\text{MS}}$ or minimal subtraction scheme. In this scheme the parton distributions are defined directly in terms of hadronic matrix elements. If renormalization is carried out according to the $\overline{\text{MS}}$ scheme then the corresponding Λ is called $\Lambda_{\overline{\text{MS}}}$.

1.2.1 Factorization theorem

In perturbative QCD the parton model is generalized by the theorem of factorization of long-distance from short-distance dependence of deeply inelastic scattering [30, 31]. Phrased differently, the structure functions can be decomposed into two parts, a parton distribution and a hard scattering function. The theorem can be expressed in the following way

$$\begin{aligned} W^{\alpha\beta}(q,p) &= \sum_a \int_\xi^1 \frac{d\xi}{\xi} \hat{\omega}_a^{\alpha\beta}(q,\xi p,\Lambda,\alpha_{\text{s}}(\mu_{\text{R}}))\phi_a(\xi,\Lambda,\mu^2) \\ &= \sum_a \hat{\omega}_a^{\alpha\beta}(q,\xi p,\Lambda,\alpha_{\text{s}}(\mu_{\text{R}})) \otimes \phi_a(\xi,\Lambda,\mu^2). \end{aligned} \tag{1.42}$$

Here, the sum is over all partons a: quark, gluons, and anti-quarks. The integration is made over all parton momentum fractions ξ. The hard-scattering function $\hat{\omega}^{\alpha\beta}$ describes the probability for the scattering to take place and is infrared safe, calculable in perturbation theory. It depends upon the label a, the exchange boson, on the parton, and on the renormalization and factorization scales, but it is independent of long-distance effects. For example, it is independent of the identity of the hadron h. The parton distribution ϕ contains all the infrared sensitivity of the cross sections, it also depends on Λ and is particular for each hadron h. However, it is independent of the particular scattering process. The parton distributions are to be determined from the experiment once the hard-scattering functions are evaluated.

Generally speaking, μ_{R} and Λ need not to be equal. The former is the renormalization scale and is necessary for any perturbation theory. The latter is specific for the factorization and serves as a separator between short-distance and long-distance effects. Roughly speaking, any propagator that is off-shell by Λ^2 or more enters into the hard-scattering function $\hat{\omega}^{\alpha\beta}$ and ϕ otherwise.

1.2.2 Evolution of the parton distributions

Up to this point we were carrying out the discussion at fixed Q^2. A remarkable feature of QCD is that once the parton distributions are measured at one Q^2 scale, QCD predicts how they evolve to any other Q'^2. This fact

enormously improves the predictive power of QCD. The evolution of parton distributions is governed by the Gribov-Lipatov-Altarelli-Parisi equations [32, 33]:

$$\frac{dq_{\rm NS}(x,t)}{dt} = \int_x^1 \frac{dy}{y} P_{qq}^{\rm NS}(\frac{x}{y},t) q_{\rm NS}(y,t), \tag{1.43}$$

$$\frac{dq_{\rm S}(x,t)}{dt} = \int_x^1 \frac{dy}{y} \Big[P_{qq}^{\rm S}(\frac{x}{y},t) q_s(y,t) + 2N_f P_{qG}(\frac{x}{y},t) g(y,t) \Big], \tag{1.44}$$

$$\frac{dG(x,t)}{t} = \int_x^1 \frac{dy}{y} \Big[P_{Gq}(\frac{x}{y},t) + P_{GG}(\frac{x}{y},t) g(y,t) \Big], \tag{1.45}$$

where $t = \ln(\mu^2/\Lambda)$. The non-singlet ("valence") and singlet quark distributions are given by

$$\begin{aligned} q_{\rm NS}(x,t) &= \sum_i [q_i(x,t) - \bar{q}_i(x,t)], \\ q_{\rm SI}(x,t) &= \sum_i [q_i(x,t) + \bar{q}_i(x,t)], \end{aligned} \tag{1.46}$$

and the gluon distribution is denoted as $g(x,t)$. The evolution kernels $P_{qq'}$ express the tendency for a parton of type q' carrying a momentum fraction y to be resolved as a parton of type q with the momentum fraction $x < y$. The splitting functions $P_{qq'}$ take into account the radiative corrections and can be calculated at any order. The splitting function diagrams are shown in Fig. 1.6.

To summarize, consider the relation between the structure functions $F_a^{(Vh)}$, $V = W^{\pm}$, and the physical parton distributions $q^h(x,\mu^2)$. The method is as follows:

- (a) Calculate the infrared-regulated distributions q and g to some order in the perturbation theory,
- (b) Calculate $F_a^{(Vj)}$, with $j = q, g$ to the same order,
- (c) Combine the results of (a) and (b) to derive $\hat{\omega}_a^{\alpha\beta}$ to this order,
- Combine $\hat{\omega}_a^{\alpha\beta}$ with experimentally determined $F_a^{(Vh)}$ to obtain the non-perturbative q^h to the same order in perturbation theory by applying the factorization theorem.

These distributions can be combined with the hard-scattering functions from other processes to derive the predictions from the theory unless the factorization scheme is consistent in both cases.

Figure 1.6: Altarelli-Parisi splittings. Top: diagrams that contribute to the leading order splitting functions. Bottom: The next-to-leading-order splitting function diagrams.

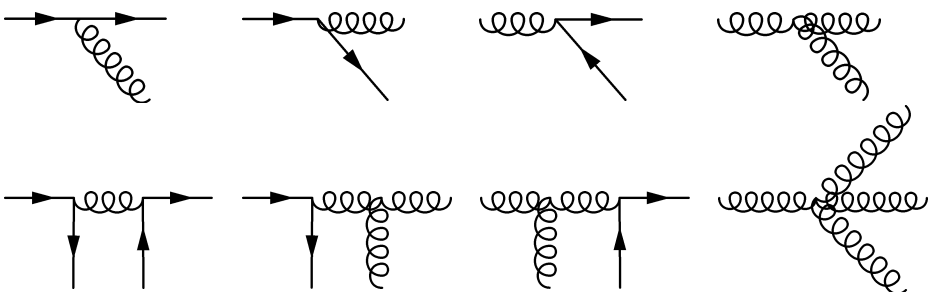

1.3 Mass threshold effects

In the previous sections we were considering the leptons and the partons to be massless. This is a good approximation for the large momentum transfer. However, average momentum transfer for CHORUS is of the same order as the charm quark mass and the mass of the nucleon, and these two effects are to be taken into account. This also leads to the violation of the Callan-Gross relation $2xF_1 = F_2$. The difference decreases as the momentum transfer Q^2 increases.

Recent calculations [18, 34] give a description of both effects by using a suitable reference frame, taking the axis along the direction of the W boson. This procedure is referred to as the "helicity formalism" since this choice of basis provides a natural separation of the structure functions for different W boson helicities 1.17. To fix this coordinate system, we define polarization vectors for a W boson with momentum q in the target nucleon rest frame as

$$\epsilon_{\mathrm{L}}(q) = \frac{1}{\sqrt{2}}(0,1,i,0) \ , \tag{1.47}$$

$$\epsilon_{\mathrm{R}}(q) = \frac{1}{\sqrt{2}}(0,1,-i,0) \ , \tag{1.48}$$

$$\epsilon_{\mathrm{l}}(q) = \frac{1}{\sqrt{-q^2}}(\sqrt{-q^2+\nu^2},0,0,\nu) \ , \tag{1.49}$$

corresponding to left-handed, right-handed and longitudinally polarized bo-

sons, respectively. The longitudinally polarized case is often called as 'scalar'. With these definitions, we can replace the tensor decomposition of equation 1.14 with a helicity decomposition:

$$W^{\alpha}_{\beta} \;=\; \sum_{\lambda=\mathrm{L,R,l}} \epsilon^{*}_{\lambda}(p,q)^{\alpha}\epsilon_{\lambda}(p,q)_{\beta}F_{\lambda}(x,q^2)\;, \tag{1.50}$$

where the dependence of ϵ on the coordinate system is indicated through the argument p, the four-momentum of the target nucleon. The helicity decomposition can be inverted to obtain a definition of the helicity structure functions F_{λ}:

$$F_{\lambda=L,R,l} \;=\; \epsilon^{*}_{\lambda}(p,q)_{\alpha}\; W^{\alpha}_{\beta}\; \epsilon_{\lambda}(p,q)^{\beta}\;. \tag{1.51}$$

The correspondence between the helicity structure functions and scaling structure functions can be worked out to obtain

$$F_{\mathrm{L}} \;=\; F_1 \;+\; \frac{1}{2}\sqrt{1+\frac{Q^2}{\nu^2}}\,F_3\;, \tag{1.52}$$

$$F_{\mathrm{R}} \;=\; F_1 \;-\; \frac{1}{2}\sqrt{1+\frac{Q^2}{\nu^2}}\,F_3\;, \tag{1.53}$$

$$F_{\mathrm{long}} \;=\; -\,F_1 \;+\; \left(1+\frac{Q^2}{\nu^2}\right)\frac{1}{2x}\,F_2\;. \tag{1.54}$$

Note that the zero target mass limit $M^2/Q^2 \to 0$ is equivalent to $Q^2/\nu^2 = 4x^2M^2/Q^2 \to 0$, which implies $F_{\mathrm{L}} = F_1 + F_3/2$, $F_{\mathrm{R}} = F_1 - F_3/2$ and $F_{\mathrm{l}} = -F_1 + F_2/(2x)$. To discuss the cross section in terms of these helicity structure functions, let us go back to the matrix element and rewrite it using helicity indices n, m instead of Lorentz indices α, β:

$$\mathcal{M} \;=\; \sqrt{2}\;G_{\mathrm{F}}\;j^{n}(Q^2)\;\frac{d^{1}(\psi)^{m}_{n}}{1+Q^2/M_W^2}\;\langle X|J_m|p,\sigma\rangle\;. \tag{1.55}$$

In this expression, j and J are the leptonic and hadronic currents, respectively, and $d^1(\psi)$ is a spin-1 rotation matrix specifying the relative orientation of the leptonic and hadronic vertex, as illustrated in Figure 1.7. Considering the "rest frame" of the exchanged W boson, the coordinate axis can be taken parallel to the hadron momenta or to the lepton momenta, and the hyperbolic cosine $\cosh\psi$ describes precisely the transformation between the two. Written out, the $d^1(\psi)$ matrix is

$$d^{1}(\psi) \;=\; \begin{pmatrix} \frac{1+\cosh\psi}{2} & \frac{-\sinh\psi}{\sqrt{2}} & \frac{1-\cosh\psi}{2} \\ \frac{-\sinh\psi}{\sqrt{2}} & \cosh\psi & \frac{\sinh\psi}{\sqrt{2}} \\ \frac{1-\cosh\psi}{2} & \frac{\sinh\psi}{\sqrt{2}} & \frac{1+\cosh\psi}{2} \end{pmatrix}\;. \tag{1.56}$$

Figure 1.7: The coordinate systems used in the helicity formalism. In a) the axis is taken to be in the plane defined by the W and hadron momenta. In c) the axis is taken to be in the plane defined by the W and lepton momenta. After a Lorentz boost to the frame where the W is at rest, a) transforms to b) whereas c) transforms to d).

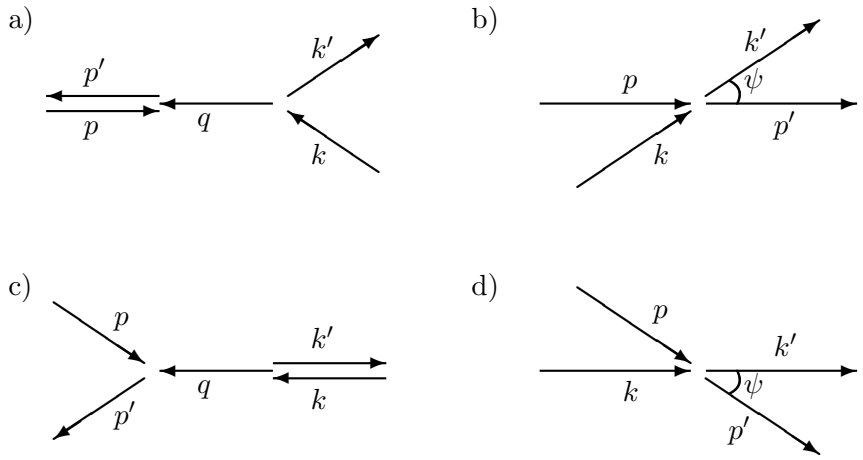

The hyperbolic cosine itself can be obtained from the formulae

$$\cosh\psi = \frac{2\cdot(k+k')}{\Delta(-Q^2,p^2,p'^2)} \tag{1.57}$$

$$= \frac{E_\nu + E_\mu}{\sqrt{Q^2+\nu^2}} = \frac{\eta^2 M^2 - Q^2 + 2\eta(s-M^2)}{\eta^2 M^2 + Q^2} \tag{1.58}$$

$$\stackrel{M\to 0}{\longrightarrow} \frac{2-y}{y}\ , \tag{1.59}$$

where the first equality is general, the remaining relations are given in the laboratory reference frame. The triangle function is

$$\Delta(a,b,c) = \sqrt{a^2+b^2+c^2-2(a\cdot b + a\cdot c + b\cdot c)}. \tag{1.60}$$

In these expressions, η is a generalization of the Bjorken scaling variable x for the case where the target nucleon mass is taken into account. It is

defined through the implicit equation

$$2\ q\cdot p = \frac{Q^2}{\eta} - \eta\ M^2\ . \tag{1.61}$$

To show the correspondence between x and η more clearly, 1.61 can be rewritten as

$$\frac{1}{x}\ =\ \frac{1}{\eta} - \eta\ \frac{M^2}{Q^2}\ . \tag{1.62}$$

It is clear that x and η become identical in the limit $M^2/Q^2 \to 0$. The variable η is sometimes referred to as the Nachtmann variable [35]; it also applies to the inclusive neutrino cross section in the absence of heavy quarks.

In Eq. 1.21, we showed the decomposition of the inclusive cross section for deeply inelastic scattering in terms of the scaling structure functions F_i. A similar derivation gives this cross section in terms of the helicity structure functions:

$$\frac{d\sigma^{\nu(\bar{\nu})}}{dxdy} = \frac{yQ^2}{4\pi(1+Q^2/M_W^2)^2} \left[(1+\cosh^2\psi)\frac{F_{\rm R}+F_{\rm L}}{2} + \sinh^2\psi F_{\rm l} \mp \cosh\psi(F_{\rm R}-F_{\rm L})\right]\ , \tag{1.63}$$

where the plus (minus) sign in the last term refers to the case of neutrinos (antineutrinos).

To understand what we have gained by these transformations, we have to return to the factorization theorem, Equation 1.42. The point to note is that the tensor decomposition of $W^{\alpha\beta}$ and the tensor decomposition of $\hat{\omega}^{\alpha\beta}$ no longer coincide when masses are introduced. The hadronic tensor $W^{\alpha\beta}$ is decomposed in terms of linear combinations of the four-momentum transfer q and the hadronic four-momentum p, whereas the partonic tensor $\hat{\omega}^{\alpha\beta}$ is decomposed in terms of linear combinations of the four-momentum transfer q and the partonic four-momentum $\xi' p$. Neglecting both the nucleon mass and all quark masses involved, there is a direct correspondence between W_i and $\hat{\omega}_i$: the hadronic structure functions are obtained by simple multiplication of $\hat{\omega}_i$ with the parton structure functions, summing over all partons. This situation changes dramatically as masses are introduced since the p and $\xi' p$ will no longer be parallel. Therefore, the W_i will be linear combinations of all $\hat{\omega}_j$, including non-diagonal terms for which $j \neq i$. In general, the partonic four-momentum can be written as $\hat{p}^\mu = \zeta_p p^\mu + \zeta_q q^\mu$. The zero-mass limit is then recovered through the replacements $\zeta_p \to \xi'$ and $\zeta_q \to 0$.

On the other hand, in the helicity formalism, tensors are decomposed with respect to the W boson polarization vectors, introduced in Equations 1.47–1.49. Analogous to the hadron decomposition given in 1.51, we can define parton helicity structure functions

$$\hat{\omega}_{\lambda=\mathrm{L,R,l}} \quad = \quad \epsilon^*_\lambda(\hat{p},q)_\alpha \; \hat{\omega}^\alpha_\beta \; \epsilon_\lambda(\hat{p},q)^\beta \; . \tag{1.64}$$

The simplification of the helicity approach now follows from the fact that the two sets of polarization vectors $\epsilon_\lambda(\hat{p},q)$ and $\epsilon_\lambda(p,q)$, as opposed to the two sets of Lorentz invariants in $\hat{p}$ and p, are identical and remain identical when masses are introduced: the direction of the polarization axis is given by three-momenta, not four-momenta. In the infinite momentum frame, the three-momenta $\hat{p}$ and p are collinear by construction. Thus, the helicity formalism retains the one-to-one correspondence between hadronic and partonic structure functions, even when quark and nucleon masses are introduced.

Furthermore, because of the chiral couplings of electroweak theory, the parton-level helicity amplitudes ω_λ exhibit a simple symmetry and structure. In particular, for the W-exchange process encountered in charged current neutrino scattering, only left-handed chiral couplings are involved. Working out the parton helicity structure functions for this process, we obtain

$$\omega_R \;=\; |V_{12}|^2 \; \frac{Q^2+m_1^2+m_2^2-\Delta(-Q^2,m_1^2,m_2^2)}{\Delta(-Q^2,m_1^2,m_2^2)} \; \delta\left(\frac{\xi}{\chi}-1\right) \; , \tag{1.65}$$

$$\omega_L \;=\; |V_{12}|^2 \; \frac{Q^2+m_1^2+m_2^2+\Delta(-Q^2,m_1^2,m_2^2)}{\Delta(-Q^2,m_1^2,m_2^2)} \; \delta\left(\frac{\xi}{\chi}-1\right) \; , \tag{1.66}$$

$$\omega_{\mathrm{long}} \;=\; |V_{12}|^2 \; \frac{\frac{(m_2^2-m_1^2)^2}{Q^2}+m_1^2+m_2^2}{\Delta(-Q^2,m_1^2,m_2^2)} \; \delta\left(\frac{\xi}{\chi}-1\right) \; , \tag{1.67}$$

where m_1 and m_2 are the masses for the initial state and final state quarks, respectively and V_{12} is the CKM matrix element for the transition between quark flavours 1 and 2. Finally, χ is a further generalization of the Bjorken scaling variable x, now for the inclusion of quark masses. In terms of the previously introduced Nachtmann variable η, it is defined as

$$\chi \;=\; \eta \; \frac{Q^2+m_2^2-m_1^2+\Delta(-Q^2,m_1^2,m_2^2)}{2Q^2} \; . \tag{1.68}$$

Now we have all the necessary components to calculate the charm production cross section. Neglecting the masses of d and s quarks and taking the

sum in Eq. 1.42 the following equations for the helicity structure functions are obtained

$$F_{\mathrm{L}} = g_{\mathrm{La}}^2 2q_{\mathrm{N}}^a(\chi)\ , F_{\mathrm{R}} = 0\ , F_{\mathrm{long}} = g_{\mathrm{La}}^2 \frac{m_{\mathrm{c}}^2}{2Q^2} 2q_{\mathrm{N}}^a(\chi)\ , \tag{1.69}$$

where the sum is over a which can be either d or s quark. It's worth noting that the Callan-Gross relation ($F_{\mathrm{long}} = 0$) is violated if the charm quark mass is taking into account. Substituting the expressions of the structure functions into Eq. 1.63:

$$\frac{d^2\sigma}{dxdy} = G_{\mathrm{F}}^2 \frac{yQ^2}{\pi} \Big(|V_{\mathrm{cd}}|^2 d(\chi) + |V_{\mathrm{cs}}|^2 s(\chi) \Big) \Big[\Big(\frac{1+\cosh\psi}{2} \Big)^2 + \frac{m_{\mathrm{c}}^2}{2Q^2} \frac{\sinh^2\psi}{2} \Big]\ , \tag{1.70}$$

where G_{F} is Fermi constant. To get similar expression for the anti-neutrino nucleon scattering, it is sufficient to replace $d(\chi)$ and $s(\chi)$ by $\bar{d}(\chi)$ and $\bar{s}(\chi)$ respectively.

1.4 Radiative corrections and polarization effects

Radiative corrections due to strong interactions are taken into account by redefinition of the structure functions as described in Section 1.2.2. Radiative corrections due to electromagnetic processes are included explicitely since they affect the kinematical variables. The dominant effect is that the measured momentum of outgoing muon is lower than it is considered in the calculations. Such a smearing is simulated using the formalizm from Ref. [36]. TAUOLA software package [37] takes care of the polarization effects of the outgoing lepton.

1.5 Quasi-elastic charm production

In addition to the deeply inelastic production of charm, there is also a significant contribution of charm produced in quasi-elastic processes (QE). These processes are as follows

$$\nu_\mu n \to \mu^- \Lambda_{\mathrm{c}}^+\ , \tag{1.71}$$

$$\nu_\mu n \to \mu^- \Sigma_{\mathrm{c}}^+ (\Sigma_{\mathrm{c}}^{+*})\ , \tag{1.72}$$

$$\nu_\mu p \to \mu^- \Sigma_{\mathrm{c}}^{++} (\Sigma_{\mathrm{c}}^{++*})\ . \tag{1.73}$$

The key features of the QE interactions are low hadronic energy along with two charged tracks at the primary vertex: one is muon and the other one

is charmed hadron. The cross section for the quasi-elastic charm has been measured by CHORUS collaboration [38] and is found to be

$$\frac{\sigma(\mathrm{QE})}{\sigma(\mathrm{CC})} = [0.23^{+0.12}_{-0.06}(\mathrm{stat})^{+0.02}_{-0.03}(\mathrm{syst})] \times 10^{-2} \ . \tag{1.74}$$

To estimate the quasi-elastic charm production a specific Monte Carlo generator QEGEN [39] has been written. The generator is based on a theoretical model which uses SU(4) symmetry in the matrix elements calculation for different processes. The details of the model are in Ref. [40].

Chapter 2

The CHORUS beam and detector

The CHORUS experiment was designed to search for $\nu_\mu \rightarrow \nu_\tau$ oscillations through the detection of τ produced in charged current interactions. Although the charm physics was not originally foreseen, it became feasible due to fast emulsion scanning systems. This chapter considers the neutrino beam and the parts of the detector that are essential for the charm analysis: the emulsion target, the calorimeter and the muon spectrometer.

2.1 Neutrino beam

High-energy neutrino beams were built for the first time back to 1960s when the existence of muonic neutrino has been discovered at Brookhaven. The neutrinos are produced by the decays of π and K mesons coming from the interaction of a boosted hadron and a nucleus. By installing magnetic lenses on the path of the secondary hadrons it is possible to separate positively charged hadrons from the negative ones and thus enhancing a neutrino beam component against anti-neutrinos and vice versa. It is also possible to give a desired shape to the neutrino beam spectrum.

For the purposes of the CHORUS experiment the West Area Neutrino Facility (WANF) [41] provided a beam of mainly muonic neutrinos in wide spectrum band mode. Schematic representation of the beam-line is shown in Fig. 2.1. Protons from the Proton Synchrotron (PS) are accelerated in Super Proton Synchrotron (SPS) to 450 GeV in a cycle of 14.4 s. After the acceleration protons are extracted in two spills each lasting 6 ms and separated by 2.7 s, and then stopped in a Be target producing mainly pions and kaons of both charges. The magnetic system made of horn and reflector

Figure 2.1: Sketch of WANF beam-line.

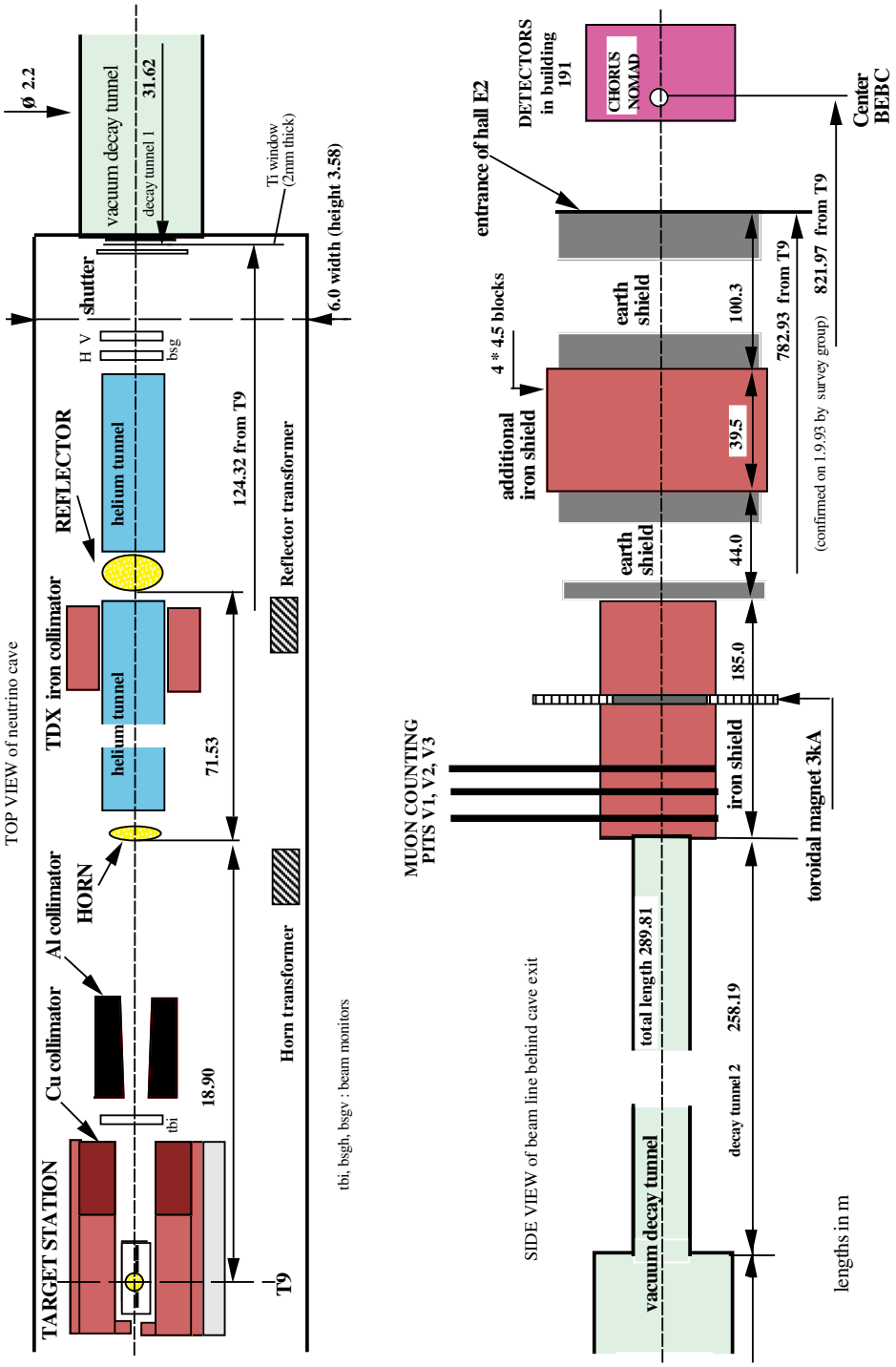

focuses positively charged particles and bends out the negative species. The beam of unstable π^+ and K^+ enters into the 290 m long vacuum tunnel where they decay to muonic neutrino channels with branching ratios of 99.99% and 66.7% respectively :

$$\begin{aligned} \mathrm{BR}(\pi^+ \to \mu^+\nu_\mu) &= 99.99\% \\ \mathrm{BR}(K^+ \to \mu^+\nu_\mu) &= 63.4\% \\ \mathrm{BR}(K^+ \to \pi^0\mu^+\nu_\mu) & \end{aligned} \tag{2.1}$$

The protons, which did not interact in the target, charged leptons or hadrons from the meson decay or surviving π^+ or K^+ are all absorbed in a shielding composed of 225 m of iron and 144 m of earth. The neutrino beam in front of the detector is composed of predominantly ν_μ, with unavoidable 5.6% $\overline{\nu}_\mu$ contamination, 0.7% of ν_e and 0.17% of $\overline{\nu}_e$. Since the experiment was designed to discover neutrino-oscillations any significant source of ν_τ would have dramatic consequences for the analysis. The level of ν_τ from $D_s^+ \to \tau\nu_\tau$ was estimated to be below one detected event over the lifetime of the experiment. Fig. 2.2 shows the simulated beam spectra by GBEAM [42] utility. The average ν_μ energy in the beam was $< E_\nu >$=27 GeV.

2.2 Beam flux measurement

The beam flux has been measured for the purpose of the structure function analysis [43, 44]. Let us briefly review it.

To measure the energy spectra and the integral fluxes charged current neutrino interactions reconstructed in the calorimeter are used. Since the neutrino cross section is approximately proportional to the neutrino energy E_ν, the energy spectrum of neutrino interactions is directly related to the energy weighted beam spectrum. The normalization is chosen such that the energy weighted beam flux corresponds to the rate of interactions on an target of surface density of (1 ton $\cdot$ m^2). The interaction rate is determined from the number of events in bins of different energies $N(E_i)$, corrected for detector acceptance and resolution, and normalized to the bin size ΔE_i, the surface density ρ, and the number of protons on target N_{pot}:

$$\Phi(E) = \frac{N(E_i)}{N_{\mathrm{pot}}\Delta E_i \rho}. \tag{2.2}$$

The resulting beam spectra are shown in Fig. 2.3 together with the results from the GBEAM simulation. In neutrino beam mode, the neutrino

component is typically 15% below the GBEAM values, except around 60 GeV, where they agree with each other. The measured anti-neutrino contamination is also lower than GBEAM, except at very high and very low energy.

The integrated interaction rate and the average interaction energy of the measured beam spectra and of the simulation are summarized in Tables 2.1 and 2.2.

Although the interaction rates are given at the calorimeter they should not be much different at the emulsion target.

2.3 CHORUS detector

The CHORUS detector [45] contains several parts each performing its own task:

Figure 2.2: Simulated flux of the different components of the neutrino beam as a function of the neutrino energy.

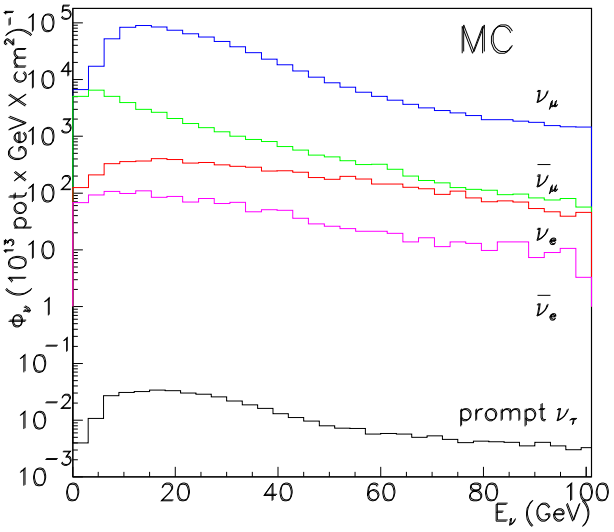

Figure 2.3: Measured and simulated beam spectra in neutrino beam mode.

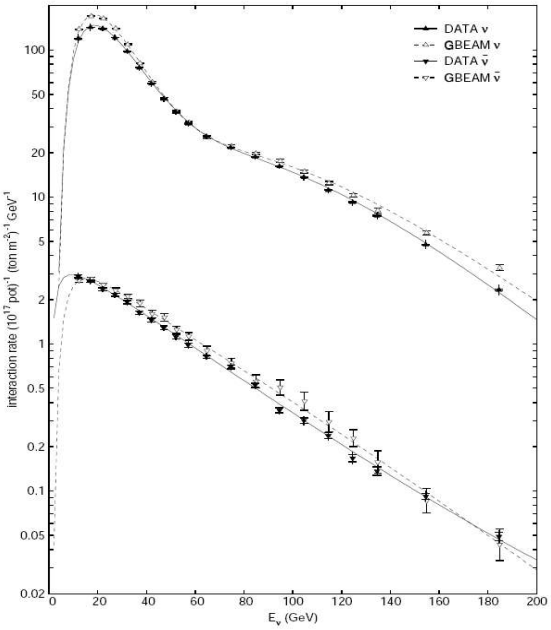

Table 2.1: Interaction rates on a 180×180 cm^2 surface at the calorimeter for neutrinos between 10 and 200 GeV. The units are $(10^{16}\mathrm{N_{pot}})^{-1}(\mathrm{ton}\cdot\mathrm{m}^{-2})^{-1}\mathrm{GeV}^{-1}$. The first error is statistical and the second is systematic. The difference between the data and the simulation can be attributed by a simulation of the focusing power that is not as strong in reality as is simulated in GBEAM.

	Data	GBEAM
ν_μ	580.1 ± 0.6 ± 17.5	645.9 ± 2.0
$\bar{\nu}_\mu$	12.9 ± 0.1 ± 0.4	14.1 ± 0.2

Table 2.2: Average neutrino energies in units of GeV on a 180×180 cm^2 square surface at the calorimeter for neutrinos between 10 and 200 GeV. The first error is statistical and the second is systematic.

	Data	GBEAM
ν_μ	47.07 ± 0.04 ± 0.84	46.83 ± 0.16
$\bar{\nu}_\mu$	48.87 ± 0.25 ± 0.74	50.20 ± 0.70

- Emulsion target. Emulsion serves not only as a target to the neutrino beam but also allows to make a detailed investigation of the events. It is possible due to the outstanding spatial resolution of the emulsion.
- Hexagonal magnet. The magnet is used as a hadron spectrometer.
- High resolution calorimeter. The calorimeter measures the energy and the direction of electromagnetic and hadronic showers.
- Muon spectrometer. This installation measures the momentum of hard muons and their charge.
- Trigger system. Using logical combinations of the signals coming from different trigger planes, the trigger system selects specific types of events: charged current or neutral current interactions. It also rejects events not related to the neutrino-induced processes.

The detector overview is schematically shown in Fig. 2.4.

2.3.1 Target area

The target area contains four emulsion modules followed by scintillating fibre trackers as shown in Fig. 2.5. Each emulsion module is made of two rows of four sub-modules with a size of 0.36 × 0.76 m^2 put into a metallic frame. Every sub-module has successive 36 *bulk sheets*, a *special sheet* (SS) placed just immediately after the most downstream bulk sheet and a *changeable sheet* (CS) located 38 mm further downstream to separate the tracks. A bulk sheet has a 90 μm plastic transparent base and is covered with 350 μm of nuclear emulsion on each side. In total, 206 litres of emulsion weighting 770 kg were used. Bulk sheets serve as a neutrino target and after development allow to manually scan interesting events. Bulk emulsion has been exposed for two years in the beam while it was typically several months for the CS

Figure 2.4: CHORUS detector overview.

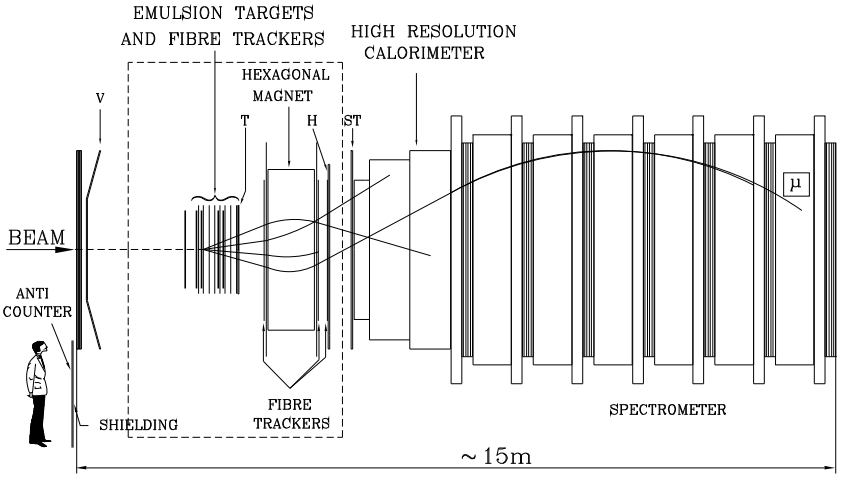

or SS interface sheets. The special sheets and the changeable sheets are used to align the tracks in emulsion with tracks reconstructed in further downstream electronic detectors. For this purpose, an emulsion module has been followed by a scintillating fibre tracker system [46, 47]. To reduce extrapolation errors and to avoid ambiguities in the tracks reconstruction, the tracker system must offer good two-track separation such that a track can be located in emulsion.

Fibre trackers follow the pattern of the emulsion sub-modules and consists of eight modules interleaved between the four emulsion stacks. Every module consists of four planes, measuring the two transverse coordinates Y,Z and two orthogonal stereo projections $Y^{\pm}$,$Z^{\pm}$ rotated by $\pm 8^{\circ}$ with respect to Y and Z. A tracker plane consists of seven layers of scintillating fibres 500 μm diameter each. The far ends of fibres are covered with aluminium to act as a mirror while the other is attached to an opto-electronic chain with a CCD camera. There are about one million fibres connected to 58 opto-electronic chains. Corrected for intrinsic angular resolution in the emulsion scanning, the achieved precisions are $\sim$ 150 μm in position and $\sim$

Figure 2.5: Overview of the emulsion target area. The emulsion modules are placed along the X-axis and each of them is followed by a scintillating fibre tracker system.

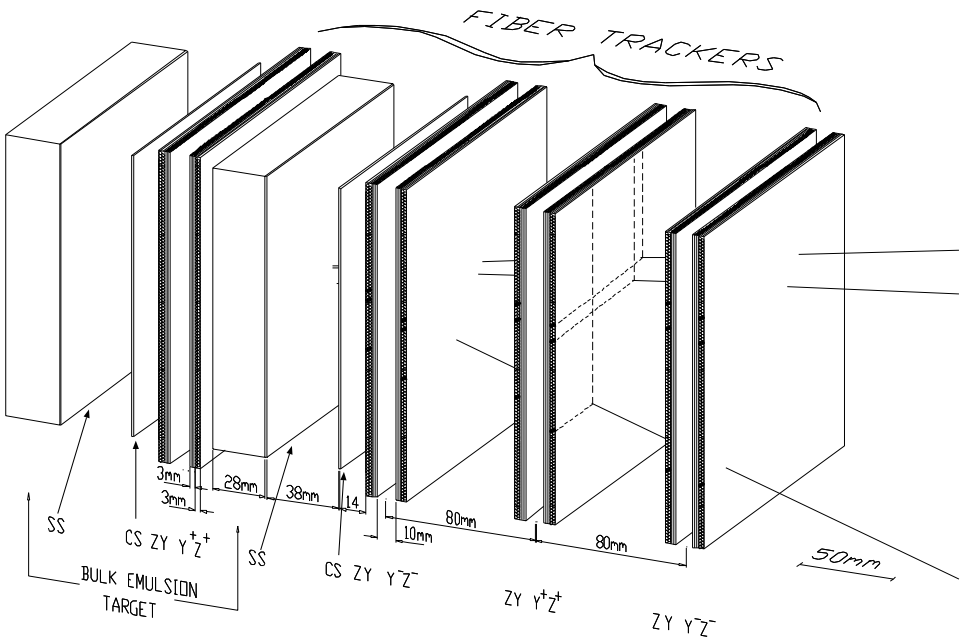

2 mrad in slope.

2.3.2 Hexagonal magnet spectrometer

An air-core magnet[48] with hexagonal shape is placed between the target region and the calorimeter for the measurement of the charge and momentum of the particles (mainly hadrons and slow muons) coming from the target area. A field of 0.12 Tesla is produced such that its value does not change much with radial distance.

The measurement of particles momentum uses a fit to curvature of track trajectory. Track slope and position are measured in front of the magnet and right behind it by another system of scintillating fibre trackers. Severe geometrical design constraints limit the resolution of the hexagonal magnet spectrometer.

The momentum resolution $\frac{\Delta p}{p}$ is the quadratic sum of two terms: a

Figure 2.6: The muon momentum resolution for the hexagonal magnet spectrometer. The solid lines show the result of the fit by convoluting the two known spectrometer resolution: below and above 6 GeV.

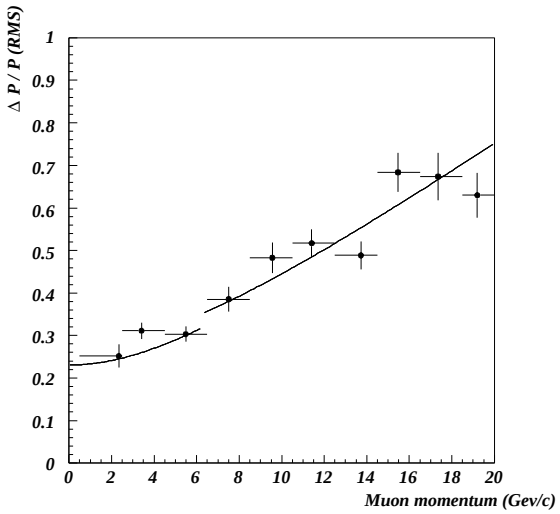

constant term from multiple scattering within the magnet

$$\frac{\Delta p}{p_{scat}} = 22\%, \tag{2.3}$$

and a term which reflects the measurement accuracy and is proportional to momentum

$$\frac{\Delta p}{p_{meas}} = 3.5\% \times p/\mathrm{GeV}. \tag{2.4}$$

The momentum measurement resolution of the spectrometer was obtained comparing muon momentum reconstructed by the muon spectrometer and hexagonal hadronic spectrometer. This resolution is presented in Fig. 2.6.

2.3.3 High resolution calorimeter

Reconstruction of the kinematical variables in the electronic detectors is of great importance starting from the selection of events to be scanned to the selection for each particular analysis. It implies that the hadronic shower should be measured with good energy and angular resolution. The calorimeter also has a capability to measure track information to link tracks in the Target Tracker and the muon spectrometer.

These requirements are fulfilled by a spaghetti calorimeter with scintillating fibres embedded into a lead matrix and interleaved with a set of streamer tubes. Each fibre has 1 mm in diameter. The lead to scintillator volume ratio is 4:1 which assures both compensation and good sampling, and consequently good hadronic energy resolution. The fibres are placed perpendicular to the beam direction to provide good angular resolution for showers and the tracking of muons of any origin.

The CHORUS calorimeter has a modular structure and consists of three sections with decreasing granularity : electro-magnetic calorimeter (EM), hadronic calorimeters HAD1 and HAD2. A sketch of the calorimeter is shown in Fig. 2.7. EM and HAD1 are made of scintillating fibres and lead while HAD2 lead layers are interleaved with scintillating strips. The tracking capability of charged particles is improved by 22 streamer tube planes.

The total calorimeter thickness is 144 radiation lengths or 5.2 interaction lengths. Such thickness is sufficient to contain 99% of showers produced by a 5 GeV/c pion. About 90% of hadrons produced in neutrino interactions have momentum less than 5 GeV/c which makes leakage to the muon spectrometer small enough for interactions in the emulsion.

The calibration of the calorimeter was made with test beams of well-defined energy. First, the calorimeter response was studied using an electron test beam in the range 2.5 to 10 GeV/c. The energy resolution is well fitted by the function

$$\frac{\sigma(E)}{E} = \frac{(13.8 \pm 0.9)\%}{\sqrt{E(\mathrm{GeV})}} + (-0.2 \pm 0.4)\%. \tag{2.5}$$

By studying electron showers in different calorimeter zones, the nonuniformity was estimated to be of the order of 5%. A similar test has been performed with pion beams with an energy range from 3 to 20 GeV/c. From Gaussian fit to the response distributions the energy resolution for pions was estimated to be

$$\frac{\sigma(E)}{E} = \frac{(32.3 \pm 2.4)\%}{\sqrt{E(\mathrm{GeV})}} + (1.4 \pm 0.7)\%. \tag{2.6}$$

Figure 2.7: Schematic overview of the calorimeter with the three sections.

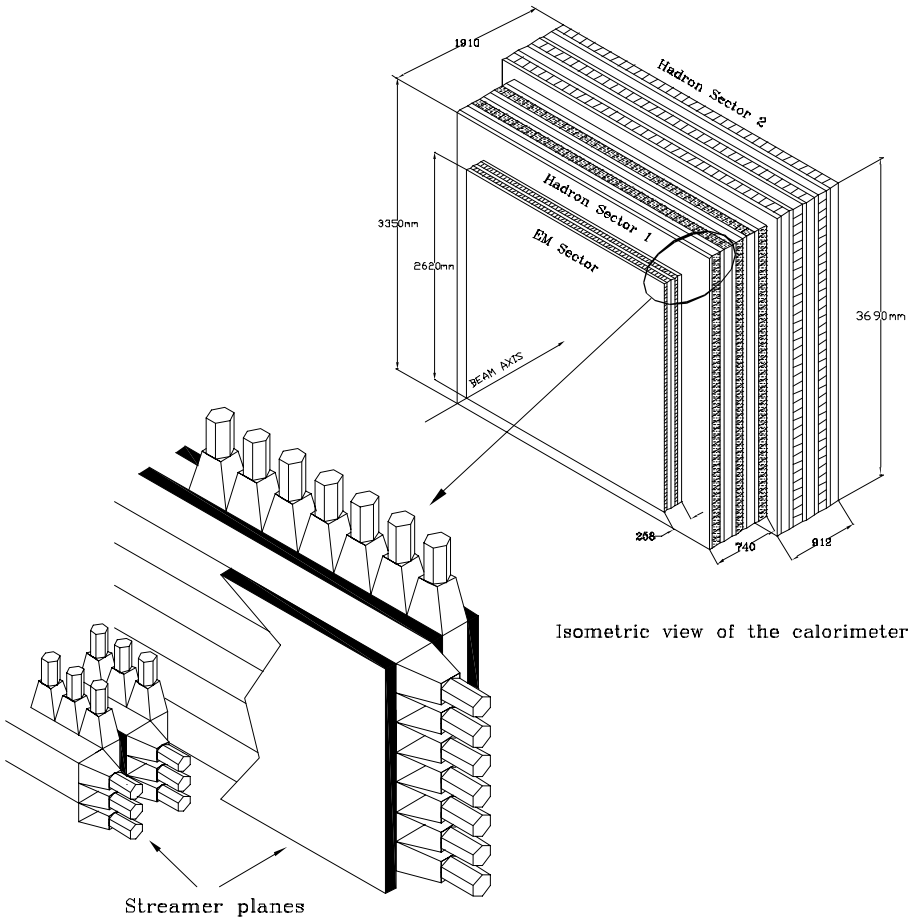

The energy resolution for hadrons and electro-magnetic components is presented in Fig. 2.8.

Figure 2.8: Energy resolution of the calorimeter. Left side: electromagnetic component, right side: the hadronic part of the shower.

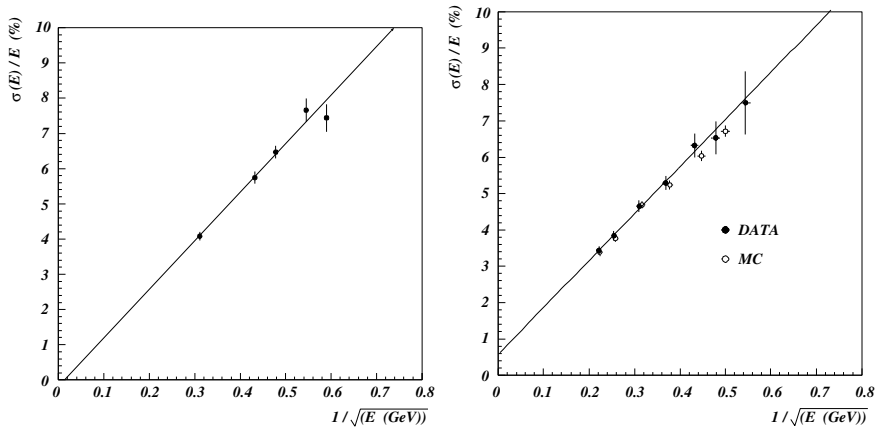

2.3.4 The muon spectrometer

The spectrometer is located further downstream the calorimeter. The calorimeter absorbs nearly all particles except muons because they are less affected by the media as they propagate through it. As shown in Fig. 2.9, the spectrometer is constructed from six magnetized toroidal modules and tracking detectors consisting of drift chambers and streamer tubes previously used in the upgraded CDHS detector [49, 50] and later in the CHARM II electronic detector [51, 52, 53, 54]. In addition, scintillator planes interleaved with the magnet iron provide a measurement of the leakage of hadronic showers from the back of the calorimeter. The fast signals from these scintillator planes are also used for triggering.

The momentum of a muon is determined from the bending of its trajectory in the six toroidal magnets. If a low momentum muon stops in the spectrometer its momentum is also estimated from the range measurement. Each magnet is constructed from twenty 2.5 cm thick iron disks with an outer diameter of 375 cm, interleaved with 0.5 cm thick scintillator planes put into the 0.6 cm gaps between the disks. Each magnet weights about 43 tons.

Figure 2.9: The muon spectrometer overview (top) and its details (bottom).

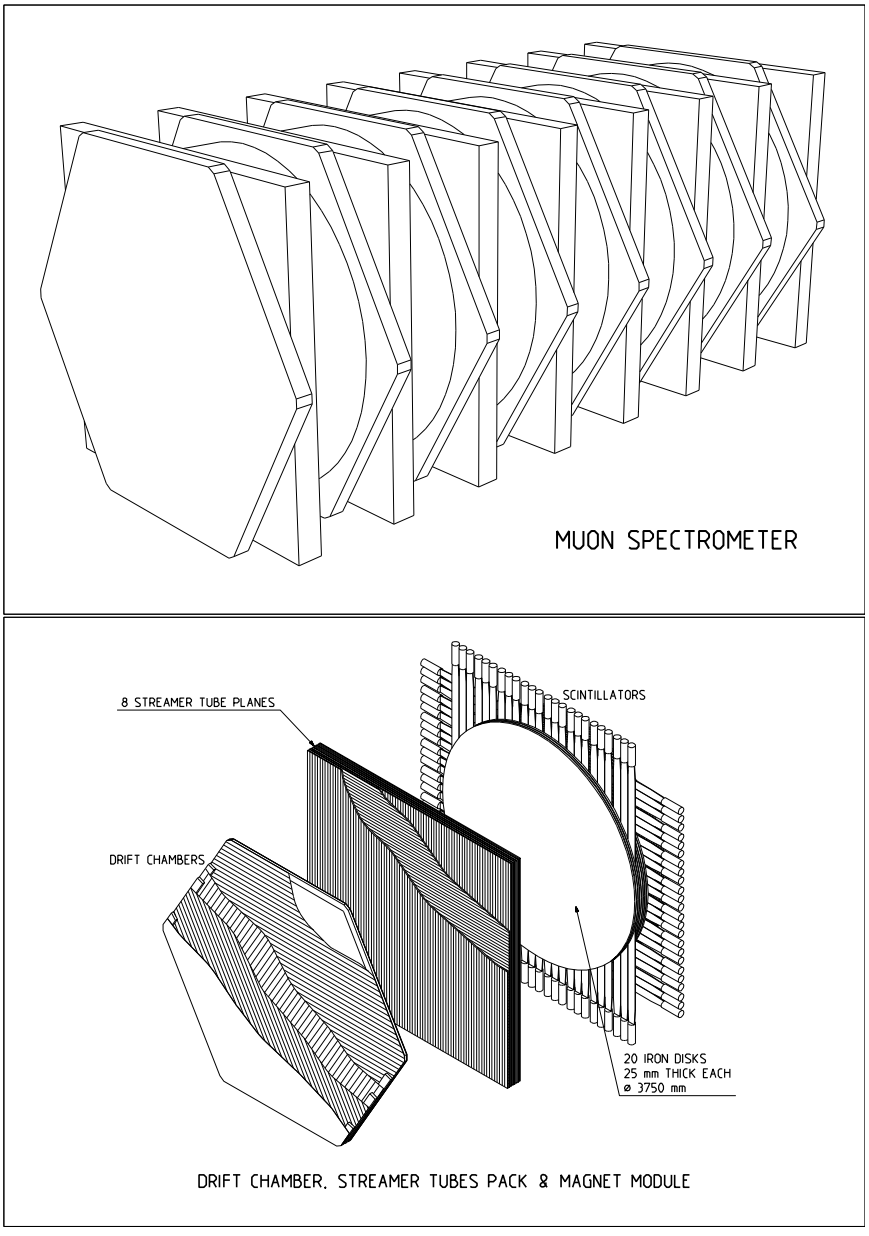

The iron is magnetized by four water-cooled copper coils passing through a 8.5 cm wide hole in the centre of each magnet. The field in iron is nearly symmetric in azimuthal angle and varies by 25% along the radius. To maximize the acceptance for τ^- decays, the polarity of the current is set such that negatively charged muons are bent towards the centre of the magnets.

The calibration of the end-system was performed using 75 GeV/c test beam muons. The momentum resolution has been evaluated with a detailed simulation and is presented in Fig. 2.10.

Figure 2.10: The momentum resolution, determined from a Gaussian fit to 1/P distribution using a test beam with both signes muons and a simulation. The measured resolution (13-15%) is reasonably well reproduced by the Monte Carlo. Somewhat inferior resolution for the test beam at 12 GeV/c can be attributed to the dispersion of the beam momentum. At the lowest momentum (12 GeV/c), which was at the limit (or even slightly beyond) of the beam line capabilities, the maximum was shifted in vertical plane by about 3 mrad from the beam core and differed from the "nominal" value by as much as 1 GeV/c. Moreover, at 12 GeV/c the variation of the average momentum with the angle within the narrow angular window was signicant (about 10%) which contributed to the measurement of the momentum resolution.

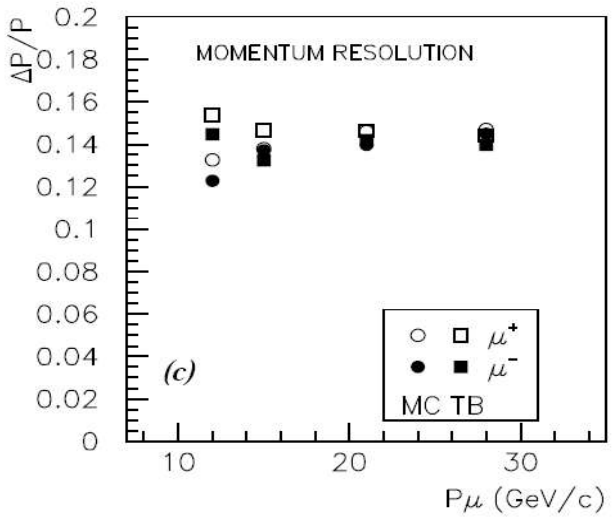

Table 2.3: Geometrical characteristics of the trigger hodoscopes. The units for strip width and strip length are cm while the covered area is in cm^2.

	E	T	H	V	A
# strips/plane	7	15	20	20	16
Strip width	20	10	10	20	20
Strip length	148	160	200	320	200
Area covered	150×148	160×160	200×200	400×320	200×320

2.3.5 The trigger system

The CHORUS trigger system was designed primarily to select neutrino interactions in the emulsion target region and in synchronizing the data acquisition with the beam spills. The main difficulties arise from the need to form a "strobe" with no incoming charged particle and from the limitation that CCD opto-electronic can handle only 2 events per neutrino spill. On the other hand, the trigger system should be flexible enough to select neutrino events in the calorimeter and, possibly, in the spectrometer. In total, only about seven events per spill are selected for detailed investigation. In the 14.4 s cycle of the SPS accelerator there are two 6 ms neutrino spills, separated by 2.7 s.

The trigger system consists of several scintillator planes (trigger-hodoscopes) E(mulsion), T(iming), H(odoscope), V(eto) and A(nti-counter) as displayed in Fig. 2.11. The geometrical characteristics of the planes are summarized in Table 2.3. Logical combinations of the hodoscopes are used to select neutrino interactions and to reject the background coming from cosmic rays, beam charged remnants and neutrino interaction outside the target. A neutrino trigger in the target region is defined as a hit coincidence in E, T planes and H consistent with a particle slope $|\tan\theta| < 0.25$ with respect to the neutrino beam. A veto is formed by any combination of a counter hit in the veto hodoscopes (V and A) and a hit in T, with a precise timing of 2 ns at FWHM to avoid vetoes due to backscattering.

The observed rate of neutrino interactions is 0.5 events per 10^{13} protons on the SPS target corresponding to an effective neutrino target mass of 1600kg. About one half of these events originate in the emulsion target. The cosmic background is very small, about one $T \times H \times \bar{V}$ per 100 ms. Owing to the high redundancy of the trigger system and to the simplicity of the requirements, a trigger efficiency of 99% was simulated for ν_μ charged current interaction and is more than 90% for neutral current events.

Figure 2.11: Overview of the trigger system hodoscopes.

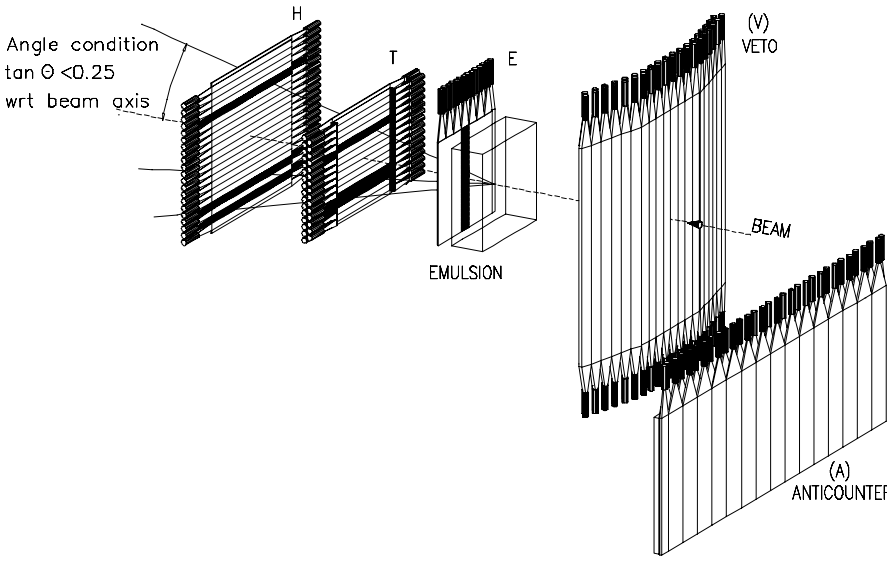

Chapter 3

Event reconstruction in the emulsion

At present time emulsion experiments have outstanding angular and space resolutions in terms of tracking. However, the price has always been the huge emulsion scanning load, which translates into high expense of time and manpower. As an example, analyzing the CHORUS emulsion manually would take hundreds of man-years. Thanks to the latest achievements in automatic emulsion scanning, CHORUS has collected about one hundred thousand charged-current neutrino interactions which contain a subsample of two thousand charm events. It is worth stressing that the quality of the collected data is very different with respect to the other neutrino dimuon experiments. In these experiments events with two hard muons are studied: one muon comes from the neutrino interaction vertex and the other one is from charm decay. The advantage of such experiments is high statistics. However, the main disadvantage is low spatial resolution which the reason of significant level of the background in dimuon data. The background events are mainly muonic decays of strange particles or pions. In CHORUS every charm event is verified by manual confirmation and the background is very low (<5%) if compared to usual dimuon data (up to 30%).

The event reconstruction in the emulsions, the so-called Netscan technique, was developed in Nagoya University originally for the DONUT experiment at Fermilab. The main feature of Netscan is that all track segments within a fixed volume centred on the vertex position are picked up. The automatic scanning technique, developed by CHORUS for the oscillation search, is based on an extremely fast automatic follow back in the emulsions of a long track reconstructed by the electronic detectors. Such a track

is called *scanback* track. In the oscillation search, the scanback track is a candidate for being a decay product of the τ, and it is traced back to the neutrino interaction vertex. Then, further measurements are made to search for the presence of a τ decay vertex.

The Netscan technique extends the automatic scan to a full inspection of the emulsion volume surrounding the interaction vertex. The events which are analyzed are those for which a neutrino interaction vertex has been located using the scanback track technique. A surface of 1.5×1.5 mm^2 is automatically scanned on eight consecutive planes: the plate immediately upstream from the vertex plate, the vertex plate itself and the six plates downstream. All the tracks found in the volume are written to a data file for further analysis. Then, by software, the reconstruction of the full event topology can be performed. In four years of data taking CHORUS has collected about 30 times the statistics of the previous similar experiment E531 [15, 16]($\sim$ 4000 charged and neutral current interactions of ν_μ and $\overline{\nu}_\mu$), by increasing both the target mass (770 kg of emulsion) and the integrated neutrino flux. Given the complexity of the automatic scanning technique, its overall efficiency is definitely lower than that of the manual scanning performed by E531. In this chapter, the main features of Netscan are described as well as the event location and selection efficiencies.

3.1 Event simulation in the emulsion

Neutrino charge current interactions for a beam simulated by GBEAM [42] utility are simulated by deep inelastic scattering event generator JETTA [55]. The JETTA generator is derived from JETSET [56] combined with LEPTO 6.1 [57]. The JETTA generator is devoted to the deep inelastic regime with a cut of 2 GeV^2 for mass of the recoiling hadronic system W^2. The quasi-elastic events are generated by RESQUE [58] generator. Apart from the QE event, RESQUE generates production of baryonic resonances.

The response of the eletronic detectors is simulated by EFICASS utility which is based on GEANT [59] software package. At this stage of the simulation the Monte Carlo is processed through the same event reconstruction program as the real data. The reconstruction program is based on a software package called CHANT. CHANT recosntructs tracks, vertices and performs particle identification. Finally, the response of the emulsion is simulated as explained below.

A complete simulation of emulsion and its scanning is a very challenging task. There are many effects that have to be taken into account: distortion, fog from grains, response of microscope mechanics, optics, chemical devel-

Figure 3.1: Production of τ lepton in ν_τ charged current interactions and its muonic decayas an example. The τ decay vertex is found requiring an angle between τ and μ tracks.

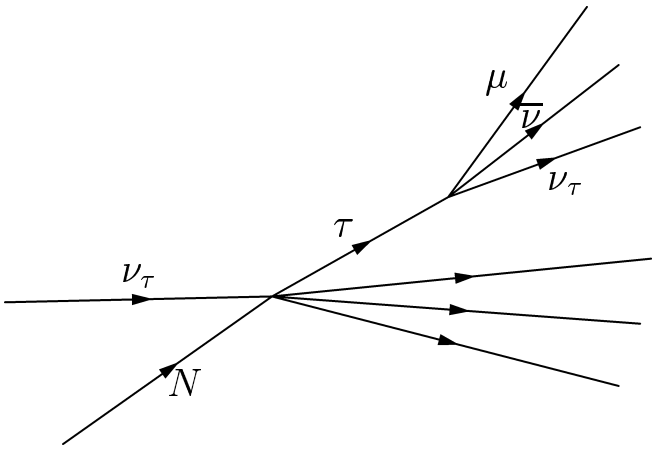

opment of the emulsion and reconstruction software. Fortunately, the full emulsion simulation can be avoided by using real data. Fiducial volumes with no found scanback track (muon) provide the most realistic conditions. However, in some cases the scanback tracks has not been found basically due to inefficiencies. Obviously, the ideal "empty" boxes would be fiducial volumes arbitrary taken in the emulsion. This has not been done in the experiment because the priority is given to the scanning of real data. Finally, an event is simulated by merging simulated tracks into such an empty acquisition set. After this procedure the event is processed through exactly the same reconstruction software as the real data. Let briefly review the complete chain of the simulation.

3.2 Event location in emulsion

CHORUS has finished data acquisition and analysis searching for $\nu_\mu \rightarrow \nu_\tau$ oscillations without finding any evidence. The searched signal was represented by the observation of the decay of the τ produced in a ν_τ interaction. The characteristic topology of the τ decay with one charged daughter is a kink, i.e. a change of the track direction that indicates the decay point (see Figure 3.1).

The emulsion scanning was based on the selection of a track candidate which was followed up to bulk emulsion until the vertex plate which is characterized by the disappearance of the track. This fully automated procedure is called scanback track location and is performed by a hardware video image processor interfaced to a microscope through a CCD camera, the Track Selector.

The CHORUS sample is divided in two sets, according to the two decay modes that were used for the τ search: events containing a negative muon (1μ) and events without muon (0μ). In the 1μ sample, the negative muon was selected as a scanback track, while in the 0μ case, one or more negative hadrons were used. The scanback was then performed on events reconstructed by the fiber tracker with the vertex predicted in the bulk emulsion. The 1μ sample contains many charmed hadrons produced in the charged current interactions which is a background for the τ decays search on one hand and allows to study charm production on the other hand.

This work concerns charm production in neutrino charged-current interactions, thus we focus on events with a muon: a 1μ event is then sent to the scanback if the angle that the muon forms with the beam direction is less than 400 mrad. The angular cut has been introduced due to the limited efficiency of the Track Selector at higher angles.

The location of the primary vertex is a very complex procedure. The automatic search of a track in the target emulsion has to be limited to very small areas ($\sim$ 1 mm^2) and to a small angular range (a few mrad) because of the presence of huge amount of background tracks in the emulsion. This is essentially due to the fact that the exposure of the emulsions was 2 years and hence all particles traversing the emulsion in that period are recorded. A muon reconstructed in the muon spectrometer is extrapolated to the changeable sheet, using the slopes measured by the scintillating fiber trackers that were right downstream of emulsion. Then if the track is found in the changeable sheet, the parameters are measured with higher precision and the track is searched for in the special sheet. Again, if it is found, the track is followed up to bulk, plate by plate (only the most upstream 100 μm are scanned) until it is not found in two consecutive plates: this determines the primary vertex plate.

The event location has several sources of inefficiencies due to distortion of the emulsion, dirt, bad alignment, attachment of the scanback track to a background track, etc. Depending on event, the sources may correlate with each other which makes the simulation of each source of inefficciency difficult to reproduce. Instead, the simulation of all effects taken together is made as a parametrization. During the simulation the location efficiency

has been parametrized as a function of the muon momentum and the slope. The muon momentum distribution is different for the two samples of charged current events, containing or not charm. The dependence of the ratio of the location efficiencies as a function of visible energy is not strong, and the average value of the ratio is

$$\frac{\varepsilon_{\rm loc}^{\rm charm}}{\varepsilon_{\rm loc}^{\rm cc}} = 0.92 \pm 0.02 \ . \tag{3.1}$$

Table 3.1 contains the value of the ratio per different visible energy bins.

During the 1996-1997 exposure period the CHORUS collaboration has collected and reconstructed in the emulsion 93807 1μ and 18178 0μ events.

Table 3.1: The Netscan location efficiencies for charged-current and charm events as obtained with simulation. The units of the energy bins are GeV.

	$E_{\rm vis} < 30$	$30 \leq E_{\rm vis} < 50$	$50 \leq E_{\rm vis}$	Average
$\varepsilon_{\rm loc}^{\rm cc}$	0.65±0.01	0.69±0.01	0.63±0.01	0.65±0.01
$\varepsilon_{\rm loc}^{\rm charm}$	0.60±0.01	0.64±0.01	0.57±0.01	0.60±0.01
$\varepsilon_{\rm loc}^{\rm charm}/\varepsilon_{\rm loc}^{\rm cc}$	0.92±0.02	0.93±0.02	0.91±0.02	0.92±0.02

3.3 Netscan technique

3.3.1 Data acquisition

The basic idea of the automatic emulsion scanning is to transform the three-dimensional information contained in the emulsion volume, into many tomographic images (given by the interplay of a microscope and a CCD camera) taken at different focal depths.

The automatic scanning in CHORUS is performed by a computer controlled microscope of 3 μm depth of field, whose view is sent to the Track Selector[60], a hardware video image processor composed of a Fast Programmable Gate Array, a Fast Memory and a grabber board connected to a CCD camera of 512×512 pixels at 120 Hz frame rate. The actual view corresponds to 150×150 μm^2 and is determined by the microscope optics. The system is described schematically in Fig. 3.2 and 3.3.

In the scanback data taking, the most upstream 50 μm (which corresponds to approximately 100 μm of not swelled emulsion) of the plate are

Figure 3.2: Schematic view of the components of the automatic scanning system at CERN [61].

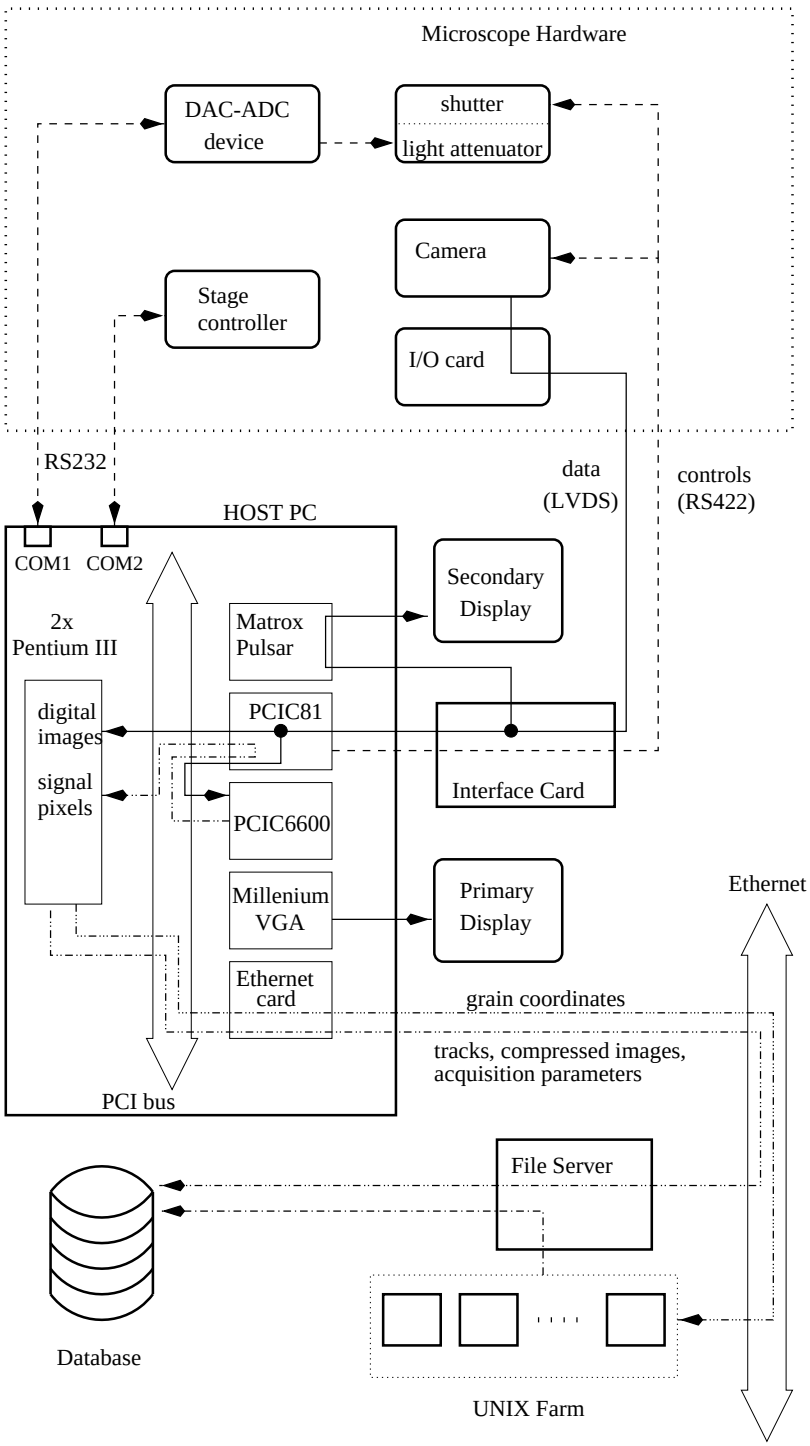

Figure 3.3: An overview of the automatic scanning systems at Nagoya [62, 60, 63].

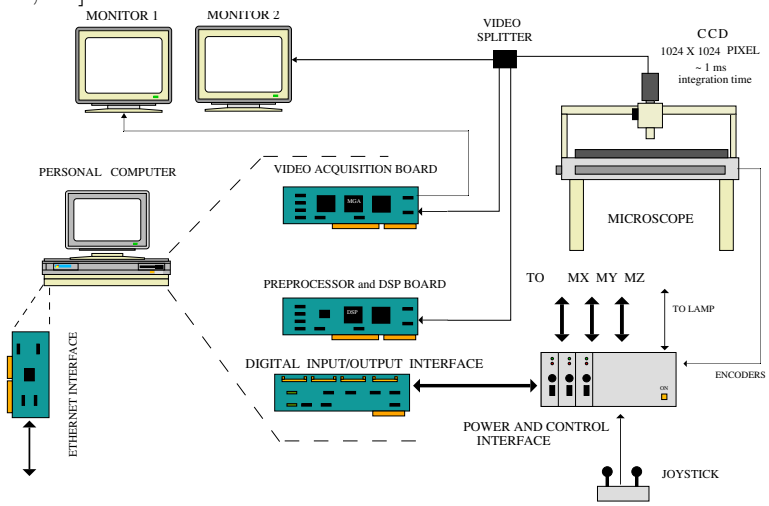

subdivided in 16 slices, which correspond to different depths of field of the microscope. Correspondingly, 16 tomographic images are taken in the most upstream 3 μm of each slice and digitized, then shifted horizontally with respect to the first layer, according to the angle predicted by the special sheet. The track is identified as a peak in the pulse height: this can range from 1 to 16, since each frame can give 1 if a track segment over the fixed greyscale threshold is found therein, or 0 otherwise. An example is shown in Fig. 3.4.

A threshold at a pulse height of 12 is set to accept a track: this on one hand introduces an inefficiency mostly for large angle tracks, but also rejects random coincidences. Table 3.2 shows the TrackSelector efficiency for various angle ranges when the pulse height threshold is set. The efficiencies were measured considering three consecutive plates, with no track segment found in the middle one and a signal in the outer ones, and checking manually if the segment missed by the TrackSelector was actually present. This was repeated for different sets of tracks according to their angle with respect to the neutrino beam.

There are two main reasons why the tracking efficiency decreases with increasing track angle. The first is the shift of the sixteen emulsion slices that the TrackSelector performs to identify the track, according to its predicted angle: in the extreme case of 0 angle, there is no shift at all, so that no mistake can occur. In intermediate situations, the bigger is the track angle,

Figure 3.4: The main steps in image processing by the Track Selector. The images are shifted in the focal plane according to the track slope and then they are summed up to form a pulse-height.

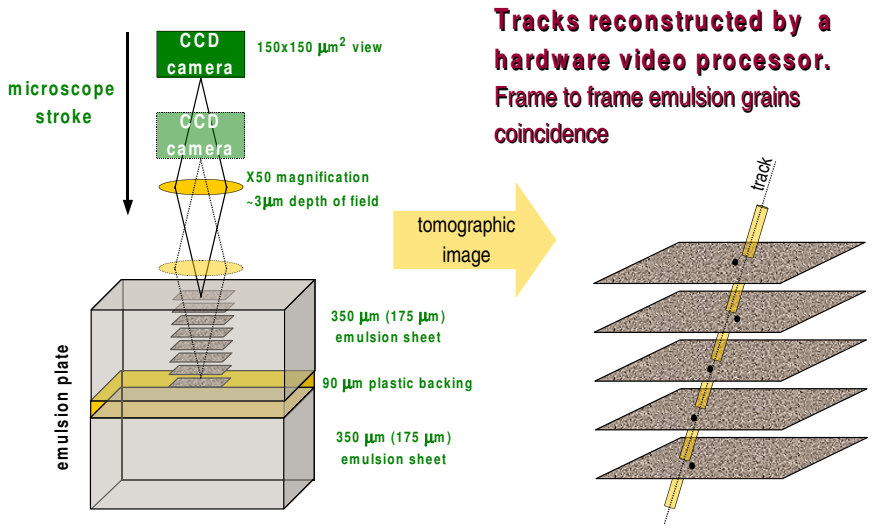

Table 3.2: Track Selector efficiency as a function of the track slope.

Angle range, mrad	Efficiency,%
0 - 50	99.7±0.1
50 - 150	98.6±0.2
150 - 250	90.8±0.4
250 - 350	85.6±0.6
350 - 450	62.9±0.9

the larger is the absolute error on the TrackSelector shift. The second reason is that such tracks go away from the fiducial volume.

The last generation of TrackSelector, the UTS, performs the analysis at 1 cm^2/hour. Such high processing speed allows to handle huge emulsion data similar to the emulsion data of CHORUS.

As mentioned, the events located with the scanback method are inherited by Netscan and used as a prediction of the vertex position. The Netscan data acquisition is performed by the same instrument as for scanback, but a much larger area is scanned, with a large angular acceptance, and no angular prediction from electronic detectors.

A fiducial volume of 1.5 mm ×1.5 mm ×6.32 mm is considered. The longitudinal dimension corresponds to 8 plates: the vertex plate, 1 plate upstream and 6 plates downstream are scanned. The volume is optimized to search for secondary vertices of τ or charm, which both have an average decay length of about 1 mm. The fiducial volume is shown in Fig. 3.5.

As for the scanback, sixteen tomographic images are taken in the most upstream 100 μm of each plate at different focal depths. The threshold on pulse height to retain a track segment is set to 10. All track segments, within the angular acceptance, in the fiducial volume are measured and stored. The angular acceptance is set to -400 mrad $< \theta_{y,z} <$ 400 mrad, where θ_y and θ_z are the angles between the track and the beam axis (conventionally chosen as x) in the (x, y) and (x, z) planes. This is because of the decrease of efficiency of the UTS at larger angles. With the last version of the UTS, the netscanning of one event takes about 10 minutes.

3.3.2 Offline reconstruction

The raw track segments undergo several operations, whose final aim is to reconstruct tracks and vertices of the event. The offline reconstruction then

Figure 3.5: The fiducial volume for the Netscan data taking. The hatched area represents the transparent plastic base of the emulsion plate. The black thick parts of the tracks show the Netscan reconstructed segments.

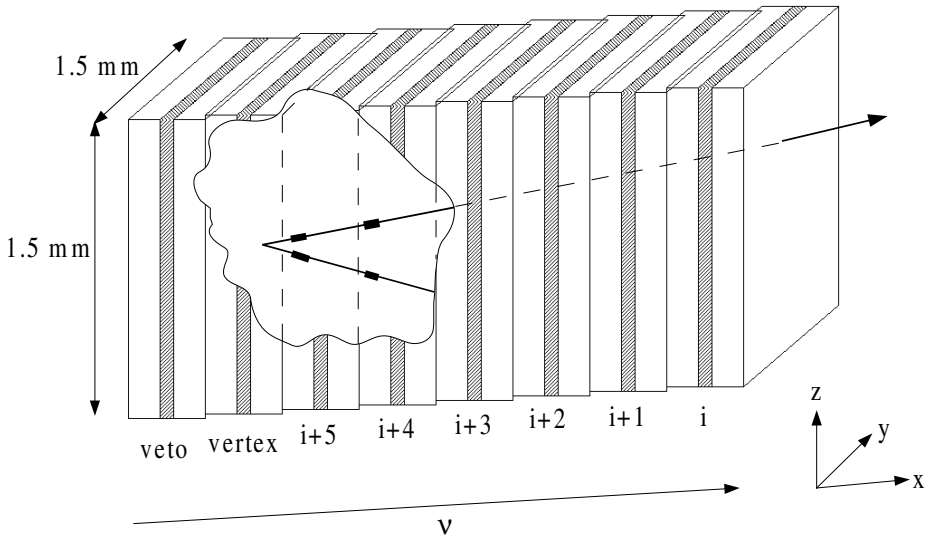

consists in alignment, tracking and vertex finding. Since much of the digital information is in fact not associated to the event, also a heavy work of background rejection must be performed. The reconstruction program is written in C++ and is divided in two block: ECFSAL (Emulsion Chamber First Structure ALignment) which performs first alignment and tracking, and ECVTXA (Emulsion Chamber VerTeX Analysis) for background track rejection, *fine* alignment and vertex reconstruction.

Alignment and tracking

Once the reliable track segments are selected on the basis of the pulse height cut off, "ghosts" must be rejected, i.e. copies of segments which are seen twice because they fell in the intersection zone of two microscope views. Then, if two segments having the same angle are found, the distances to the original track are compared. If the distance for one of them is greater than

5 μm, then it is rejected.

After the segment selection, the recursive alignment-tracking program (ECFSAL) is run. It compares the pattern of segments in two neighbour plates to determine the position and rotation parameters of the plate to plate alignment.

The tracking consists in the extrapolation of the segments of the first plate to the following one, looking for a matching segment in a cone of angle dependent on the alignment residuals (20 mrad being the maximum angle), and in about 4 μm in position, corresponding to 3σ of alignment resolution. If no candidate is found, the starting segment is kept anyway, and the matching is tried in the further upstream plate. This means that gaps are allowed in the Netscan tracks which improves the track reconstruction efficiency.

Rejection of low momentum tracks and fine alignment

At the end of the first alignment-tracking process, on average 5,000 tracks are reconstructed in the fiducial volume but only a few of them are real event tracks. The large part are low momentum tracks coming from cosmic rays, radioactivity, low energy interactions of neutrals, accumulated during the years of emulsion exposure. It is then mandatory to eliminate as more background as possible, and then a second, fine alignment is performed once the event has been cleaned. This is done within the fine alignment-verticing program (ECVTXA).

Tracks are obtained by the connection of several track segments, and the number of reconstructed tracks depends on the angular acceptance in the extrapolation from a segment to the following plate: the larger is the acceptance, the easier a segment will fall inside the solid angle. At the moment, in ECFSAL the tolerance is a floating value which depends on the plate alignment residuals: this means that low momentum tracks, that undergo large scattering, can appear splitted in track segments. Of course it would be easy to make them connected increasing the acceptance, but this can be risky because one could also attach event tracks to background tracks. It is then necessary to find a good balance between the level of misconnection introduced and the number of reconnected low momentum tracks. It was found [62] that the optimal minimal momentum is 100 MeV/c.

After low momentum track rejection, a second, fine alignment is performed using informations from the surviving tracks, similar in procedure to the first level one. After the second alignment, the resolution is 0.5 μm in position and 2 mrad in angle.

3.3.3 Vertex reconstruction

Before reconstructing the vertex, one must eliminate those tracks that seem to belong to the event only because they happen to pass through the fiducial volume, but do not originate therein. These are mainly particles produced in other neutrino interactions and their decay daughters.

A track is defined to be a *stopping track* if it escapes the fiducial volume not more than once (no matter where, be it from the downstream face, or from the borders, or from the upstream face). All tracks which escape twice, are defined passing through tracks and thus are not related to the event. After low momentum track rejection, on average 40 stopping tracks are found in the fiducial volume.

Most of the surviving tracks clearly are still background: in fact, they are originated from fragments of low momentum tracks that ECVTXA was not able to reconnect and eliminate. Completely isolated segments are eliminated. Still included are the fragments of low momentum tracks made of two (or more) connected segments: since the minimum number of connected segments necessary to form a standalone track is 2, that fragment of a low momentum track is already considered a stopping track itself. One could increase the number of segments that form a track, but the price of this is a loss in the tracking efficiency. It was preferred to leave a bigger contamination but also higher efficiency, and use other methods to reject the background.

One of such methods is based on tighter cuts during the vertex reconstruction. At first stage, stopping tracks are considered two by two and two track vertices are constructed. The requirement for two tracks to form a vertex is that the distance between them is less than 20 μm. Also single segments can be reincluded, provided they are matched at less than 30 mrad with a target tracker track, but at least one of the two tracks building the vertex must be connected in two plates. Two track vertices are then clustered to form a real vertex, requesting that the distance between two tracks that form the two track vertices is less than 10 μm.

On average 3.9 vertices are reconstructed per event. At this level, no hypothesis is done on the reliability of the vertices. In the following we shall see that the validation of the target tracker is needed to discard fake vertices.

An example of located vertex as seen with the microscope is shown in Fig. 3.6.

Figure 3.6: Microscope view of a vertex found in the emulsions. The depth of images goes down with the beam direction. The two tracks of charged particles marked with arrows get closer as they approach the neutrino interaction point. The black tracks that are seen at 0 μm depth are highly ionazing nuclear fragments and slow hadrons.

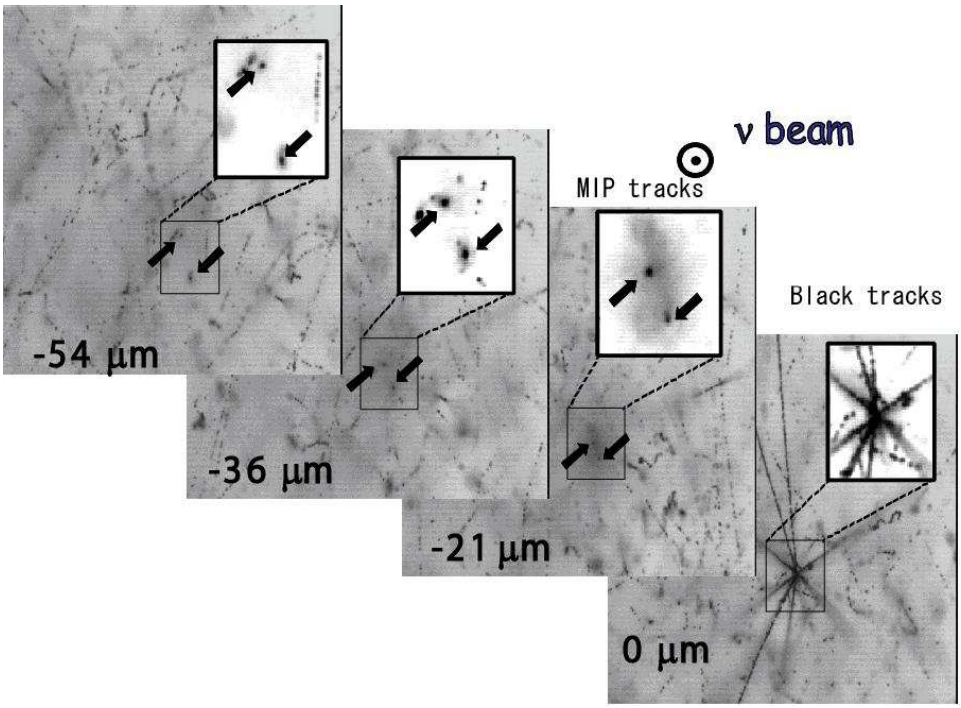

3.3.4 Charm selection

Once the vertex reconstruction has been performed, one defines a primary vertex (and its associated tracks) and possibly one or more secondary vertices to which daughter tracks are attached. To select interesting decay topologies while preserving a good efficiency for charmed hadron detection, the following selection is applied:

- The primary muon track and at least one of the daughter tracks are detected in more than one plate and the direction measured in the emulsion matches that reconstructed in the fiber tracker system.
- The parent angle should be within $\theta_p < 400$ mrad

- A cut is made on the impact parameter of the secondary tracks $IP > \sqrt{5^2 + (2\sigma dx)^2} < 130$ μm, where dx is the vertex depth from the downstream surface of emulsion sheet and $\sigma = \sqrt{0.003^2 + (0.0194 \cdot \tan\theta)^2}$.

- The flight length of a candidate is more than 25 μm.

The parameters are shown in Fig. 3.7.

The events which have passed the criteria described above are considered as charm candidates. However, such a selection would have a significant background from false vertices, non-charm hadronic decays, gamma-rays conversion, etc. In order to improve the charm selection purity every selected event has passed through eye check. The manual scanning also allows to precisely reconstruct the charm decay topology and to measure the parameters of the secondary tracks.

The possibility of manual scanning is the greatest advantage of emulsion experiments over the other types of detectors. The price that is paid for such an advantage is the time needed to perform the scanning and certainly it requires experience. On average, it takes about fifteen minutes to scan one event. This results in limited statistics of the charm sample. But, then again, the background is much smaller compared to the other types of experiments.

From the current sample of 93 890 scanned and analyzed events, charm selection criteria select 2963 events which have been visually inspected to confirm the decay topology. A secondary vertex is accepted as a decay if the number of charged particles is consistent with charge conservation and no other activity (blob because of nuclear evaporation or an Auger-electron) is observed. During the eye-check charm candidates have been subdivided into

Figure 3.7: The parameters that are used to apply the charm selection criteria.

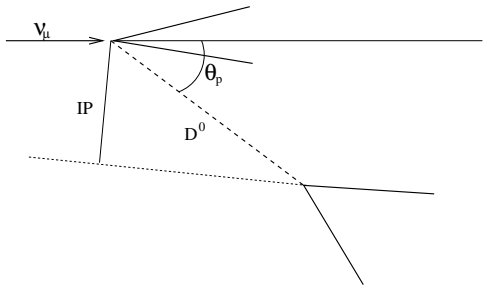

several sub-samples by the number of charged daughters (sometimes called prongs), that is C1 stands for one charged daughter of charged charm, V2 for two daughters of neutral charm, etc. It is worth noting that the net three momentum of the charged daughters is not necessarily conserved because of possible neutral daughters. The result of the visual inspection is given in Table 3.3. The purity of the automatic selection is found to be 73.2%. The rejected sample consists mainly of hadronic interactions, δ-rays or gamma conversions ($\sim$ 35%) and of low momentum tracks which, due to multiple scattering, appear as tracks with a large impact parameter ($\sim$ 55%). The remaining 10% consists either of false vertices, being reconstructed using one or more background tracks, or of vertices with a parent track not connected to the primary vertex. The details are summarized in Table 3.3.

Table 3.3: The number of charm candidates in each prong sample and the relative number of background events in the various samples

Decay topology	**Charm candidates**	**Background events**
C1	452	43.3±2.4
V2	819	36.6±3.5
C3	491	3.8±0.2
V4	226	negligible
C5	22	1.5±0.1
V6	3	negligible
Total sample	2013	85.2

There is a non-negligible fraction of non-charm events in the manually confirmed sample. This contamination is mainly due to hadronic interactions that fake charm decays (white kinks), and decays of $\Sigma^{\pm}$, K^0_s and Λ^0. The backgrounds from the decays of the strange particles were estimated using the JETTA [55] MC generator which is based on LEPTO 6.1 [57]. The production rate of the strange particles normalized to the charged-current events was found to be consistent with the NOMAD data [64, 65]. The last column of Table 3.3 shows the number of background events in the charm decay topologies.

3.4 Data and Monte Carlo comparison

Before going into the discussion concerning the selection efficiency, let make ourselves confident about the description of the data by the simulation. In the following Figures 3.8, 3.9, 3.10 the general kinematical quatities are compared for the charm sample and the charm from the Monte Carlo. It is worth mentioning that the shown distribution for E_{shower} is not the original MC spectrum. Original MC data are slightly different from the presented distributions. This is taken into account by fitting MC distributions to the real data using a linear function. The corrected value for the MC is

$$E^{\text{corr}}_{\text{shower}} = 0.9 E_{\text{shower}} \ . \tag{3.2}$$

The simulated data have been tuned on the charged current events and not specifically for charm data. As it is seen from the plots, in average the agreement between the charm real data and the simulated data sample is good.

Figure 3.8: Data vs Monte Carlo comparison of the primary muon momentum for the events with charmed hadrons.

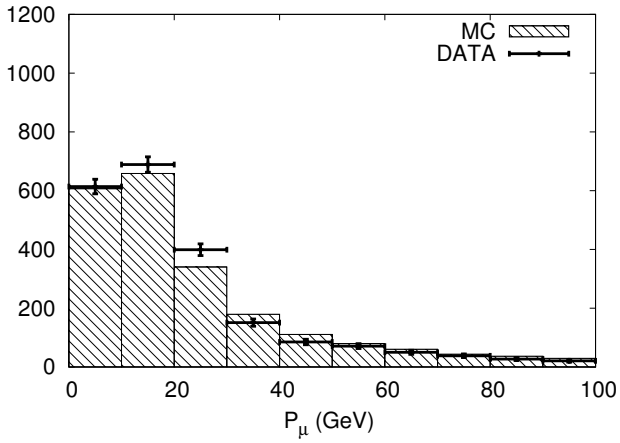

Figure 3.9: Data vs Monte Carlo comparison of the hadronic shower energy for the events with charmed hadrons.

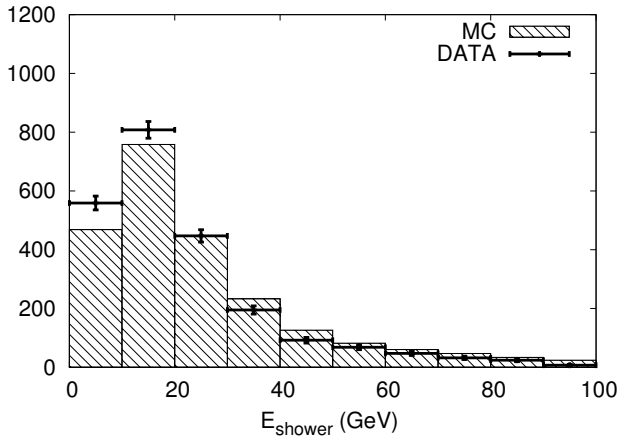

Figure 3.10: Data vs Monte Carlo comparison of the the visible energy (defined in 5.3.1), for the events with charmed hadrons.

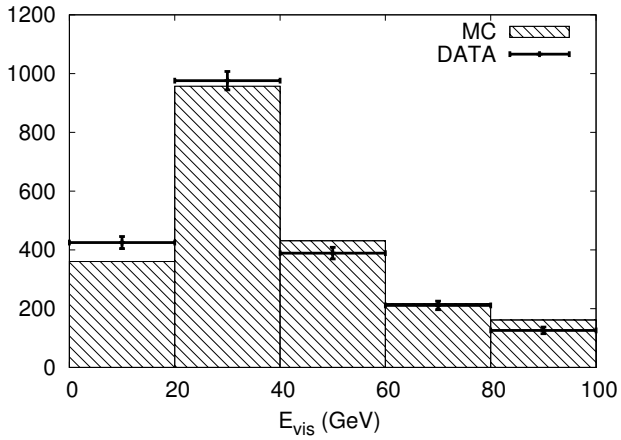

3.5 The charm selection efficiencies

The event selection efficiency is a function of many variables: charm species, flight path, energy of the charmed hadron, number of prongs (decay daughters), etc. It also depends on particle identity of the decay daughters. For example, the selection efficiency for charmed hadrons decaying muonically is different from an inclusive charm selection efficiency. This fact, of course, has to be taken into account in the estimation of the muonic branching ratio of the charmed hadrons. Thus, the sixteen average efficiencies are to be estimated: four charm species times two decay topologies and similar to the previous but considering only muonic decays. Let us look at it a bit closer to be sure that the dependencies can be qualitatively understood.

Figures 3.11 and 3.12 show the efficiency dependence as a function of the flight length per each charm species and per each decay topology. The low value of the selection efficiency at short flight lengths is explained by the difficulty to separate the two vertices. If a track from the seconday vertex is attached to the primary then the efficiency to reconstruct the secondary vertex becomes lower. At long flight paths the selection efficiency goes down because the decay point is quite close to the edge of the fiducial volume then few secondary tracks can be reconstructed. The simulation shows that approximately 3% of D^0 decay out of the fiducial volume, 12% of D^+, 3% of D_s^+ and <1% of Λ_c^+.

Figure 3.13 shows the selection efficiency as a function of the visible energy. The dependence between the two is due to the correlation between the incident neutrino energy and the charmed hadron Lorentz-boost factor.

Figure 3.11: Dependence of the charm selection efficiency as a function of the flight path for D^0 (top) decaying into two prongs and four prongs and D^+ (bottom) decaying into one and three prongs respectively. At low $E_{\rm vis}$ the efficiency is lower because the primary and secondary tracks go out of the fidicial volume. At high $E_{\rm vis}$ the selection efficiency goes down because the charmed hadrons go out of the fiducial volume.

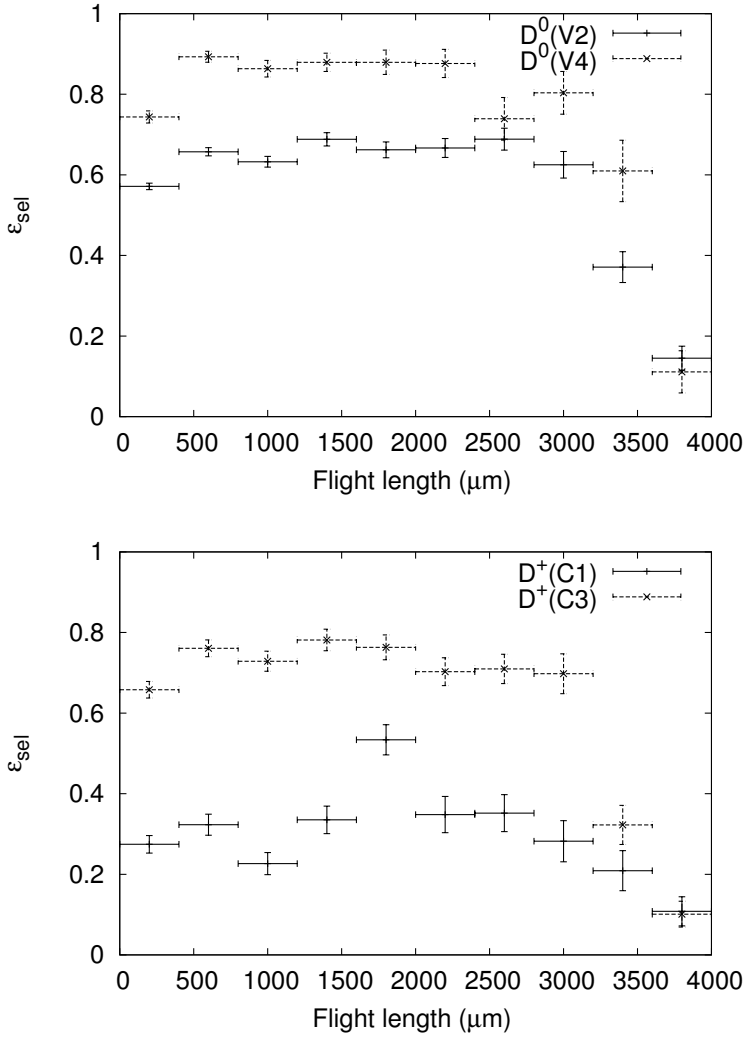

Figure 3.12: Dependence of the charm selection efficiency as a function of the flight path for D_s^+ (top) and Λ_c^+ (bottom) decaying into one and three prongs.

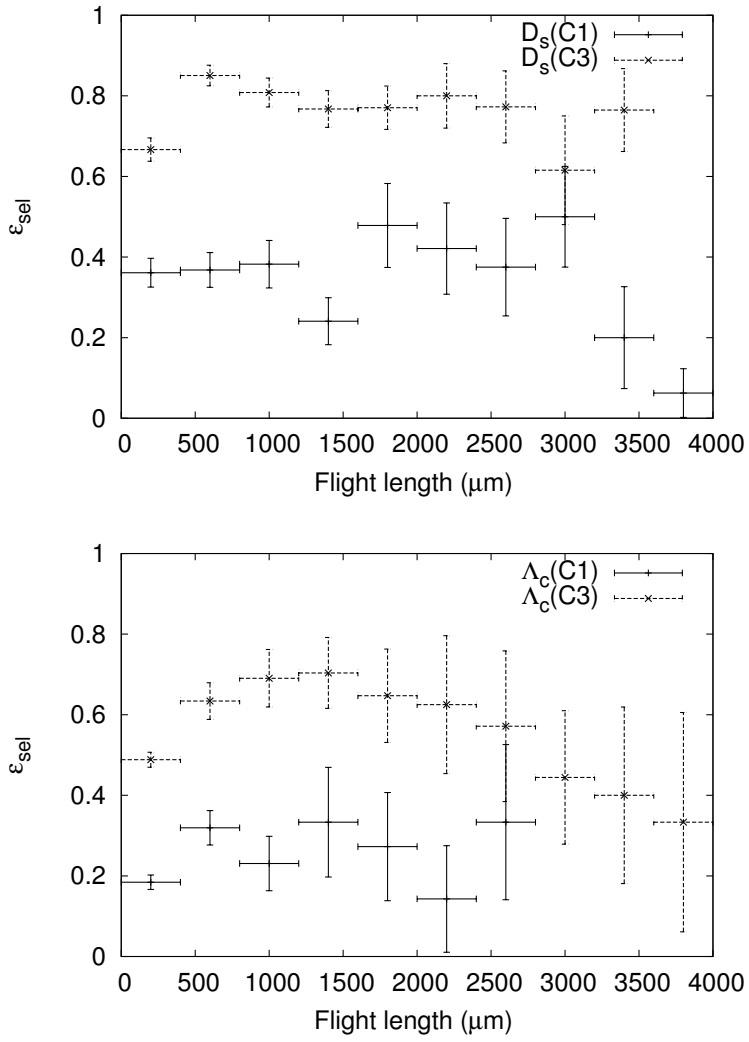

Figure 3.13: Dependence of the charm selection efficiency as a function of the visible energy. The histogram shows the simulated distribution before the selection.

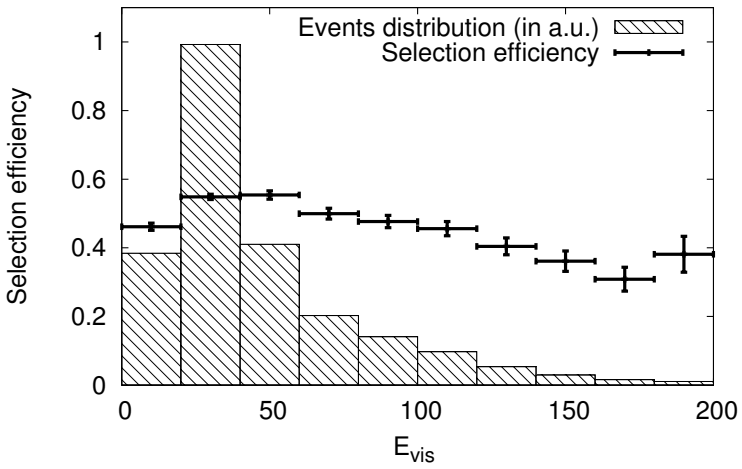

The determination of the muonic branching ratio of charmed hadrons depends on the ratio of the selection efficiency for all decay modes of these hadrons (D^0, D^+, D_s^+ and Λ_c^+) and for their specific muonic decay channels. The other charmed hadrons disintegrate through strong or electromagnetic interactions into these four charmed particles. The difference in the reconstruction efficiency is taken into account by introducing the following factor for each number of prongs n:

$$R(n\text{-prong}) = \frac{\sum\limits_{D_i \to n} f_{D_i} \varepsilon_{D_i}}{\sum\limits_{D_i \to n} f_{D_i} \varepsilon^{\mu}_{D_i}} \ , \tag{3.3}$$

where, for example, the sum is taken over D_s^+, D^+ and Λ_c^+ if n is odd. The quantities f_{D_i} are the charm production fractions which include the different charm production processes, ε_{D_i} is the selection efficiency for different charm species, $\varepsilon^{\mu}_{D_i}$ is the selection efficiency for the charm particles with a muonic decay. For $D^0 \to$V2 or V4 (decay of a neutral particle into two or four charged prongs), the R-factor becomes just the ratio of these two

Table 3.4: Charm production fractions times the branching ratio to decay topology from a reanalysis of the E531 data (second column) [67] and from the JETTA generator (third column). The fractions take into account the branching fraction of the D^0 into final states with all neutrals [66] and they are normalized to the total charm production. The last two columns represent the average selection efficiency and the selection efficiency for decays with a muon in the final state. The efficiencies are normalized to the events located in the emulsion. The average charm selection efficiency is $\varepsilon_{\rm sel}^{\rm charm} = 0.51$ where the errors are negligible.

D^0	f_{D^0}(E531)	f_{D^0}(JETTA)	ε_{D^0}	$\varepsilon^{\mu}_{D^0}$
V0	0.12	0.11	0	–
V2	0.38	0.38	0.57±0.01	0.61±0.02
V4	0.09	0.09	0.75±0.01	0.78±0.02

D^+	f_{D^+}(E531)	f_{D^+}(JETTA)	ε_{D^+}	$\varepsilon^{\mu}_{D^+}$
C1	0.07	0.10	0.24±0.01	0.29±0.02
C3	0.07	0.12	0.53±0.01	0.56±0.03

D_s^+	$f_{D_s^+}$(E531)	$f_{D_s^+}$(JETTA)	$\varepsilon_{D_s^+}$	$\varepsilon^{\mu}_{D_s^+}$
C1	0.06	0.03	0.33±0.02	0.39±0.08
C3	0.05	0.04	0.70±0.02	0.77±0.05

Λ_c^+	$f_{\Lambda_c^+}$(E531)	$f_{\Lambda_c^+}$(JETTA)	$\varepsilon_{\Lambda_c^+}$	$\varepsilon^{\mu}_{\Lambda_c^+}$
C1	0.08	0.03	0.21±0.02	0.25±0.05
C3	0.07	0.05	0.52±0.02	0.58±0.14

efficiencies, since f_{D_i} cancels out. The R-factor can similarly be defined for a mixture of different topologies. The second and third columns of Table 3.4 show different estimations of the fractions. In both cases, the same value of the branching ratio of the D^0 into final states with all neutral particles is used [66]. One (JETTA) is the model used in the Monte Carlo, the other one (E531) is the only direct measurement of the fractions in the literature [15, 16]. These results on the charged charm decay topologies are split here into two different categories, C1 and C3. It is worth stressing that the exact values of the production fractions are not very important because the event reconstruction efficiency does not change dramatically from one charm

species to the other one and the effect is further weakened when taking the sum. For this particular analysis, the ratio $\varepsilon_{D_i}/\varepsilon^{\mu}_{D_i}$ plays a more important role than the production fractions. Nevertheless, a systematic error on R is introduced as a result of choosing the two different sets of the fractions f_{D_i}. In many cases, the errors on R may be neglected since they are small with respect to the other sources. The values of the R factor are summarized in Table 3.5.

Table 3.5: The values of the R-factor defined in the text for different charm decay topologies and their mixtures. The systematic errors include the uncertainty on charm production fractions. The first error quoted is statistical and, when present, the second is the systematic error. The inclusive case is corrected for D^0 into neutrals according to Table 3.4. The C5 and V6 samples are omitted because of low statistics.

Topology	R
C1	$0.83 \pm 0.06 \pm 0.01$
V2	0.93 ± 0.02
C3	$0.92 \pm 0.06 \pm 0.01$
V4	0.96 ± 0.02
C1+C3	$0.89 \pm 0.04 \pm 0.01$
V2+V4	$0.94 \pm 0.01 \pm 0.01$
Inclusive	$0.80 \pm 0.01 \pm 0.01$

3.6 Anti-neutrino charged current sample

The results presented in this section come from the analysis concerning anti-neutrino charm production Refs. [68, 69]. More details can be found in the original works.

An event is considered as a charged current interaction if there is at least one muon identified in the muon spectrometer. The magnetic field of the spectrometer is oriented to bend the positively charged muons from the centre. Thus, it is possible to measure the charge of particles. Knowing the charge of the primary muon it is possible to separate neutrino interactions from anti-neutrino ones. On top of 93807 charged current candidates, there are 2704 events with a good positive muon (or of the highest-energy muon in case of multimuon events). These events are identified as $\bar{\nu}_\mu$ charged current

Table 3.6: Estimated background in the μ^+ sample of located events. The first error is statistical and the second is systematic. The systematic errors take into account the uncertainty on the beam flux measurement [43].

μ^+ sample	2704 event
wrong μ^- reconstruction	$169 \pm 28 \pm 17$
μ^+ from charm decay	$79 \pm 16 \pm 8$
π, K punch-through	$284 \pm 45 \pm 28$

interactions. There is certainly a background in such a definition. To obtain the sample of $\bar{\nu}_\mu$ charged current interactions, one has to account for:

- ν_μ charged current events with μ^- reconstructed as μ^+;
- ν_μ-induced dimuon events for which the primary muon is not reconstructed in the spectrometer while the μ^+ from the charmed hadron decay is seen;
- punch-through hadrons traversing the 5.2 interaction lengths of the calorimeter and reconstructed as positive muons in the muon spectrometer, in charged current events with no identified μ^-, or in neutral current interactions.

It was estimated that the contribution from π and K decays into a μ reconstructed in the specrometer is negligible. A detailed simulation of the experiment has been performed to evaluate these contributions as well as the overall detection efficiencies. The various contaminations to the sample of μ^+ located events, shown in Table 3.6, have been statistically subtracted to estimate the total number of $\bar{\nu}_\mu$ charged current interactions. They represent together $(19.7 \pm 2.1)\%$ of the complete anti-neutrino sample.

The detection efficiencies for ν_μ and $\bar{\nu}_\mu$ charged current interactions have been evaluated, taking into account the efficiencies of the muon reconstruction (including charge determination), the tracking downstream to the emulsion stack, and the scanning-back to the primary vertex plate. Their average values are presented in Table 3.7.

Applying the correction for the detection efficiency on the anti-neutrino sample, it is possible to estimate the ratio of $\bar{\nu_\mu}$ and ν_μ interaction rates in the emulsion. It is found to be 0.021 ± 0.001. This result is in good agreement with the previous measurement of 0.022 ± 0.001 which is based on the calorimeter data (see Table 2.1).

Table 3.7: Detection efficiencies for $\bar{\nu}_\mu$ and $\nu_\mu$induced events with at least one muon in the spectrometer. The errors include the uncertainty from the Monte Carlo statistics.

	$\epsilon_{\text{det}}(\%)$
$\bar{\nu}_\mu$ CC	43.7 ± 0.6
ν_μ CC	40.3 ± 0.4
$\bar{\nu}_\mu$ CC charm	28.2 ± 1.0
ν_μ CC charm	32.2 ± 0.2

Table 3.8: Results of the visual inspection per decay topology for anti-neutrino sample.

Number of prongs	Number of events
C1	6
V2	18
C3	7
V4	7
C5	2

Charm selection criteria (see Section 3.3.4) select 81 events for visual inspection out of 2704. From these events 40 have been confirmed to have a decay topology consistent with charm. The results of the visual inspection are shown in Table 3.8 as a function of the number of prongs. The corresponding selection efficiencies are shown in Table 3.9. The C5 sample is kept here to preserve the consistency with the original work [68].

The detection efficiencies for charm events are shown in Table 3.7. These efficiencies are estimated by combining the efficiency to reconstruct muon in the spectrometer, perform the tracking downstream the emulsion stack and to find the interaction vertex. Their values are somewhat lower than the average detection efficiencies for charged current interactions. This can be explained by two effects: the average track multiplicity in charm events is higher and the momentum and angular distributions of the primary muons are different in charm and all charged current events (Ref.[69]).

There is still a large fraction of background in the sample presented in Table 3.8. The major part of it is from the ν_μ-induced charm events for which either the primary μ^- was reconstructed as a μ^+ or the μ^+ track

Table 3.9: Charm selection efficiency containing geometrical acceptance and reconstruction efficiency for decays of hadrons produced in $\bar{\nu}_\mu$ charged current interactions. Similar efficiencies for ν_μ-produced charm are shown in Table 3.4. The contribution from charmed D^- and D_s^- mesons was evaluated assuming $D_s^+/D^- = 0.627 \pm 0.073$ [70] and the production ratio as obtained in Ref. [71, 72]. The errors include limited Monte Carlo statistics, instrumental effects and the uncertainty on D_s^+/D^-.

	$\bar{D}^0$	$D^- + D_s^-$
C1	-	31.0 ± 5.2
V2	53.7 ± 2.5	-
C3	-	56.3 ± 5.0
V4	68.4 ± 4.7	-
C5	-	60.5 ± 24.4

coming from charm decay was wrongly attached to the primary vertex. To reduce this background, stronger criteria on the muon identification have been applied to the event candidates:

- low momentum muons stopping inside the spectrometer, for which the reconstruction is based on few hits in the electronic detectors, are discarded;
- the distance of the impact point on the spectrometer entrance surface from its axis is required to be smaller than 150 cm, ensuring a long potential path through the toroidal magnets;
- several muon reconstruction algorithms in the spectrometer are available, using only hits in the drift chambers or the combined data from all electronic detectors. Consistency checks are applied when a muon track is reconstructed by more than one algorithm. Otherwise, the track length is required to be greater than three spectrometer gaps (two magnets);
- when matching a spectrometer track with a track in the fiber trackers, a tighter cut is applied on the χ^2 of the global track fit.

With the above primary muon identification criteria, the probability to select a ν_μ event as a $\bar{\nu}_\mu$ goes down from $(0.12 \pm 0.02)\%$ to $(0.02 \pm 0.01)\%$ while still preserving good selection efficiencies [69].

The other important sources of backround are:

- White kinks. These are hadronic interactions with no highly ionizing tracks or other evidence (blobs or Auger electrons). Such interactions look very similar to C1 topology.
- Neutral strange particles that mimic V2 charm decay although in average they have a much longer flight path.

The backroung sources contributing to three or more prong decays were found to be negligible. The total number of background events was estimated to be 3.2±0.3.

The final sample is shown in Table 3.10. Combining the numbers with the efficiencies from Table 3.9 gives an average for charm selection efficiency

$$\bar{\varepsilon}_{\text{sel}}^{\text{charm}} = 0.53 \pm 0.02, \tag{3.4}$$

where the error includes the uncertainty on the selection efficiencies. Bearing in mind that the neutrino and anti-neutrino beams were not the same, this value should be compared to the average neutrino produced charm selection efficiency from Table 3.4.

The charm production rate in charged current interactions induced by $\bar{\nu}_\mu$ normalized to the $\bar{\nu}_\mu$CC sample is found to be [68]:

$$\frac{\sigma(\bar{\nu}_\mu N \to \mu^+ \bar{c} X)}{\sigma(\bar{\nu}_\mu N \to \mu^+ X)} = [5.0^{+1.4}_{-0.9}(\text{stat}) \pm 0.7(\text{syst})]\% \ . \tag{3.5}$$

A similar ratio is not given for the charm production because the analysis is still going on. A very preliminary estimation is made in the Chapter 5.

Table 3.10: Candidate events and estimated backgrounds for each decay topology after applying a stronger primary muon definition. The last column shows the number of events background subtracted and charm selection efficiency corrected. The first error is statistical and the second is systematic. The statistical errors have been evaluated according to the statistical approach from Ref. [84].

Decay topology	Events	Background	Weighted sample
C1	4	1.3 ± 0.2	$8.6^{+9.1}_{-5.1} \pm 1.4$
V2	16	1.4 ± 0.2	$27.2^{+8.9}_{-6.8} \pm 1.3$
C3	4	0.3 ± 0.1	$6.5^{+5.0}_{-2.9} \pm 0.6$
V4	6	0.13 ± 0.05	$8.6^{+4.8}_{-3.1} \pm 0.6$
C5	2	0.02 ± 0.01	$3.3^{+3.8}_{-2.1} \pm 1.3$

Chapter 4

Muonic branching ratio

In this chapter, the measurement of the topological muonic branching ratios for different charm decay topologies is described. Using the obtained results, several physical quantities are extracted.

4.1 Muon identification

Particles recognition plays an essential role in the high energy physics experiments. The muon identification procedure is important not only for the selection of muons coming from the decays of charm but also to separate charged current neutrino interactions from neutral current ones. Most of the identification algorithms rely on the fact that different sorts of particles interact differently with matter. It is well known that the muons penetrate further into the detector with respect to the electrons and the hadrons provided they have similar incident energy. This what makes them easier to detect. The interactions of muons in the media leads to a threshold on the muon momentum and the geometrical acceptance.

A new algorithm MURECO has been developed to identify muons for the CHORUS experiment. This algorithm delivers a set of basic estimators to the user. The user can combine the estimators to boolean expressions and decide if a track is a muon or not. The boolean expressions depend on the cuts chosen for each basic estimator. The values of the cuts will depend on the kinematic properties of the studied muons.

The MURECO algorithm has been implemented as a module of our general event reconstruction framework CHANT and uses information from the downstream part of the calorimeter and from the spectrometer. It is track driven, which means that, providing the track parameters from either

emulsion or target tracker, it extrapolates the track to the calorimeter and the spectrometer and returns the estimators. Such approach allows to check the tracks found in emulsion and attached to the secondary vertex which dramatically changes the situation if compared to the other measurements which do not require an identified muon to be attached to a vertex. The details on the MURECO algorithm can be found in the note[73].

4.2 Basic estimators

Range measured with scintillators

A cylinder is defined around the extrapolation of the track under concern. The tolerance is different for the two parts of the detector: 7 cm for the calorimeter and 12 cm for the spectrometer. If the center of the scintillator slab lies within the road, it is considered. The track is seen if one of the signals around the road is greater than the threshold value of 0.2 minimum ionizing particle signal (MIP).

A schematic representation of the estimator construction is shown in Fig. 4.1. In total ten planes are used: the last six calorimeter planes and the first four spectrometer readout planes. No distinction is made between the two projections. A subset of four consecutive planes is examined, and a bit is set when three out of the four planes have a hit. There are also two variations of the estimator requiring two out of the four and four out of the four hits respectively. This procedure is repeated shifting the region of four planes each time one plane further downstream. The six bits give a distribution for the tracks from 0 to 63. Fig. 4.2 shows the comparison between the data and the simulation for different types of tracks.

Range and isolation measured with streamer tubes in the calorimeter

The streamer tubes in the calorimeter are used in a similar manner compared to the scintillators. However, this time the two projections are treated independently and two estimators are constructed. Again each time four consecutive planes having the same orientation are examined. The road is defined in two steps shown in Fig. 4.3. First a pivot point is defined as a hit in the most downstream plane out of four that is within the road. Each possible pivot hit, defines a new straight line, using the origin of the measured track and the pivot hit as hypothesis for the trajectory. Then the three upstream planes are checked for the presence of hits. If two planes

out of three have hits then the appropriate bit is set to 1. This algorithm considers only hits in sufficiently isolated clusters (up to three hits) with the aim to reduce the background coming from the hadronic showers. There were in total twenty-two streamer tubes planes. The small planes near the electromagnetic calorimeter were not used leaving nine useful planes in each projection. These form six possible regions of four planes. The possible values are from 0 to 63. The results are shown in Fig. 4.4.

On top of that, isolation estimators are constructed in a similar fashion as the range measured with streamer tubes. The cluster isolation is defined as a minimum distance to the nearest cluster. And again the two projections are treated separetely. The possible values are from 0 to 63. The results are shown in Fig. 4.5

Figure 4.1: Schematic representation of the scintillator estimator construction. The two projections have been merged together for simplicity. The black squares represent a signal above the threshold. The squares outside the road are not considered.

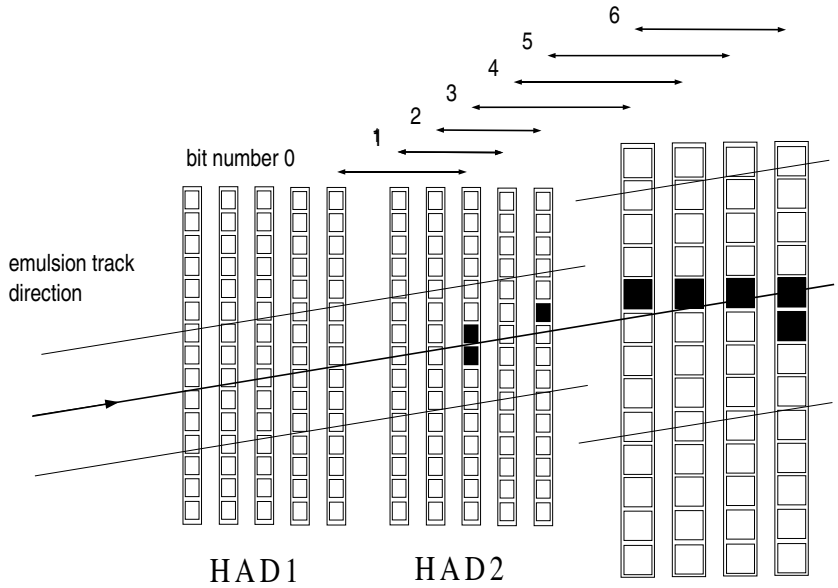

Figure 4.2: Comparison of the scintillators estimator for simulated muons(top) and hadrons(bottom), both coming from charm. The reader should take into account that the normalization is different in the two cases.

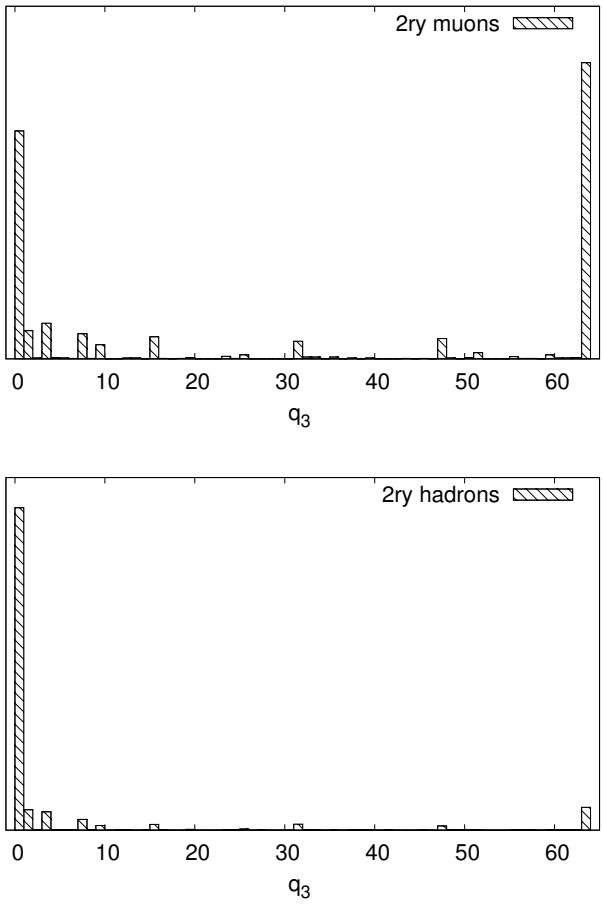

Figure 4.3: Schematic representation of the streamer tube estimator construction. The tubes in the planes are shown as squares. The pivot hit is shown as filled square in the most right plane. A new trajectory is defined connecting this hit to the track origin. The new road is in general different from the original one as shown in the figure. Only one region is shown.

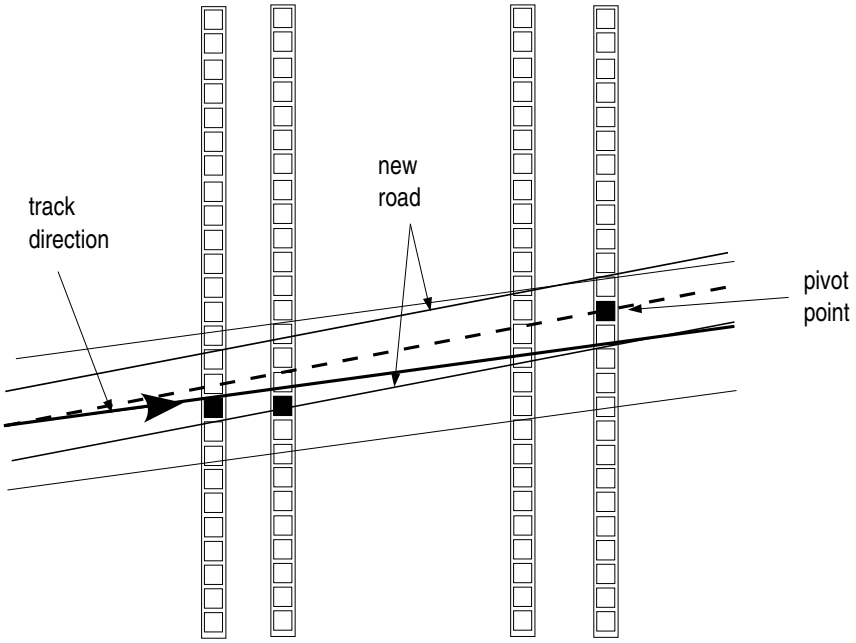

Figure 4.4: The results for the streamer tubes estimators.

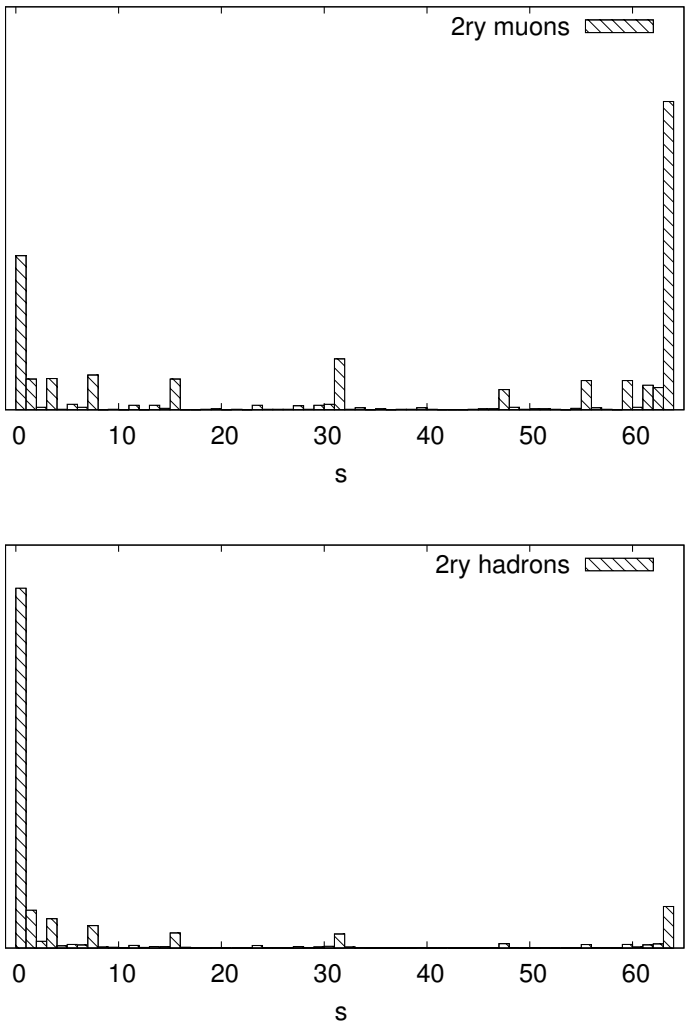

Figure 4.5: The distribution of the isolation streamer tubes estimator for secondary muons(top) and hadrons(bottom).

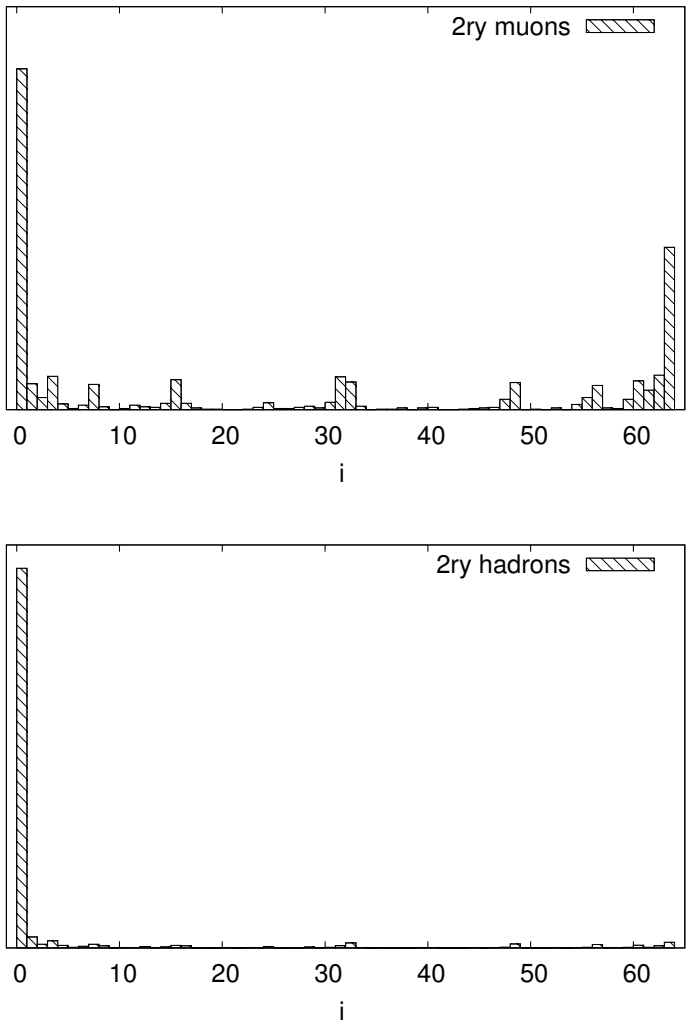

Energy in the calorimeter

Muons coming from charm decay are quite soft particles compared to the primary ones. One of the consequences of that is the difficulty to separate the muons from hadronic showers in the downstream part of the calorimeter. In order to reduce the background coming from the last part of the calorimeter an estimator is constructed which is a sum of the energy deposited in the downstream part of the calorimeter HAD2. The units of this estimator are MIPs.

It was found that there is a discrepancy between the data and Monte Carlo for this estimator. That is why a decision has been made to recalibrate it by fitting simulated charged current data to the real charged current data using a linear function. As a result the systematic error on the muonic branching ratios has been reduced. The output of the fit is shown in Fig. 4.6 and the numerical values are

$$E^{\text{corr}}_{\text{HAD2}} = 0.83 * E_{\text{HAD2}} + (-3.8 \pm 0.2) \times 10^{-3}, \tag{4.1}$$

where the error is from the fit. The error on the E_{HAD2} slope coefficient is negligible.

4.3 Muon identification criteria

The muon identification algorithm assumes to be ran as a post-scanning routine. Thus the tracks under consideration come from Netscan. These tracks are not necessarily matched to target tracker tracks but they have to be confirmed to belong to any of the vertices related to the event. The confirmation is made by eye-checking the presence of the secondary vertex in the fiducial volume. The information about the vertex of origin gives an enormous advantage in the muon identification because we can use different criteria for the primary and for the secondary muons. It is worth stressing that in the previous measurements [74, 75, 76, 77, 78, 17, 79, 80] the analyses have been made requiring the presence of two (or more) tracks satisfying the same criteria without demanding the attachment of the two tracks to the different reconstructed vertices. By doing so we may count also soft muons from charm that have been scattered, but we also may count muons coming from background (π and strange particles decays). Such a low energy background is very difficult to simulate. The level of the background muons was different in the measurements mentioned above but it unavoidably lead to the increase of the systematic error for all of them. To require a muon

Figure 4.6: The result of the fit of the energy distribution in HAD2 for simulated charged current data and real charged current data. Although a descrapansy is seen at high HAD2, the low HAD2 region containing major part of the events fits well.

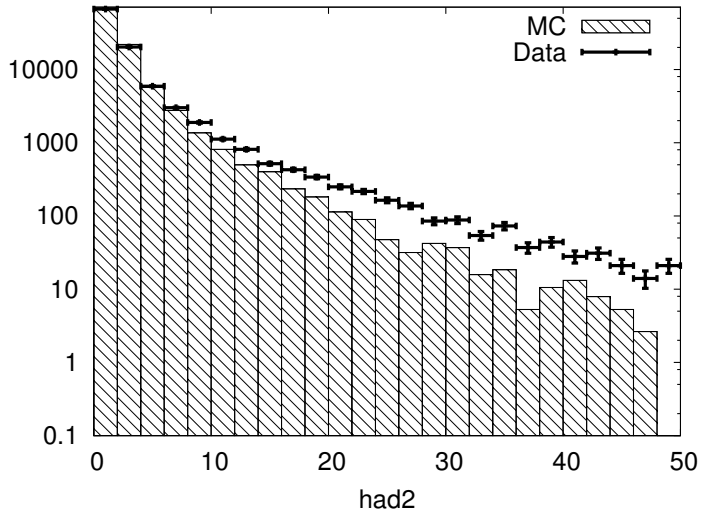

to be attached to the secondary vertex, gives an opportunity to measure muonic branching ratio for each charm decay topology separately and makes the analysis absolutely transparent.

The basic estimators defined in the previous sections are combined to define a "muon flag". This flag is used to separate tracks that resemble the properties of muons from other tracks. So, the track is assumed to be a muon coming from charm decay if it is attached to a downstream secondary vertex found in the fiducial volume and

$$\begin{aligned} &\left[q_3 > q_{\text{cut}} \cap P_\mu > 10^{-3}\right] \bigcup \\ &\left[q_3 > q_{\text{cut}} \cap s_y > s_{\text{cut}} \cap s_z > s_{\text{cut}} \cap (\Delta\theta_y > \theta_{\text{cut}} \cup \Delta\theta_z > \theta_{\text{cut}})\right. \\ &\left. \cap E_{\text{HAD2}} < E_{\text{cut}}\right] \bigcup \\ &\left[q_3 > q_{\text{cut}} \cap s_y > s_{\text{cut}} \cap s_z > s_{\text{cut}} \cap i_y > i_{\text{cut}} \cap i_z > i_{\text{cut}}\right], \end{aligned} \tag{4.2}$$

where q_3 is the version of scintillator estimator requiring three hits in four planes, P_μ is the matching probability between target tracker track and spectrometer track, $s_{y,z}$ are the ranges measured with the streamer tubes in two projections, $\Delta\theta_{y,z}$ are the slope distance from primary muon in two projections, E_{HAD2} is the energy deposited in the downstream part of the calorimeter HAD2 and $i_{y,z}$ are the isolation estimators measured with the streamer tubes. For the secondary muons the values of the cuts were different for each decay topology. The purpose of this was to optimize the statistical and systematical errors. The values of the cuts for secondary muons are presented in Tables 4.1 and 4.2. The muon identification efficiency as a function of the secondary muon momentum is presented in Fig. 4.7. There are several sources of background to this muon definition. Those giving the largest contributions are punch-through hadrons and muons from decays of π's and K's that have been matched to emulsion tracks. All other processes give a minor contribution.

The choice of cuts has been directed by the larger statistics on one side and the symmetrical systematic distributions of the muonic branching ratios on the other side. The latter is discussed in the next section. The number of selected tracks are summarized in Table 4.3.

The physical sources of dimuon events in the four-prong sample are very much suppressed with respect to two-prong events. Because of that, the definition explained above for secondary muons would introduce too much background in the four-prong sample. Therefore, for the V4 sample the tighter requirement of a secondary track associated with a positively charged spectrometer track was applied in order to optimize the signal to background

Table 4.1: The values of the cuts used to identify muons coming from charm for each decay topology. The V4 case is explained in the text. The C5 and V6 samples are omitted due to low statistics in the data.

Number of prongs	q_{cut}	s_{cut}	i_{cut}	E_{cut}
C1	6	6	46	15
V2	6	6	46	15
C3	6	6	52	15
V4	63	63	63	0

Table 4.2: Similar to the previous but per visible energy bin. This time the samples (C1, V2, C3, V4) are mixed together.

E_{vis} bin	q_{cut}	s_{cut}	i_{cut}	E_{cut}
0 GeV $< E_{\text{vis}} <$ 30 GeV	16	7	16	15
30 GeV $< E_{\text{vis}} <$ 50 GeV	56	35	56	12
50 GeV $< E_{\text{vis}}$	47	32	7	15

ratio. This criterion selects two events out of 226. If the spectrometer track is required to have negative charge no events are selected. Background for such events could come from hadronic charm decays with one of the charm daughters decaying muonically. It has also been verified that the muonic background coming from decays of strange particle (K^0_s, Λ^0) daughters is small. A Monte Carlo simulation shows that the level of the muon identification background corresponding to this sample is $(3.4\pm0.4)\times10^{-2}$.

4.4 Systematic uncertainty

The main source of systematic uncertainty on the muonic branching ratio is the systematic error on the secondary muon identification. The selection is not very sensitive to changes in the criteria on the matching with muon tracks found in the spectrometer. However, it does depend on the details of the scintillator range estimator, the streamer tubes range estimator, the isolation measured with the streamer tubes, and the energy deposited in the most downstream part of the hadronic calorimeter. An estimate of the systematic error is obtained by a variation of the cuts on the parameters in the secondary muon identification procedure. For each set of parameters (cuts) applied to the estimators a value of B_μ is obtained. Then the distribution

Figure 4.7: Muon identification efficiency as a function of the muon momentum as obtained with Monte Carlo. Only muons coming from charm decays are presented here. One of the sources of the systematic error is the model parameters that change the spectrum. The histogram shows distribution of secondary muons momenta as obtained with simulation.

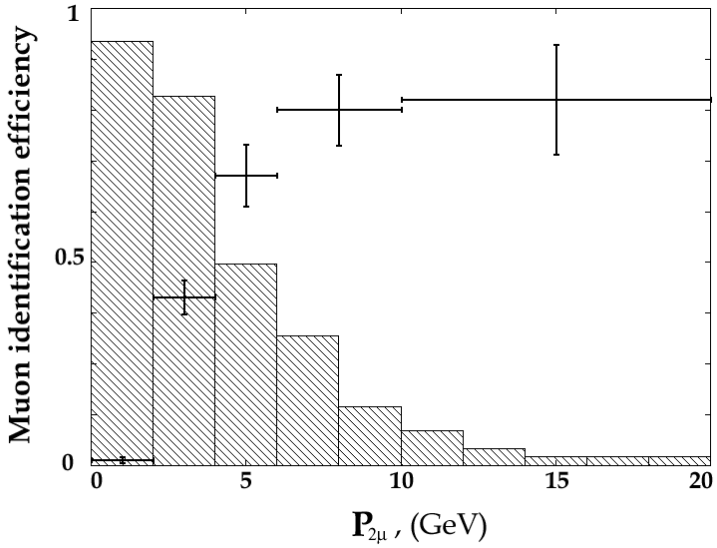

is fit using MINUIT package [81] to the Gaussian probability distribution function with three parameters

$$f(x, N, \mu, \sigma^2) = \frac{N}{\sqrt{2\pi\sigma^2}} \exp\left(\frac{-(x-\mu)^2}{2\sigma^2}\right), \tag{4.3}$$

where N is a normalization factor which has no physical meaning and is omitted further, μ and σ are the mean and standard deviation of the probability distribution function. The results for each dominating decay topology and per energy bin are presented in Tables 4.4 and graphically shown in Fig. 4.8, 4.9, 4.10, 4.11, 4.12, 4.13. Using the charmed fractions from Table 3.4 the systematic errors are obtained for the mixtures of the topologies and for the inclusive measurement. The relative errors are presented in Table 4.5.

Another source of systematic error is the choice of the parameters of the model used in the simulation. The charm quark mass, m_c, the choice

Figure 4.8: The distribution of B_μ obtained by the variation of the cuts in the muon identification for the C1 sample.

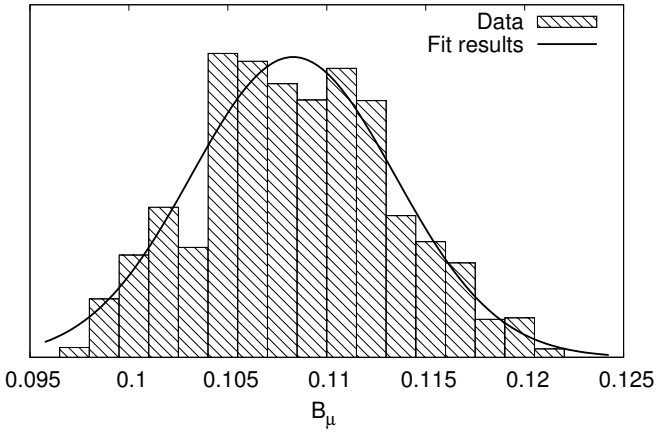

Figure 4.9: The distribution of B_μ obtained by the variation of the cuts in the muon identification for the V2 sample.

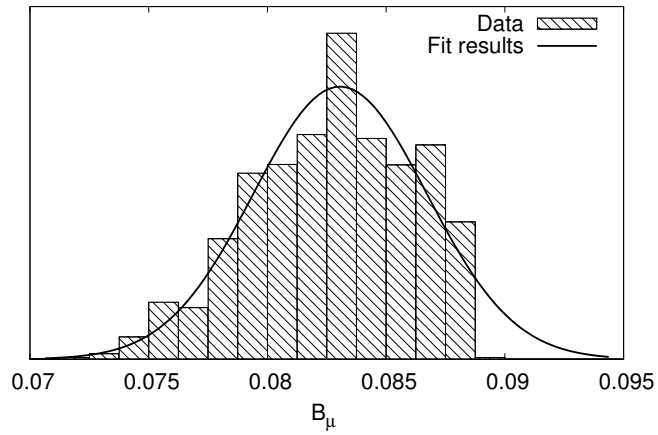

Figure 4.10: The distribution of B_μ obtained by the variation of the cuts in the muon identification for the C3 sample.

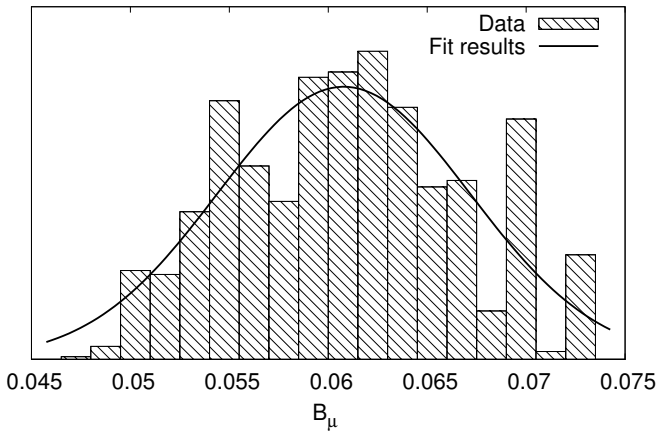

Figure 4.11: The distribution of B_μ obtained by variation of the cuts in the muon identification for the energy bin 0 GeV $< \mathrm{E_{vis}} <$ 30 GeV for the mixed topologies.

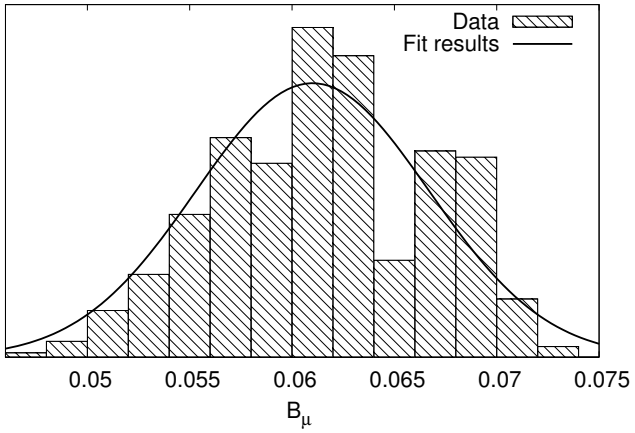

Figure 4.12: The distribution of B_μ obtained by variation of the cuts in the muon identification for the energy bin 30 GeV $<$ E_{vis} $<$ 50 GeV for the mixed topologies.

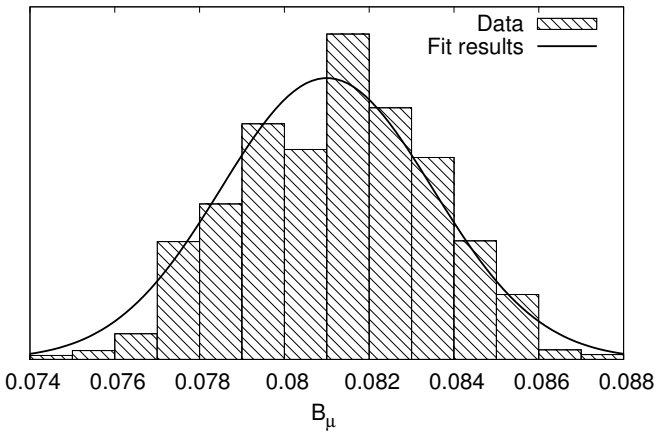

Figure 4.13: The distribution of B_μ obtained by variation of the cuts in the muon identification for the energy bin 50 GeV $<$ E_{vis} for the mixed topologies.

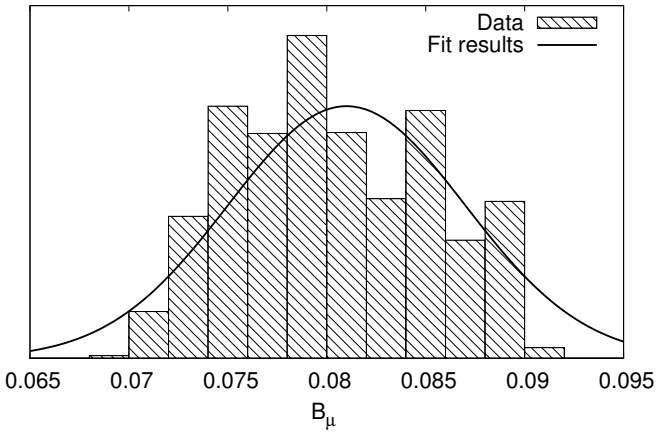

Table 4.3: The number of secondary tracks identified as muons in real data, the background normalized to the number of selected tracks, and the identification efficiency as obtained from simulation. The errors on the identification efficiencies are determined by the limited Monte Carlo statistics. The identification criteria for the V4 sample are explained in the text. In the inclusive case the samples are combined using the weights from Table 3.4.

Number of prongs	**Selected**	**Background**	$\varepsilon_\mu^{\rm id}$,%
C1	20	0.8	36.0 ± 3.4
V2	34	9.8	34.5 ± 1.9
C3	17	8.4	26.4 ± 2.6
C1+C3	37	9.2	31.7 ± 3.1
V2+V4	36	9.8	30.1 ± 1.5
Inclusive	73	19.0	30.4 ± 2.1

of the parton distribution functions, GRV94LO[82] and CTEQ3[83], and the relative fraction of the strange quark sea compared to the down-quark sea, κ, affect the momentum spectrum of the muons coming from charm decays. The variation limits for $m_{\rm c}$ and κ are consistent with the values of the fit parameters describing the energy dependence of the D^0 production cross-section measured with the same sample of events (see Ref. [66]): $m_{\rm c} = 1.42 \pm 0.08$ GeV/c^2 and $\kappa = 0.38 \pm 0.10$. The relative systematic error obtained in this manner corresponding to one standard deviation is equal to $\sigma_{\rm syst}^{\rm model}$ =1.6% to be compared with the $\sigma_{\rm syst}^{\rm id}$, Table 4.5.

4.5 Results

B_μ^n, the muonic branching ratio for each n-prong sample, can be written in terms of measurable quantities as

$$B_\mu^n = \sum_i f_{D_i}^n B^n(D_i \to \mu^+ X) = \frac{N_{2\mu} - N_{\rm bg}}{N \cdot \varepsilon_\mu^{\rm id}} \times R(n\text{-prong}), \qquad (4.4)$$

where the sum is taken over the contributing charmed hadrons, N is the total number of events in the n-prong sample corrected for non-charm background, $N_{2\mu}$ is the number of tracks identified as secondary muons, $N_{\rm bg}$ is the number of background tracks in $N_{2\mu}$ from Table 4.3, and ε_μ^{id} is the

Table 4.4: The results of fit as an estimate of the systematic error on the muonic branching ratio for the each sample and inclusively per energy bin. The mean can be reinterpreted as an average B_μ while the standard deviation is the systematic error on it. The uncertainty on μ and σ and the correlation coefficient ρ are from the fit.

Number of prongs	μ	σ	ρ
C1	$[10.83 \pm 0.35] \times 10^{-2}$	$[5.14 \pm 0.34] \times 10^{-3}$	0.022
V2	$[8.31 \pm 0.02] \times 10^{-2}$	$[3.66 \pm 0.21] \times 10^{-3}$	-0.113
C3	$[6.08 \pm 0.08] \times 10^{-2}$	$[6.4 \pm 0.79] \times 10^{-3}$	0.068

Energy bin	μ	σ	ρ
$0 < E_{vis} < 30$ GeV	$[6.16 \pm 0.06] \times 10^{-2}$	$[5.74 \pm 0.56] \times 10^{-3}$	0.036
$30 < E_{vis} < 50$ GeV	$[8.13 \pm 0.02] \times 10^{-2}$	$[2.46 \pm 0.22] \times 10^{-3}$	-0.061
$50 < E_{vis}$	$[8.1 \pm 0.07] \times 10^{-2}$	$[6.12 \pm 0.59] \times 10^{-3}$	0.273

Table 4.5: The relative systematic errors on the muonic branching ratio from the muon identification for different decay topologies and their mixtures.

Topology	$\sigma^{\text{id}}_{\text{syst}}$ (%)
C1	4.7 ± 0.3
V2	4.4 ± 0.2
C3	10.7 ± 0.8
V4	negligible
C1+C3	5.6 ± 0.4
V2+V4	3.6 ± 0.2
Inclusive	3.3 ± 0.1

Table 4.6: The muonic branching ratios for different prong samples and their mixtures. The first error quoted is statistical and the second is the systematic error. The statistical errors include the uncertainty on the number of identified muons and the error on the identification efficiency.

Number of prongs	$\overline{B}_\mu$ (%)
C1	$10.8 \pm 2.4 \pm 0.5$
V2	$8.3 \pm 1.4 \pm 0.4$
C3	$6.1 \pm 1.6 \pm 0.6$
C1+C3	$8.6 \pm 1.4 \pm 0.4$
V2+V4	$8.1 \pm 1.5 \pm 0.3$
Inclusive	$7.3 \pm 0.8 \pm 0.2$

secondary muon identification efficiency. The inclusive value of the ratio is calculated as a weighted sum of the ratios per topology

$$\overline{B}_\mu = \sum_n f_{C_n} \cdot B(C_n \to \mu^+ X), \tag{4.5}$$

where C_n can be C1, V2, C3 or V4, and f_{C_n} are the average fractions obtained from Table 3.4. Table 4.6 contains the values of the muonic branching ratios as a function of the number of prongs.

The muonic decay branching ratio of the D^0 could be obtained by combining the results for the two-prong and four-prong samples and taking into account the branching ratio of the D^0 into only neutral particles, $B(D^0 \to$ neutrals), mentioned earlier. This yields

$$B_\mu(D^0) = [6.5 \pm 1.2 \text{ (stat)} \pm 0.3 \text{ (syst)}] \times 10^{-2} \ ,$$

where the systematic error is determined by the precision of the muon identification and on $B(D^0 \to$ neutrals). This result is in agreement with the value $(6.6 \pm 0.8) \times 10^{-2}$ quoted in Ref. [11].

The limit for the V4 decays could be obtained using the Feldman–Cousins approach [84] with a 90% confidence level. The result is normalized to the total D^0 cross-section:

$$3.0 \times 10^{-4} < B_\mu(D^0 \to \text{V4}) < 3.4 \times 10^{-3} \ , \tag{4.6}$$

to be compared with the existing 90% C.L. limit $B(D^0 \to K^-\pi^+\pi^-\mu^+\nu_\mu) < 1.2 \times 10^{-3}$ [85]. It is also consistent with the value using D^0 events in

the emulsion, $2.0 \times 10^{-4} < B(\mathrm{D}^0 \to \mathrm{K}^-\pi^+\pi^-\mu^+\nu_\mu) < 1.5 \times 10^{-2}$ at 90% C.L., which was obtained by counting the number of four-prong charm-decay events with two opposite-charge muons in the final state [86].

The average muonic branching ratio for the C1 and C3 samples taken together could be reinterpreted as the average branching ratio for charged charm hadrons D_s^+, D^+ and Λ_c^+ (taking into account the small number of C5 events).

The inclusive muonic branching ratio for the complete sample of charm hadrons is therefore determined to be

$$\overline{B}_\mu = [7.3 \pm 0.8\ (\mathrm{stat}) \pm 0.2\ (\mathrm{syst})] \times 10^{-2}.$$

Our earlier result, $\overline{B}_\mu = [9.3 \pm 0.9\ (\mathrm{stat}) \pm 0.9\ (\mathrm{syst})] \times 10^{-2}$ [17], was obtained using a value for $B(\mathrm{D}^0 \to \text{neutrals})$ from the observed decay channels only [11]. If the new determination for this topological branching ratio obtained in Ref. [66] is used, the previous result is reduced by $\approx 7\%$. The results are therefore compatible given the entirely different systematic uncertainties of the two measurements. The improvement in the systematic error is significant. Because of the limited statistics of the present sample, the energy dependence of $\overline{B}_\mu$ could be determined in a small number of bins only. The splitting of the total sample into three subsamples ($E_\mathrm{vis} \leq 30$ GeV, 30 GeV $\leq E_\mathrm{vis} \leq 50$ GeV and 50 GeV $\leq E_\mathrm{vis}$) gives results compatible with each other within one standard deviation. The dependence is shown in Fig. 4.14.

Strictly speaking, the muonic branching ratio measured in this analysis can not be compared directly with the results from other experiments because the beam spectra are not the same. As an additional difference it should be mentioned that the present determination is a direct measurement while in the other experiments $\overline{B}_\mu$ was extracted as one of the parameters of a fit to kinematical distributions.

Many explicit final states of the different charmed hadrons have been observed, in particular in $\mathrm{e}^+\mathrm{e}^-$ colliders. However, the inclusive muonic branching ratio has only been measured for the D^0 decays. The values quoted in PDG (Particle Data Group)[11] for the inclusive leptonic branching ratios rare

$$\begin{aligned} B(\mathrm{D}^0 \to \mu^+ \text{ anything}) &= [6.6 \pm 0.8] \times 10^{-2}\ , \\ B(\mathrm{D}^+ \to e^+ \text{ anything}) &= [17.2 \pm 1.9] \times 10^{-2}\ , \\ B(\mathrm{D}_\mathrm{s}^+ \to e^+ \text{ anything}) &= [8^{+6}_{-5}] \times 10^{-2}\ , \\ B(\Lambda_\mathrm{c}^+ \to e^+ \text{ anything}) &= [4.5 \pm 1.7] \times 10^{-2}\ . \end{aligned} \tag{4.7}$$

If it is assumed that electronic and muonic branching ratios are equal and using the charmed fractions from Table 3.4 , one easily gets from Eq.4.5

$$\overline{B}_\mu = [7.8 \pm 0.9] \times 10^{-2},$$

which is in good agreement with the direct measurement. Another estimation can be done by reading Eq. 4.5 in the opposite way: starting from the measurement of the inclusive muonic branching ratio to extract a B_μ for one particular species if the B_μ for the others are known. For example, using $\overline{B}_\mu$ for the C1+C3 sample the muonic branching ratio for D_s^+ can be estimated (because it has the worst precision)

$$B(D_s^+) = \frac{\overline{B}_\mu(C1 + C3) - f_{D^+} B_\mu(D^+) - f_{\Lambda_c^+} B_\mu(\Lambda_c^+)}{f_{D_s^+}}. \tag{4.8}$$

Working out the calculations the ratio is found to be

$$B(D_s^+ \to \mu^+ \text{ anything}) = [4^{+6.5}_{-4}] \times 10^{-2}, \tag{4.9}$$

Figure 4.14: Average muonic branching ratio as a function of visible energy. The value of visible energy for each bin is an average over the events in the bin. The error bars include statistical and systematic uncertainties. The last bin contains all events with neutrino energy larger than 50 GeV.

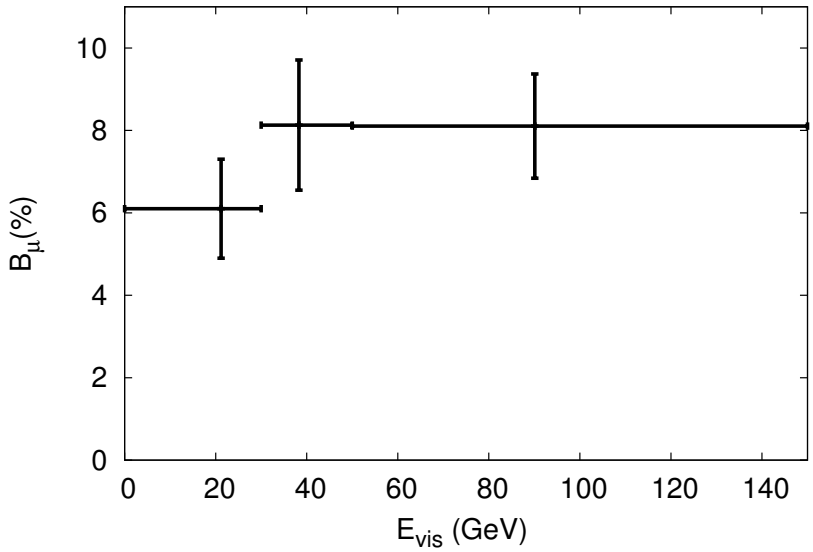

Figure 4.15: Dimuon neutrino cross-section normalized to the charged-current cross-section as a function of visible energy. The solid crosses show CHORUS result and the dashed ones is the average over the other dimuon experiments [87].

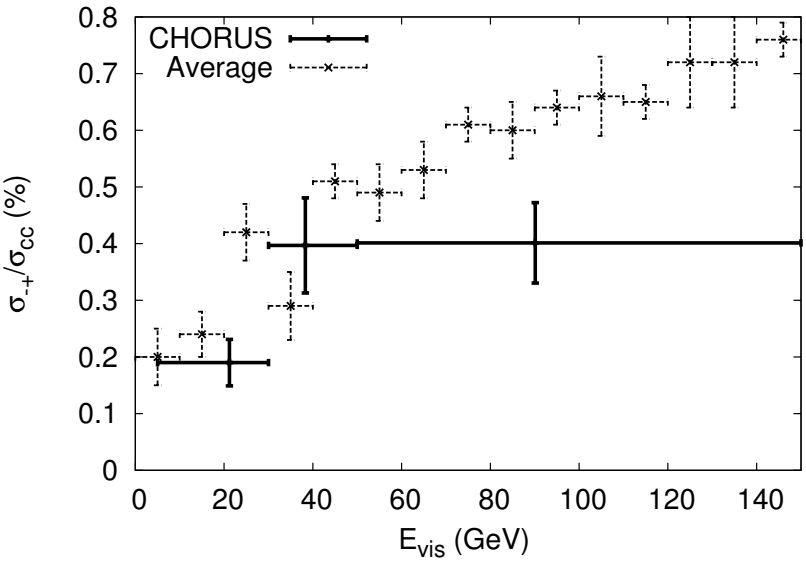

to be compared with Eq. 4.7.

In a similar manner, one can obtain the dimuon cross-section normalized to the charged-current cross-section. In terms of measurable quantities the ratio is

$$\frac{\sigma_{\mu^-\mu^+}}{\sigma_{\rm cc}} = \frac{N_{2\mu} - N_{\rm bkgr}}{N_{\rm cc} \cdot \varepsilon_\mu^{\rm id}} \times \frac{\varepsilon_{\rm loc}^{\rm cc}}{\varepsilon_{\rm loc}^{\rm charm}} \times \frac{1}{\varepsilon_{\rm rec}^{\rm charm}} \ , \tag{4.10}$$

where $N_{\rm cc}$ is the number of charged-current events in a bin, $\varepsilon_{\rm loc}$ are the location efficiencies from Eq 3.1, and $\varepsilon_\mu^{\rm charm}$ is the average event reconstruction efficiency of charm decaying muonically from Table 3.4 (evaluated to be $\varepsilon_\mu^{\rm charm} = 0.57$). The result is shown in Fig. 4.15 as a function of energy. The average value is

$$\frac{\sigma_{\mu^-\mu^+}}{\sigma_{\rm cc}} = [3.16 \pm 0.34 \ ({\rm stat}) \pm 0.09 \ ({\rm syst})] \times 10^{-3} \ .$$

The CCFR experiment has extracted the value for $|V_{\rm cd}|$ by combining its study of opposite-sign dimuon events with a determination of $\overline{B}_\mu$

based on the E531 data, considering only events with a visible energy above 30 GeV [77]. This approach has been adopted by the particle data group as well [11], even though it is then applied on the average over $\overline{B}_\mu |V_{\rm cd}|^2$ measurements from different experiments with leading order (LO) and next-leading order (NLO) analyses which requires an assumption on the scale uncertainty. Our value for $\overline{B}_\mu$ is model independent and thus can be used to extract the values of $|V_{\rm cd}|$ for LO and NLO separately. Averaging the measurements at the leading order by the CDHS, CHARM II and CCFR experiments [67], one would get

$$\overline{B}_\mu \times |V_{\rm cd}|^2 = (0.474 \pm 0.027) \times 10^{-2} \ .$$

Selecting from our sample the events with a visible energy greater than 30 GeV yields a value of

$$\overline{B}_\mu = [8.5 \pm 0.9 \ (\text{stat}) \pm 0.6 \ (\text{syst})] \times 10^{-2} \ .$$

Adding the statistical and systematic errors in quadrature, and combining with the value above we find that

$$|V_{\rm cd}|_{\rm LO} = 0.236 \pm 0.016 \ .$$

Up to now, there is only one measurement at the next-to-leading order by the CCFR experiment [77]

$$\overline{B}_\mu \times |V_{\rm cd}|^2 = [0.534 \pm 0.046 \ (\text{stat}) \ {}^{+0.025}_{-0.051} \ (\text{syst})] \times 10^{-2} \ ,$$

where the last error is from the scale uncertainty. Substituting our value for $\overline{B}_\mu$ and symmetrizing the errors, one gets

$$|V_{\rm cd}|_{\rm NLO} = 0.251 \pm 0.021 \ .$$

Both values should be compared with $0.221 < |V_{\rm cd}| < 0.227$ at 90% C.L. which is obtained when imposing CKM-matrix unitarity and only three generations [11]. Also they are compatible with our previous measurement [17] $|V_{\rm cd}| = 0.219 \pm 0.022$.

Chapter 5

Neutrino-induced production of charm

In this chapter, preliminary results of the measurement of the $|V_{cd}|$ CKM matrix element and the x-distribution of charm and anti-charm are described.

5.1 V_{cd} CKM matrix element

The Cabibbo-Kobayashi-Maskawa matrix is of great importance because its elements are parameters of the Standard Model. Their values enter in the calculation of any electroweak charged current cross section involving a quark. The charm is produced from either d or s quark which gives an opportunity to measure $|V_{cd}|$ and $|V_{cs}|$. Several experiments [77, 76, 74, 17] have extracted the CKM matrix elements $|V_{cd}|$ and $|V_{cs}|$ from a global fit of the distributions of observable kinematical variables. More precisely, a typical procedure was to fit the distributions of "visible" versions of the kinematic variables E, x and the fragmentation variable $z = E_D/\nu$, E_D and ν being the energy of the charm particle and the energy transfer to the hadronic system. The data were fitted to models with four parameters:

- m_c, the charm quark mass;
- α, a parameter that describes the difference in shape between sea $q(\xi, Q^2)$ and $\bar{q}(\xi, Q^2)$;
- κ, the ratio of the nucleon's momentum carried by the strange quarks

relative to that carried by u or d sea quarks, defined as

$$\kappa = \frac{\int_0^1 [\xi s(\xi) + \xi \bar{s}(\xi)] d\xi}{\int_0^1 [\xi \bar{u}(\xi) + \xi \bar{d}(\xi)] d\xi} \; ; \tag{5.1}$$

- $\bar{B}_\mu$, the mean inclusive muonic branching ratio for charmed hadrons produced in neutrino or anti-neutrino scattering.

The analyses fit the same data either to the cross sections from a leading order [77] or from a next-to-leading order [88] QCD model. To extract values for κ and $\bar{B}_\mu$, $|V_{\rm cd}|$ and $|V_{\rm cs}|$ are set to values implied by the three generations CKM matrix unitarity. If the unitarity constrains are dropped, then the fit parameters change from $\bar{B}_\mu \to \bar{B}_\mu |V_{\rm cd}|^2$ and $\kappa \to \bar{B}_\mu \frac{\kappa}{\kappa+2} |V_{\rm cs}|^2$. Then, extracting the muonic branching ratio $\bar{B}_\mu$ from other data leads to the measurement of $|V_{\rm cd}|$ and $|V_{\rm cs}|$. However, the values obtained in this manner are model dependent. In CHORUS, the matrix elements can be directly measured by subtraction of the sea component from the cross section and normalizing it to the charged current neutrino interactions. But before going to this lets recall the cross section formulae.

5.2 Extraction of $V_{\rm cd}$

The method to extract the $V_{\rm cd}$ CKM matrix element is based on the subtraction of the charm produced from the sea s quark from the neutrino sample. In this case, only charm produced from d quark stays in the sample. This analysis is very preliminary and several assumptions have to be made in an attempt to look at the results of the method.

First of all, let go back to charm production (see Eq. 1.70)

$$\frac{d^2\sigma}{dxdy} = G_{\rm F}^2 \frac{yQ^2}{\pi} \Big(|V_{\rm cd}|^2 d(\chi) + |V_{\rm cs}|^2 s(\chi) \Big) \Big[\Big(\frac{1+\cosh\psi}{2} \Big)^2 + \frac{m_{\rm c}^2}{2Q^2} \frac{\sinh^2\psi}{2} \Big] \; , \tag{5.2}$$

where

$$\frac{1}{\eta} = \frac{1}{2x} + \sqrt{\frac{1}{4x^2} + \frac{M^2}{Q^2}} \; , \tag{5.3}$$

$$\cosh\psi = \frac{\eta^2 M^2 - Q^2 + 2\eta(s_{\rm s} - M^2)}{\eta^2 M + Q^2} \; , \tag{5.4}$$

$$\chi = \eta \frac{Q^2 + m_2^2 - m_1^2 + \Delta(-Q^2, m_1^2, m_2^2)}{2Q^2} \; . \tag{5.5}$$

Assuming that the masses are small with respect to the 4-momentum transfer ($m/Q \to 0$) the equations above read

$$\eta \overset{M^2/Q^2\to 0}{=} x \ , \tag{5.6}$$

$$\cosh\psi \overset{M^2/Q^2\to 0}{=} \frac{2-y}{y} \ , \tag{5.7}$$

$$\chi \overset{m_{1,2}^2/Q^2\to 0}{=} x \ . \tag{5.8}$$

Substituting this to the equation of the charm production cross section Eq. 5.2 gives

$$\frac{d^2\sigma}{dxdy} = G_F^2 \frac{Q^2}{\pi}\Big(|V_{cd}|^2 d(x) + |V_{cs}|^2 s(x)\Big)\Big[\frac{1}{y} + \frac{m_c^2}{Q^2} 2(1-y)^2\Big] \ . \tag{5.9}$$

The second term in the brackets which contains confined function $(1-y)$ vanishes when $m_c^2/Q^2 \to 0$. This leads to the following expression for the cross section

$$\frac{d^2\sigma}{dxdy} = G_F^2 \frac{x s_m}{\pi}\Big(|V_{cd}|^2 d(x) + |V_{cs}|^2 s(x)\Big) \ , \tag{5.10}$$

where s_m is a Mandelstam variable (total energy).

Using the assumptions made above, the $|V_{cd}|$ CKM matrix element can be extracted from the data by taking the difference of the ratios

$$R_c = \frac{\sigma(\nu N \to \mu^- c X)}{\sigma(\nu N \to \mu^- X)} - \frac{\sigma(\bar{\nu} N \to \mu^+ c X)}{\sigma(\bar{\nu}_\mu N \to \mu^+ X)} = |V_{cd}|^2 \ . \tag{5.11}$$

The reason to subtract the ratios is to avoid problems related to the normalization of the samples which are related to the neutrino and anti-neutrino beams. The nice property of R_c is its functional dependence only on the valence quark distribution. This fact has three virtues: the valence quark distribution is better measured; the valence quark distribution suffers less suppression from the charm mass; and the valence quark distribution has a theoretical simpler QCD evolution. Also, R_c should be less susceptible to the QCD scale errors because it depends only on the ratios.

There is a tricky point here concerning the normalizations of the charm, anti-charm and charged current samples. The difference between charm and anti-charm samples is mainly due to the beam spectrum described in the previous chapter. A preliminary study of the quasi-elastic interactions and baryonic resonanses production shows that their rate is higher than it is

Table 5.1: Numbers of events that pass the muon identification cut and $W^2 \geq 2\text{GeV}^2$ DIS cut in neutrino and anti-neutrino charged current data and their charm subsamples.

	N_ν^{cc}	N_ν^{charm}	$N_{\bar{\nu}}^{\text{cc}}$	$N_{\bar{\nu}}^{\text{charm}}$
Events	55842	1894	2430	32

expected to be. The reason of it is not clear for the time being. To avoid dealing with the problem a cut is introduced on the squared mass of hadronic system $W^2 \geq 2$ GeV^2. This cut kills quasi-elastic events that are from another kinematic domain compared to DIS. Normally, one would not drop these events but rather merge deep inelastic and quasi-elastic samples but the analysis is not finished yet. Table 5.1 shows the number of events that fulfill the selection requirements. In the assumption that the background in the charm sample is affected by the cut in the same way as charm, the contribution of the white kinks and strange particles scales to 78 events while the anti-charm sample stays the same.

Finally, the value of V_{cd} is extracted using the following formula

$$|V_{\text{cd}}|^2 = \frac{N_\nu^{\text{charm}}}{N_\nu^{\text{cc}}} \cdot \frac{\epsilon_{\text{loc}}^{\text{cc}}(\nu)}{\epsilon_{\text{loc}}^{\text{charm}}(\nu)} \cdot \frac{1}{\epsilon_{\text{rec}}^{\text{charm}}(\nu)} - \frac{N_{\bar{\nu}}^{\text{charm}}}{N_{\bar{\nu}}^{\text{cc}}} \cdot \frac{\epsilon_{\text{loc}}^{\text{cc}}(\bar{\nu})}{\epsilon_{\text{loc}}^{\text{charm}}(\bar{\nu})} \cdot \frac{1}{\epsilon_{\text{rec}}^{\text{charm}}(\bar{\nu})} \ . \quad (5.12)$$

Substitution of the quantities from Eqs. 3.1, 3.4, 5.1 gives

$$|V_{\text{cd}}| = 0.225 \pm 0.014(\text{stat}) \ , \quad (5.13)$$

where the error is dominated by the statistics of the anti-charm sample and includes uncertainty on the charmed fractions, location efficiencies and charm selection. Although the value above is very preliminary it can be compared to $|V_{\text{cd}}|$ extracted from other measurements and from the unitarity of the CKM matrix (see Section 4.5).

The result (Eq. 5.13) has been obtained by using strong assumptions that are not satisfied in the reality. For example, an indirect cut on Q^2 is made by requiring that $W^2 \geq 2\text{GeV}^2$ which is comparable to the charm quark mass m_{c}. To make this analysis complete, the effects related to the masses (nucleon mass, charm quark mass) have to be studied in a rigorious way. But then again, the purpose of this part of analysis was to perform a first test of the method.

5.3 x-distributions

The dependence of the cross section on the Bjorken x variable gives an insight on the distributions of the quarks in a hadron. This information is usually measured in deep inelastic scattering experiments. The statistics of CHORUS is much smaller than in many other experiments which makes the competition tough. But then again, the data collected in CHORUS in terms of the level of background are more pure than in many other experiments. This virtue justifies the study of the production rate of charm as a function of the Bjorken x.

The x-distributions are studied by several collaborations [89, 90, 91, 82]. These groups use different methods and parameterizations to extract the quark distribution shapes. Such analyses are referred to as global analyses. Although there are differences in their results, all in all they show good agreement with experimental data and among each other. Using the parametrization of the global analyses reduces the number of the parameters in the fit.

5.3.1 Reconstruction of kinematics

Before going to the study the quality of the kinematics reconstruction should be investigated. The kinematic variables were defined in Eqs. 1.3, 1.5, 1.2, 1.7. In practice, the following reconstructed variables are used:

$$E_{\rm vis} = E_{\rm had} + E_{\mu_1} + E_{\mu_2} \ , \tag{5.14}$$

$$\nu_{\rm vis} = E_{\rm vis} - E_{\mu_1} \ , \tag{5.15}$$

$$Q^2_{\rm vis} = 2E_{\rm vis}(E_{\mu_1} - p_{\mu_1}\cos\theta) - m^2_{\mu} \ , \tag{5.16}$$

$$x = \frac{Q^2_{\rm vis}}{2m_{\rm N}\nu_{\rm vis}} \ , \tag{5.17}$$

$$y = \frac{\nu_{\rm vis}}{E_{\rm vis}} \ , \tag{5.18}$$

$$W^2_{\rm vis} = m^2_{\rm N} + 2m_{\rm N}\nu_{\rm vis} - Q^2_{\rm vis} \ , \tag{5.19}$$

where θ is the scattering angle of the incident lepton in the laboratory frame and $m_{\rm N}$ is the nucleon mass. The resolution on the visible variables is obtained by fitting the difference between a reconstructed value and a true for the simulated neutrino produced charm sample. The fit is made to the Gaussian probability distribution function 4.3. Figures 5.1, 5.2, 5.3, 5.4, 5.5, 5.6, 5.7, 5.8 show a comparison between the real data and Monte Carlo simulation of x, y, Q^2 and W^2 variables. Some inconsistencies are observed

in W^2 and y distributions between the data and the simulation. The non-Gaussian tails in the distributions have not been simulated so far. One of the possible reasons of such discrapency may come from the correction function that have been used to correct the hadronic energy (see Eq. 3.2). In this case the solution would be to introduce two correction functions: one for DIS sample and the other one for QE+RES.

Figure 5.1: Comparison between the charm data and the simulation in terms of reconstructed Bjorken x. The error bars include only statistical uncertainty. Although the discrepancy in the lowest x bin is more than one standard deviation, the overall agreement is good.

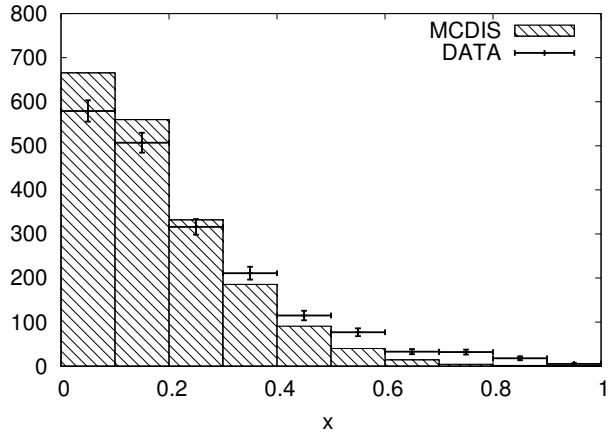

Figure 5.2: The resolution of the x reconstruction. $\mu = (-3.0 \pm 1.1) \times 10^{-3}$, $\sigma = (2.7 \pm 0.1) \times 10^{-2}$.

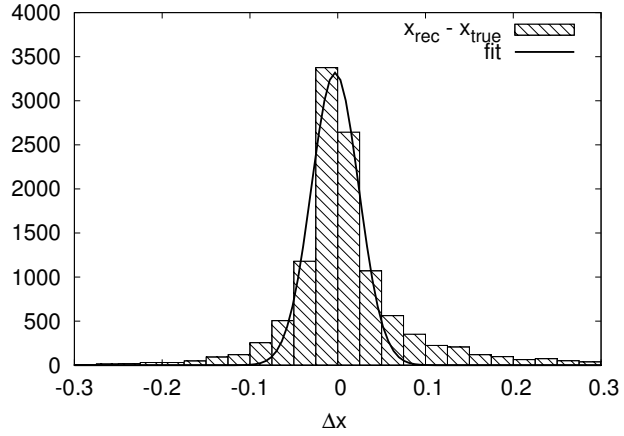

Figure 5.3: Comparison between the charm data and the simulation in terms of reconstructed Bjorken y. The error bars include only statistical uncertainty. MC DIS appears at a higher y with respect to the data. The possible explanations are that the simulated data are less smeared or that there is a certain amount of non DIS produced charm in the data.

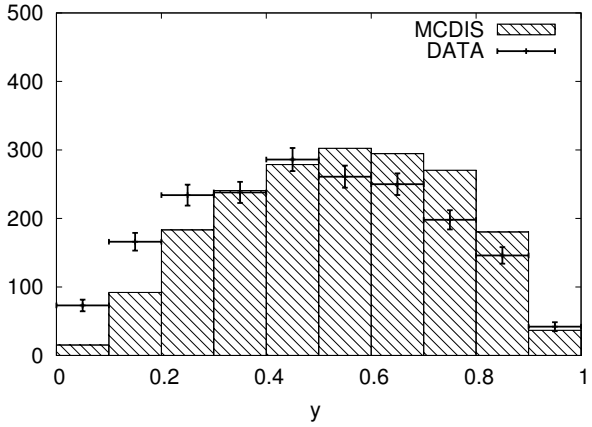

Figure 5.4: The resolution of the y reconstruction. $\mu = (-1.0 \pm 0.1) \times 10^{-1}$, $\sigma = (4.7 \pm 0.1) \times 10^{-2}$.

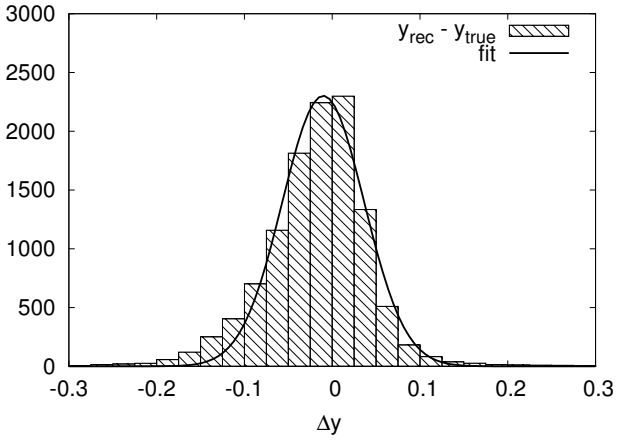

Figure 5.5: Comparison between the charm data and the simulation in terms of reconstructed momentum transfer Q^2. The error bars include only statistical uncertainty. Although the discrepancy in the lowest Q^2 bin is more than one standard deviation, the overall agreement is good.

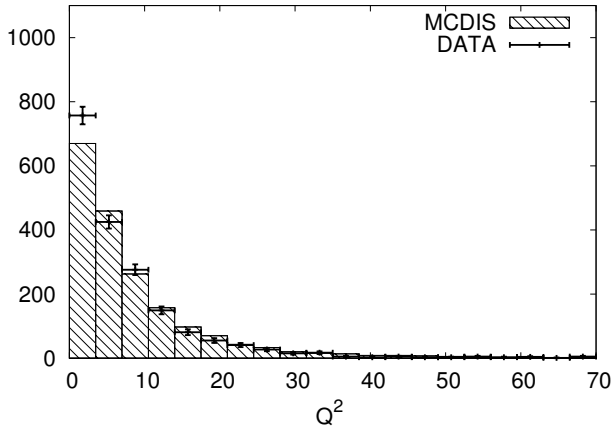

Figure 5.6: The resolution of the Q^2 reconstruction. $\mu = (-3.6 \pm 0.5) \times 10^{-1}$, $\sigma = (7.9 \pm 0.5) \times 10^{-1}$.

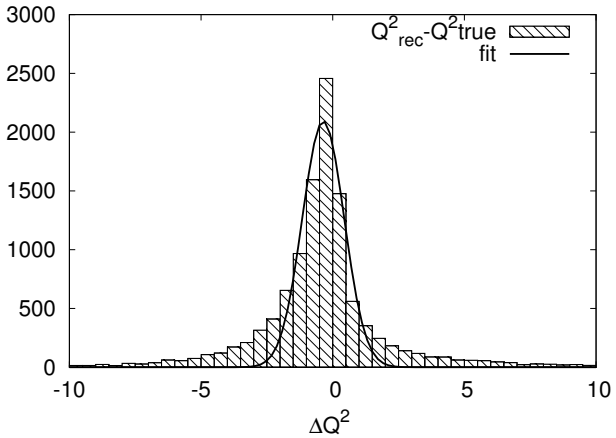

Figure 5.7: Comparison between the charm data and the simulation in terms of reconstructed W^2. The error bars include only statistical uncertainty. Again, the discrepancy between the two may be explained by the presence of non DIS charm in the real data or too pure Monte Carlo.

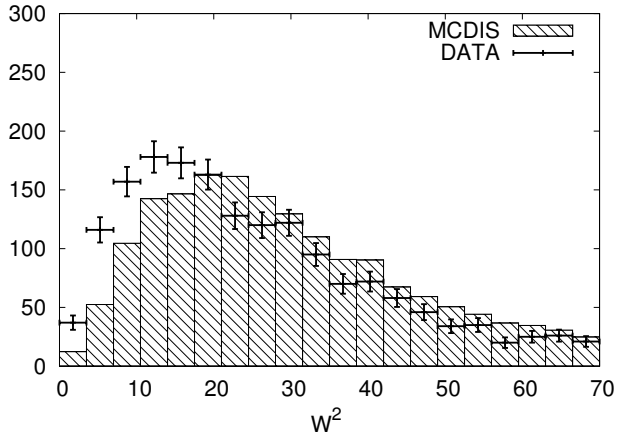

Figure 5.8: The resolution of the W^2 reconstruction. $\mu = -2.5 \pm 0.1$, $\sigma = 5.0 \pm 1.2$.

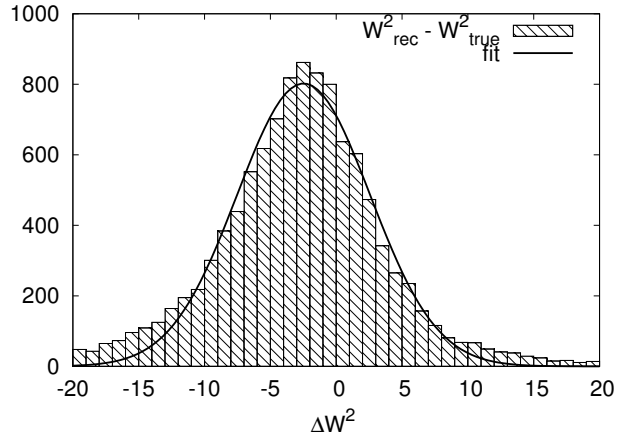

5.3.2 Five-parameter fit

To extract the strange sea component of the nucleon we shall follow the approach proposed by the CDHS collaboration with a parametrization by the E531 collaboration [16]. In their analysis, the valence d quark distribution is parametrized as a function of the Bjorken x:

$$xd(x) \propto x^{\alpha}(1-x)^{\beta} \ , \tag{5.20}$$

and the sea s quark distribution as

$$xs(x) \propto (1-x)^{\gamma} \ . \tag{5.21}$$

In general, in Eq. 5.21 the d_{S} quark from the sea should also be present. Its contribution is neglected in the assumption that the $d_{\mathrm{S}}(x)$ does not differ very much from $s(x)$ but $d_{\mathrm{S}}(x)$ is Cabibbo-suppressed while $s(x)$ is Cabibbo-favoured. Thus, the total Bjorken x quark distribution can be written as

$$\frac{dN}{dx} \propto N_{\mathrm{d}} x^{\alpha}(1-x)^{\beta} + N_{\mathrm{s}}(1-x)^{\gamma} \ , \tag{5.22}$$

where N_{d} and N_{s} are normalization factors.

After choosing a parametrization, Eq. 5.22 is smeared according to the resolution of the reconstruction of x in each bin. The reason to blur the original distribution lies in the fact that the CHORUS detector has been built with severe design limits mainly because it was supposed to be a discovery machine and to discover different types of events with respect to charm. The average muon momentum resolution is about 15% which translates to ∼30% in terms of the Bjorken x. The most convenient way to take into account the smearing is to introduce a migration matrix $\mathcal{M}_{ij}$ between the bins whose elements are the fractions normalized to one. The matrix is defined using the simulation of the process and the reconstruction of x. Doing so, the function F′ in bin number i is defined as

$$\mathrm{F'}_i = \sum_j \mathrm{F}_j \mathcal{M}_{ji} \ , \tag{5.23}$$

where F is an analytical function.

To perform a good fit, the number of degrees of freedom should be much larger than the number of fit parameters. The data samples have been subdivided into 40 equal bins compared to 5 fit parameters. Such a division gives stability to the fit on one hand and statistical significance in each bin on the other hand. The fit is made using the MINUIT package [81].

Figure 5.9: Comparison between charm neutrino data and the result of the five-parameters fit. The data points are corrected for the reconstruction efficiency using the migration matrix formalism. The error bars include only the statistical errors.

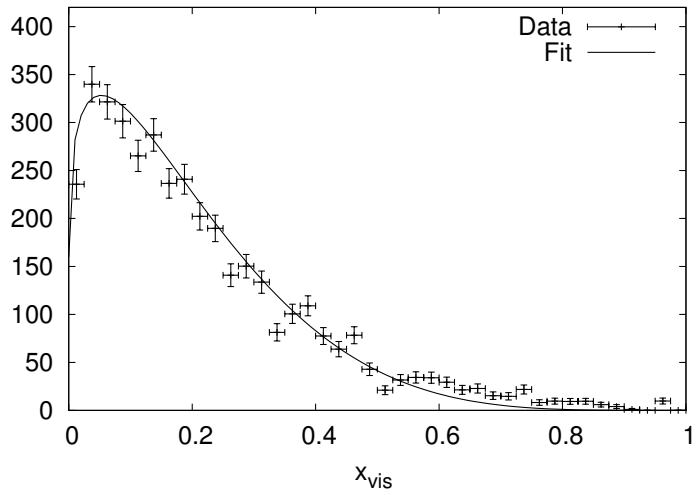

It was used to find a set of parameters which has a minimum χ^2 for the data corrected for the charm selection efficiency. The results are graphically shown in Fig. 5.9 and their numerical values are as follows:

$$\begin{aligned} N_{\rm d} &= 440.1 \pm 17.6 \ , \\ \alpha &= 0.30 \pm 0.02 \ , \\ \beta &= 3.09 \pm 0.04 \ , \\ N_{\rm s} &= 236.7 \pm 12.0 \ , \\ \gamma &= 5.30 \pm 0.15 \ , \end{aligned} \tag{5.24}$$

while the correlation coefficients matrix from the fit is

$$C_{\rm fit}^{\rm charm} = \begin{pmatrix} 1 & -0.15 & 0.89 & 0.34 & 0.87 \\ & 1 & -0.29 & 0.87 & -0.39 \\ & & 1 & 0.18 & 0.67 \\ & & & & 1 \end{pmatrix}$$

Figure 5.10: Anti-neutrino charm data are compared to the result of the fit. The error bars include only the statistical errors using approach from Ref. [84].

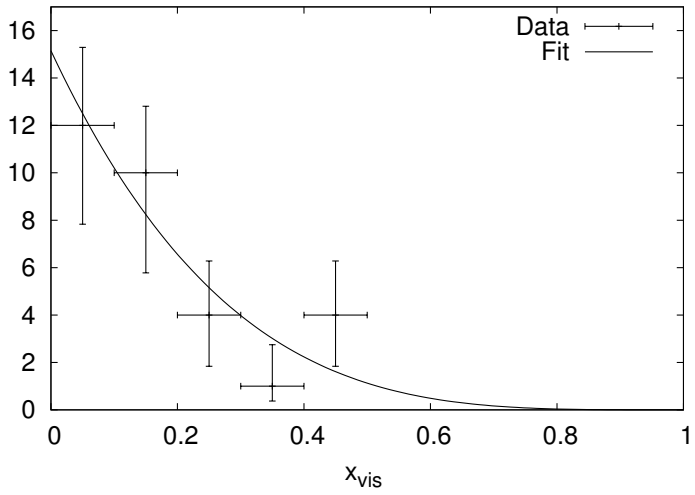

A similar two-parameters fit could be done for anti-neutrino data. Since the data sample is much smaller, the fit is performed using only five degrees of freedom. The results are shown in Fig. 5.10 and the numerical values are:

$$\begin{aligned} N_{\mathrm{s}} &= 15.2 \pm 1.4 \\ \gamma &= 3.7 \pm 0.6 \ . \end{aligned} \tag{5.25}$$

The related correlation matrix is

$$C_{\mathrm{fit}}^{\mathrm{anti-charm}} = \begin{pmatrix} 1 & 0.75 \\ & 1 \end{pmatrix}$$

The value of γ in Eq. 5.25 can be compared to a similar parameter in Eq. 5.24. The discrepancy may come from the spectrum of neutrino and anti-neutrino beam which affects the production of charm.

5.4 Discussion

The preliminary result of the first direct measurement of $|V_{\mathrm{cd}}|$ CKM matrix element is in agreement with the value obtained from the current measure-

Table 5.2: Comparison of κ from different experiments.

Experiment	κ	Ref
CDHS	0.47 ± 0.09	[74]
CHARM	0.39 ± 0.12	[75]
CHARM II	0.39 ± 0.1	[76]
CCFR	0.44 ± 0.11	[77]
E531	0.32 ± 0.25	[15]
NOMAD	0.48 ± 0.19	[78]
CHORUS calo	0.33 ± 0.08	[92]

ments of the other elements and imposing three generation unitarity.

The measurement of the distribution of charm data as a function of Bjorken x is consistent with the previous measurements [15, 16, 93]. It is possible to estimate the relative fractions of charm produced from d and from s quarks. Calculating two integrals

$$\int_0^1 440.1 x^{0.3}(1-x)^{3.09} dx = 60.3 \ , \tag{5.26}$$

$$\int_0^1 236.7(1-x)^{5.3} dx = 37.6 \tag{5.27}$$

shows that 38.8% of all charm in neutrino interactions is produced from the strange sea quark. The found ratio can be converted to another parameter κ (see Eq. 5.1) by using the total quark/anti-quark ratio measured by CCFR collaboration [94]

$$\frac{\bar{Q}}{Q} = 0.198 \ . \tag{5.28}$$

Finally, the ratio of κ is obtained by taking into account the values of the CKM matrix elements (to give $|V_{\rm cd}| = 0.224$ and $|V_{\rm cs}| = 0.996$):

$$\kappa = \frac{S+\bar{S}}{\bar{U}+\bar{D}} = \frac{N_{\rm s}}{N_{\rm d}} \frac{|V_{\rm cd}|^2}{|V_{\rm cs}|^2} \frac{Q}{\bar{Q}} = 0.14 \ . \tag{5.29}$$

The obtained value is quite low if compared with other measurements shown in Table 5.2. The reason is not understood but the descrapency may come from non-DIS events, x-distribution parametrization(see Eq. 5.22) and statistics.

Conclusions

The development of the fast automatic scanning systems allowed to enlarge the topics of physical analyses in the CHORUS collaboration. Apart from the $\nu_\mu \rightarrow \nu_\tau$ oscillation search, the CHORUS collaboration has studied numerous subjects related to the charm quark production in neutrino-induced charged current interactions and their decays as well as associated charm production in neutral current neutrino interactions. In particular, this thesis concerns the direct measurement of the topological muonic branching ratios of the charmed hadrons, an attempt of direct measurement of the $|V_{\rm cd}|$ Cabibbo-Kobayashi-Maskawa matrix and the dependence of the charm production rate as a function of Bjorken x kinematic variable. The analyses are based on about 100,000 charged current interactions with a sub-sample of 2013 charm decay candidates manually observed in the emulsion. The eye-check dramatically increases the charm selection purity (>95%) while preserving a good selection efficiency (∼70%).

The extraction of the muonic branching ratio of charmed hadrons is based on the mixture of the ratios for each decay topology. Such an approach allows also to measure the muonic branching ratio for $\rm D^0$

$$B_\mu(\rm D^0) = [6.5 \pm 1.2\ (\rm stat) \pm 0.3\ (\rm syst)] \times 10^{-2}\ ,$$

while considering only decays with four prongs

$$3.0 \times 10^{-4} < B_\mu(\rm D^0 \rightarrow V4) < 3.4 \times 10^{-3}\ .$$

The inclusive muonic branching ratio for the complete sample of charm hadrons is therefore determined to be

$$\overline{B}_\mu = [7.3 \pm 0.8\ (\rm stat) \pm 0.2\ (\rm syst)] \times 10^{-2}.$$

Normalizing the above value to the charged currents gives an average dimuon cross section

$$\frac{\sigma_{\mu^-\mu^+}}{\sigma_{\rm cc}} = [3.16 \pm 0.34\ (\rm stat) \pm 0.09\ (\rm syst)] \times 10^{-3}\ .$$

The $|V_{cd}|$ matrix element is extracted by subtracting the strange sea component from the charm production. Its value is found to be

$$|V_{cd}| = 0.225 \pm 0.014 \ .$$

This preliminary result is consistent with the previous measurements. It is also in agreement with the value estimated from the measurements of the other elements and from imposing a three generations unitary CKM matrix.

The x-distribution analysis shows that approximately one-third of all charm is produced from the strange sea quarks. The x-distribution of the charm data is fitted by an analytical function and the result is found to be

$$N_d x^{0.30}(1-x)^{3.1} + N_s(1-x)^{5.3} \ .$$

The output of the fit is consistent with other measurements where a similar parametrization has been chosen [16].

It is worth mentioning that both analyses are directly connected to the measurement of the charm production cross sections which is not finished so far.

Bibliography

[1] J.-E. Augustin *et al.*, *Phys. Rev. Letters* **33**, 1404 (1974).

[2] J. J. Aubert *et al.*, Phys. Rev. Letters **33**, 1406 (1974).

[3] S. L. Glashow, *Nucl. Phys.* **22**, 579 (1961).

[4] S. Weinberg, *Phys. Rev. Lett.* **19**, 1924 (1967).

[5] A. Salam, in *Elementary Particle Theory: Relativistic Groups and Analyticity (Nobel Symposium No. 8)*, 367 (1968).

[6] M. Kobayashi and T. Maskawa, *Prog. Theor. Phys.* **49**, 652 (1973).

[7] N. Cabibbo, *Phys. Rev. Lett.* **10**, 531 (1963).

[8] L. Wolfenstein, *Phys. Rev. Lett.* **51**, 1945 (1983).

[9] *CKMfitter project*, `http://www.slac.stanford.edu/xorg/ckmfitter`; J. Charles . *et al.*, *Eur. Phys. J.* **C41**, 1-131 (2005).

[10] S. L. Glashow, J. Iliopulos and L. Maiani, *Phys. Rev.* **D2**, 1285 (1970).

[11] Particle Data Group, S. Eidelman et al., Physics Letters **B592** (2004) 1.

[12] R. A. Johnson *et al.*, NuTeV collaboration, arXiv:hep-ex/9904028 (1999).

[13] G. P. Zeller *et al.*, NuTeV collaboration, Phys. Rev. Lett. **90**, 239902 (E) (2003).

[14] H. Georgi and S.L. Glashow, *Phys. Rev. Letters* **32**, 438 (1974)

[15] N. Ushida *et al.*, *Phys. Lett.* **B206** (1988) 380.

[16] N. Ushida *et al.*, *Phys. Lett.* **B206** (1988) 375.

[17] A. Kayis-Topaksu *et al.*, CHORUS Collaboration, *Phys. Lett.* **B549** (2002) 48.

[18] M. A. G. Aivazis, F. I. Olness, and W.-K. Tung, *Phys. Rev.* **D 50**, 3085 (1994).

[19] W. Seligman, Ph.D. Thesis, Nevis Report 292 (1996).

[20] P.S. Auchincloss *et al.*, *Z. Phys.* **C48**, 411 (1990).

[21] D.B. MacFarlane *et al.*, *Z. Phys.* **C26**, 1 (1984).

[22] P. Berge *et al.*, *Z. Phys.* **C35**, 443 (1987).

[23] J. D. Bjorken, *Phys. Rev.* **179**, 1547 (1969).

[24] E. D. Bloom *et al.*, *Phys. Rev. Lett.* **23**, 930 (1969).

[25] M. Breidenbach *et al.*, *Phys. Rev. Lett.* **23**, 935 (1969).

[26] J. I. Friedman and H. W. Kendall, *Annu. Rev. Nucl. Part. Sci.* **22**, 203 (1972).

[27] C. G. Callan and D. G. Gross, *Phys. Rev. Lett.* **22**, 156 (1969).

[28] M. Arneodo *et al.*, (New Muon Collaboration), *Phys. Rev.* **D50** (1994) 1.

[29] P. Amaudruz *et al.*, (New Muon Collaboration), *Nucl. Phys.* **B371** (1992) 3.

[30] J. C. Collins, D. E. Soper and G. Sterman, in *Perturbative quantum Chromodynamics*, edited by A. H. Muller (World Scientific, Singapore), p.1 (1989).

[31] G. Sterman *et al.*, Handbook of perturbative QCD. *Reviews of Modern Physics*, 67(1):157-248, 1995.

[32] V. N. Gribov and L. N. Lipatov, *Sov. J. Nucl. Phys.* **15**, 438 (1972).

[33] G. Altarelli and G. Parisi, *Nucl. Phys.* **B 126**, 298 (1977).

[34] M. A. G. Aivazis, F. I. Olness, and W.-K. Tung, *Phys. Rev.* **D 50**, 3102 (1994).

[35] O. Nachtmann, *Nucl. Phys.* **b 63**, 237 (1973).

[36] D. Yu. Bardin and V. A. Dokuchaeva, JINR E2-86-260, April 1986.

[37] S. Jadach *et al.*, Comput. Phys. Commun. **76**, 361 (1993).

[38] A. Kayis-Topaksu *et al.*, *Phys. Lett.* **B 575**, 198 (2003).

[39] F. Di Capua, PhD thesis, Università Federico II and INFN, Naples, 2003.

[40] R. E. Shrock and B. W. Lee, *Phys. Rev.* **D13**, 2539 (1976); Erratum: *Phys. Rev.* **D14**, 313 (1976).

[41] C. Acquistapace *et al*, CERN-ECP-95-014.

[42] S. Sorrentino. CHORUS internal report 980005, (1998).

[43] R. G. C. Oldeman, PhD thesis, University of Amsterdam, The Netherlands, June 2000.

[44] A. Kayis-Topaksu *et al.*, *Submitted to Phys. Lett.* **B**, February 2005.

[45] E. Eskut et al., *Nuclear Intruments and Methods* **A401** (1997).

[46] S. Aoki *et al.Nuclear Instruments and Methods* **A344**, 143(1994).

[47] CHORUS collaboration, P.Annis *et al*, *Nuclear Instruments and Methods*, **A367**,367-371(1995).

[48] F. Bergsma *et al.*, *Nuclear Instruments and Methods*, **A357**, 243(1994).

[49] H. Abramovitz *et al. Nuclear Instruments and Methods*, 180, 429(1981).

[50] A. Blondel *et al. Z. Phys.* **C 45**, 361(1990).

[51] J.P. Dewulf *et al.* (CHARM II Collaboration) *Nuclear Instruments and Methods*, **A252**, 443(1986).

[52] J.P. Dewulf *et al.* (CHARM II Collaboration) *Nuclear Instruments and Methods*, **A263**, 109(1988).

[53] D. Geiregat *et al.* (CHARM II Collaboration), *Nuclear Instruments and Methods*, **A 325**, 92(1993).

[54] T. Bauche, Ph. D. Thesis, University of Hamburg (1988).

[55] P. Zucchelli, Ph.D. thesis, University of Ferrara, Italy (1996).

[56] T. Sjöstrand, *Comput. Phys. Commun.* **82**, 74 (1994).

[57] G. Ingelman, Preprint TSL/ISV 92–0065, Uppsala University, Sweden (1992).

[58] S. Riccardi, Ph.D. thesis, Universit'a di Ferrara, 1996.

[59] *GEANT 3.21*, CERN program library long writeup W5013.

[60] T. Nakano, Ph.D. thesis, University of Nagoya, Japan, 1997.

[61] B. van de Vijver, PhD thesis, Vrije Universiteit Brussel, 2002.

[62] N. Nonaka, Ph.D. thesis, University of Nagoya, Japan, 2002.

[63] A. M. Güler, PhD thesis, Middle East Technical University, 2000.

[64] M. Sorrentino, CHORUS internal note 2000027 (2004), `http://choruswww.cern.ch/Publications/Notes/charm_background.pdf`

[65] P. Astier *et al*, NOMAD Collaboration, *Nucl. Phys.* **B621** (2002) 3.

[66] G. Önengüt *et al*, *Phys. Lett.* **B613** (2005) 105.

[67] G. De Lellis *et al.*, *Phys. Rep.* **399** (2004) 227.

[68] G. Onengut *et al.*, *Phys. Lett.* **B604** (2004) 11.

[69] G. De Rosa, PhD thesis, Università Federico II and INFN, Naples, 2004.

[70] G. De Lellis *et al.*, *Phys. Lett.* **B550** (2002) 16.

[71] A. Kayis-Topasku *et al.*, *Phys. Lett.* **B527** (2002) 173.

[72] A. Kayis-Topasku *et al.*, *Phys. Lett.* **B555** (2003) 156.

[73] J. Panman, *Muon recognition algorithm for post-scanning analysis*, CHORUS internal note (2002), `http://choruswww.cern.ch/Internals/Charm/murecoNote.pdf`

[74] H. Abramowicz *et al.*, *Z. Phys.* **C15** (1982) 19.

[75] M. Jonker *et al.*, *Phys. Lett.* **B107** (1981) 241.

[76] P. Vilain *et al.*, *Eur. Phys. J.* **C11** (1999) 19.

[77] S.A. Rabinowitz *et al.*, *Phys. Rev. Lett.* **70** (1993) 134;
arXiv:hep-ex/9406007 .

[78] P. Astier *et al.*, *Phys. Lett.* **B486** 35 (2002).

[79] D. Naples *et al.*, *Nucl. Phys.* (Proc. Suppl.) **B118** (2003) 164.

[80] M. Goncharov *et al.*, *Phys. Rev.* **D64** (2001) 112006.

[81] F. James and M. Winkler. `http://www.cern.ch/minuit`. CERN, May 2004.

[82] M. Glück, E. Reya and A. Vogt, *Z. Phys.* **C67** (1995) 443.

[83] CTEQ Collaboration, H.L. Lai *et al.*, *Phys. Rev.* **D51** (1995) 4763.

[84] G.J. Feldman and R.D. Cousins, *Phys. Rev.* **D57** (1998) 3873.

[85] K. Kodama *et al*, *Phys. Lett.* **B313** (1993) 260.

[86] N. Bruski, Ph.D. thesis, Westfälische Wilhelms-Universität, Münster, Germany (2002).

[87] G. De Lellis *et al.*, *J. Phys. G: Nucl. Part. Phys.* 28 (2002) 713.

[88] A.O. Bazarko *et al.*, *Z. Phys.* **C65** (1995) 189

[89] A.D. Martin, R.G. Roberts, W.J. Stirling and R.S Thorne, *Phys. Lett.* **B531** (2002) 216.

[90] arXiv:hep-ph/0201195.

[91] arXiv:hep-ph/0211096,
arXiv:hep-ph/0404111.

[92] CHORUS collaboration, draft in preparation.

[93] T. Bolton, arXiv:hep-ex/9708014.

[94] C. Foudas *et al.*, *Phys. Rev. Lett.* **64**, 1207 (1990).

[95] A. E. Asratyan *et al.*, *Z. Phys.* **C68** (1995) 43.

[96] M. Burkardt and B.J. Warr, *Phys. Rev.* **D45** (1992) 958.

[97] C. G. Wohl, unpublished note, 2002.

[98] CHORUS internal note 2000021, 2002.

[99] *The GNU operating system*, `http://www.gnu.org`

[100] *Zsh shell webpage*, `http://www.zsh.org`

[101] *Gnuplot homepage*, `http://www.gnuplot.info`

Acknowledgements

It is a pleasure to thank the many people who made this thesis possible.

I am greatful to my supervisor Thierry Delbar for supporting me all this time and his confidence in me.

I would like to thank Bart Van De Vijver for introducing me into the experiment. It was him who inspired me to do a PhD thesis in charm analysis in the framework of the CHORUS experiment. After all these years I can certainly state that it was the right choice. Since the time when I was a summer student at CERN it was always a great pleasure to work with him.

I am deeply obliged to Jaap Panman, the CERN group leader, for the helpful guidance through many problems I have encountered during the stages of the work, for his nice sense of humor and care he brings to everything he does.

I am very greatful to Vincent Lemaitre for numerous constructive discussions. After each discussion with him I was able to look on the things that I did from another perspective which was extremely useful.

I express my gratitude to Pierre Vilain, Biaggio Saitta and Ilya Tsukerman for their relevant remarks and comments on the paper. I was truly delighted to work with these people who ask the right questions.

I am indebted to Ilya Tsukerman, Andrey Artamonov, Gianfranca De Rosa and Aysel Topasku for numerous data samples and useful discussions without which this analysiswould never have been finished.

I wish to express my gratitude to Koyu Niwa, Masahiro Komatsu, Osamu Sato, Kouji Narita, Kaoru Hoshiro and Murat Güler. Their help with handling of the emulsion and personal support made the visits in FKEN laboratory Nagoya not only very informative but also extremely enjoyable. The stays in Japan are still vivid in my mind.

This work would not have been possible without the support and encouragement of the colleagues from the CHORUS collaboration and I am thankful to all of them.

I cannot forget many postdocs, PhD students and students from the Institut de Physique Nucléaire in the charming (we can say it now) city of Louvain-la-Neuve. Especially, I would like to mention Ginette Tabordon and Carine Baras, the secretaries of FYNU and CRC. I am pretty sure that every physicist in the world understands how big is the impact of a secretary in research. Working in FYNU was (and still is) a lot of fun and pleasure. Merci.